FORSCHUNGSZENTRUM ROSSENDORF FZR

WISSENSCHAFTLICH-TECHNISCHE BERICHTE
FZR-282
Dezember 1999
ISSN 1437-322X

Dmitri Kamanin

Probing the time scale of asymmetric fission

Herausgeber:
FORSCHUNGSZENTRUM ROSSENDORF
Postfach 51 01 19
D-01314 Dresden
Telefon +49 351 26 00
Telefax +49 351 2 69 04 61
http://www.fz-rossendorf.de/

Als Manuskript gedruckt

FORSCHUNGSZENTRUM ROSSENDORF

WISSENSCHAFTLICH-TECHNISCHE BERICHTE

FZR-282

Dezember 1999

Dmitri Kamanin

Probing the time scale of asymmetric fission

Dissertation

Probing the time scale of asymmetric fission

PhD Thesis

of

Dipl.-Phys. Dmitri Kamanin
born on June 15th, 1966
in Leningrad
USSR

Supervisors: Prof. H. Freiesleben
Dr. W. Wagner
Dr. H.-G. Ortlepp

Dresden, October 29, 1999

Contents

1 Introduction 3

2 Status of the field and particular tasks 5
- 2.1 General problems . . . 5
- 2.2 Scission dynamics . . . 6
- 2.3 LCP emission studies . . . 7
- 2.4 Contribution of FOBOS and motivation of further work . . . 8
- 2.5 Particular tasks of this thesis . . . 10

3 The experimental setup 12
- 3.1 Design of the FOBOS detector . . . 12
- 3.2 Position-sensitive avalanche counters . . . 15
- 3.3 Axial ionization chambers . . . 16
- 3.4 Forward array . . . 18
- 3.5 Data acquisition system hardware . . . 19
- 3.6 Experimental data structure and software . . . 21

4 Scintillator shell of the FOBOS detector 22
- 4.1 Design of the scintillator shell . . . 22
- 4.2 Scintillation detector unit . . . 24
- 4.3 The geometry of the scintillator shell . . . 26
- 4.4 Scintillator shell electronics . . . 27
- 4.5 Test of self-consistency and stability of data . . . 30
- 4.6 The scintillator shell data processing . . . 35

5 Calibration of the scintillator detectors of FOBOS 39
- 5.1 Calibration problem . . . 39
- 5.2 Calibration method . . . 41
- 5.3 Simulation of the particle identification matrix . . . 42
- 5.4 Shape-scaling method . . . 46
- 5.5 Check of the calibration . . . 48
- 5.6 Final remarks . . . 50

6 Experimental results 53
- 6.1 Main observables and parameters . . . 53
  - 6.1.1 Excitation energy . . . 53
  - 6.1.2 Mass-asymmetry . . . 55
  - 6.1.3 Total kinetic energy and masses . . . 58

6.2 Analysis of the LCP data 63
6.2.1 Primary LCP data analysis 64
6.2.2 ^{14}N 34 MeV/nucleon experiment 66
6.2.3 Post-scission multiplicities at ^{14}N 53 MeV/nucleon 67
6.2.4 Pre-scission multiplicities at ^{14}N 53 MeV/nucleon 70
6.2.5 Slope parameter measurement 71
6.3 Exploring the mass-asymmetry 73
6.3.1 Definition of symbols 73
6.3.2 The mass-asymmetry matrix 76
6.3.3 The TKE factor R_χ 78
6.3.4 Experiment with ^{40}Ar (36 AMeV) beam 80
6.3.5 Anomaly of the cooling curve 84
6.3.6 Inventory of the $\zeta - \chi$ matrix 87
6.3.7 Does asymmetric fission proceed faster? 91

7 Summary **94**

A Geometry of the scintillator shell **97**

B Energy calibration data **99**

C Kinetic temperature **102**

D Numerical simulations **103**
D.1 Cooling down by light particle emission 103
D.2 Available temperatures 104
D.3 Pre-equilibrium emission 105

Acknowledgments **107**

Bibliography **108**

Index **115**

Chapter 1

Introduction

A bulk of data concerning heavy-ion induced nuclear reactions at low and intermediate energies is available to date. In the so-called Fermi energy domain, at energies of about 30–50 AMeV, these reactions are governed from the first touching of the two nuclei to the creation of the final products by a complicated interplay of different processes which are thermodynamical in nature.

Thereby, the formation of an excited compound-like nucleus is one of possible reaction channels while nuclear fission remains to be the dominating decay mode for a large interval of excitation energies. The disintegration of heated heavy nuclei into two fission fragments (FF) mainly competes with the emission of neutrons and at temperatures above 3 MeV [1] light charged particles (LCP). It seems to be well established now, that fission represents an overdamped collective motion that brings the compound system over the saddle of the potential energy surface to a considerably large deformed scission configuration, and that proceeds on a time scale of several units of 10^{-20} s [2].

By now, the experimental efforts to extract fission time scales and nuclear friction coefficients have concentrated mostly on the study of reactions where it is assumed that the reacting nuclei fuse completely forming a fully equilibrated composite system with well-defined characteristics. In particular, compound nuclei are formed with moderate

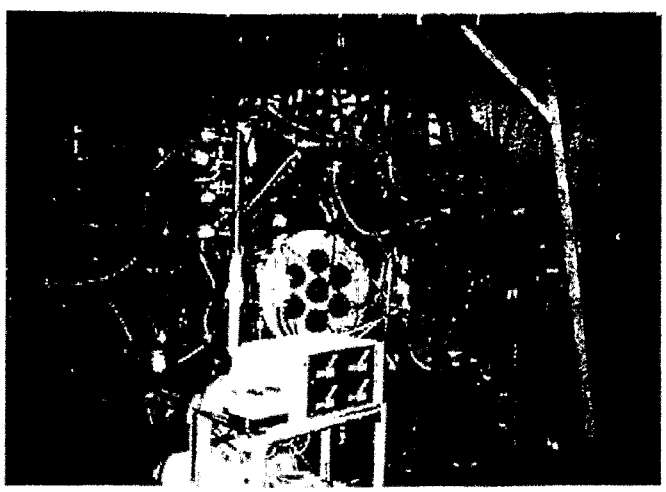

Figure 1.1: *The view of the FOBOS 4π-spectrometer. The height of the viewed area at the detector site amounts to 3 m.*

temperatures $T \sim 1.5$–2.5 MeV. To increase the temperature of a given system one obviously should increase the projectile energy. However, as the bombarding energy becomes larger than $\sim$ 10–15 AMeV, dynamical effects lead to an incomplete fusion mechanism [3] in which particles or a cluster of particles are emitted in the very early stage of the reaction thus carrying away a considerable amount of mass, energy, linear and angular momenta before the composite system reaches its thermal equilibrium. Hence, an increase in excitation energy is achieved at the expense of a less defined composite nucleus. The uncertainties in the properties of such a composite system can be remedied by measuring both fission fragments. With reasonable assumptions about the relation between linear momentum transfer and excitation energy [4] the properties of the composite system can be inferred. This method demands a detection system of high efficiency for correlated fragments achievable only in a so-called 4π-device [5].

The 4π fragment spectrometer FOBOS [6] (fig. 1.1), built up in the JINR/Dubna is one of such devices especially designed for the study of the fission process in the Fermi energy domain. Utilizing the FOBOS detector one is able to deduce "event by event" the fission fragment masses, charges and momentum components in a wide dynamical range. In addition, a shell of CsI scintillators surrounding the fragment detectors was constructed for the independent registration of light charged particles. The high geometrical efficiency of FOBOS opened the possibility to reconstruct the reaction kinematics and the inclusion of data obtained with the scintillator shell nourished great hope for deducing pre- and post-scission LCP multiplicities as well as LCP spectra by means of a clear separation of different emission sources. The dependence of LCP characteristics is to be explored as a function of both excitation energy of the composite system and fission mass asymmetry. Furthermore, the experimental data should provide valuable information on the excitation energy and its partition between the fragments at the instant of scission.

The study of the sharing of excitation energy between the fragments turned out to be an issue of a great interest. The deviation of the excitation energy partition from thermodynamical equilibrium should hint at a faster time scale relative to that proceeding via equilibrium. A decay time of $(60 \pm 20) \times 10^{-21}$s for symmetric fission was deduced from the distribution of the fission fragment masses measured by the FOBOS detector [7]. Evidence has been found for some additional process coming into play at initial excitation energies larger than $\approx$ 300 MeV in fission of Au- and Th-like composite systems. This process feeds more asymmetric disintegrations and is supposed to be faster than fission at lower excitation energies. The latter fact naturally raised the question whether asymmetric fission proceeds faster than symmetric one. A number of papers is devoted to this problem, but no definite answer has been found up to now. The information on the excitation energy sharing between the fragments together with the light charged particle data measured at FOBOS was expected to give further insights into the problem of fission time scales.

The present thesis is organized as follows. Chapter 2 contains a short review of the present situation in the field of related investigations and lists the tasks of this thesis referring to results obtained earlier at the FOBOS detector. Chapter 3 is devoted to the description of the experimental setup. Chapter 4 covers in details the scintillator shell, which has been built and put into operation by main efforts of the author. A new method of intrinsic energy calibration of the scintillator shell is presented in Chapter 5. Chapter 6 lists physical results obtained by the data analysis, and main conclusions are given in Chapter 7.

Chapter 2

Status of the field and particular tasks

2.1 General problems

Numerous attempts to describe nuclear collisions in the Fermi energy domain reflect the great interest in a coherent description of nuclear matter behavior [8]. With respect to low energy reactions, there is a drastic increase of the number of possible intermediate states between two known instants: i) impact of a projectile on a target and ii) a set of reaction products in a detector system. This leads to the difficulty of separating the problem into two subsets: entrance channel problems (elastic, inelastic, fusion, incomplete fusion etc.) and exit channel problems (fission, quasi-fission, multifragmentation etc.). Since different approaches are used for the description of the entrance and exit channels, it is convenient to introduce an averaged intermediate state which would bridge them. The analysis of the nucleus-nucleus collision dynamics and decay characteristics of compound-like products requires also a consideration of light particle (LP) and γ-ray emission because these processes bring large contributions to the total reaction cross section.

Emission of LPs at the very early stage of reaction (projectile break-up, pre-equilibrium emission etc.) is governed by the dynamics of the heavy product formation. Particles emitted at later stages of the reaction are treated normally such as they do not "remember" the entrance channel. LPs and γ-rays accompanying nucleus-nucleus collisions are the objects of the systematical study because they remove from the interaction region a significant amount of nuclear matter with certain quantum properties [9]. A complete description of the formation and decay of compound-like systems cannot be achieved without understanding the LP emission mechanisms. Experimentally observed properties of mass, energy and angular distributions of LPs are sometimes quite unexpected. The explanation of these properties is very difficult because a large number of LP emission sources are involved. The experimental discrimination of these sources is a problem of increasing importance.

The nuclear fission is undoubtedly a reaction of particular interest. A compound nucleus represents a long-living body of excited nuclear matter of some definite geometrical shape, which exhibits quantum properties at the same time. The rich experimental data concerning different aspects of fission dynamics are collected and analyzed to date [2, 10, 11]. In accordance with a well-known empirical relation of Viola [12], the mean total kinetic energy (TKE) of fission fragments for a given compound nucleus does not reveal

any dependence on the excitation energy. This reflects large overdamping in the collective motion towards fission. The nature and magnitude of nuclear viscosity and its effect on fission remains a topic of great interest [5]. The so-called "dynamical delay" of fission induced by nuclear viscosity is recognized through a relative increase in the pre-scission emission of neutrons [13, 14, 15] and LCP [16] (in comparison with predictions of standard statistical models), as well as by the enhanced emission of giant dipole resonance (GDR) γ-rays [17, 18]. In spite of these extensive studies a number of general questions still remains open. The question how fission proceeds with respect to the time-space evolution of the nuclear matter is essential in understanding the collective behavior of a multi-nucleon system. In contrast to a usual picture of fission as a sequence of equilibrium steps, Brosa [19] treated fission as "an evolution of instabilities". The random neck rupture approach requires a violent stretching of a nucleus to a pre-scission configuration, and the position of the neck rupture, accounting for the fission mass fluctuations, is not pre-defined. The mass-asymmetry, hence, is introduced as an independent degree of freedom.

A complicated shape evolution from some initial symmetrical form of a composite system to an asymmetric configuration in the exit channel appears as a rather time-consuming process. Statistical and quantum properties of the studied objects make it difficult to come to a definite conclusion about the time scales.

2.2 Scission dynamics

Time scales play a key role in understanding fission and quasifission dynamics. Information of it is contained in such well-studied observables as TKE and its width, fission mass-distribution widths, angular distributions of massive fragments and so on. The experimental and theoretical findings on fission time scales are rather controversial. Hinde et al. [15], for example, deduced a dynamical fission time scale of 35 ± 15 zs [1] by analyzing pre-scission neutron multiplicities and mean kinetic energies in fusion-fission reactions of symmetrical fission of compound nuclei with $A \sim 140 - 250$ and excitation energies $E^* \sim 0.3 - 1.2$ MeV/nucleon. Hinde also concluded that the dynamical fission time decreases with increasing mass asymmetry in the fission split. Similarly, Lestone [20] found a dynamical fission time of 30 ± 10 zs by analyzing pre-scission proton and α-particle multiplicities and mean kinetic energies, also in fusion-fission reactions of fission of compound nuclei with $A \sim 195$ and excitation energies $E^* \sim 0.3 - 0.5$ MeV/nucleon.

Most data concerning fission dynamics are obtained from exploiting neutron measurements [11]. Transient fission times deduced from LCP multiplicities are not well established experimentally. Ikezoe et al. [21, 22] measured and analyzed pre-scission proton and α-particle multiplicities without any reference to nuclear dissipation, using a standard statistical code [23] for energy spectra and multiplicity fits. Standard statistical models manage to describe fission data, however, above a certain excitation energy strong dissipation is needed [24].

Gui et al. [25] studying proton and α-particle emission proposed a decreasing scission time from ~ 10 zs to ~ 0.5 zs as the mass-asymmetry decreases in the range $A_H/A_L = 4.8$ to 1.0. The corresponding excitation energies at scission are found to decrease from ~ 2.2 to 0.6 MeV/nucleon. Siwek-Wilczynska et al. [26], on the contrary, suggested even a slightly longer time for asymmetric ($A_H/A_L = 1.6$) fission comparing pre-fission

[1] 1 zs $= 10^{-21}$ s

multiplicities of α-particles observed in the reaction ^{40}Ar(9AMeV) + ^{232}Th, but due to large statistical uncertainties one can assume also that there is no fission time dependence on asymmetry. Charity [27], however, in the framework of the statistical model concluded that there is a strong dependence of the fission "delay time" on the mass asymmetry. Analysis of pre-saddle multiplicities and fragment charge distributions reveals that the system should spend a significant time for the saddle-to-scission transition. The fission pre-saddle time τ_{pre} and the saddle-to-scission transition time τ_{ssc} in the analysis of LCPs by Lestone was consistent with $\tau_{pre} = 9 \pm 6$ zs and $\tau_{ssc} = 22 \pm 7$ zs, implying that the hot system spends a considerable time beyond the saddle point. Rubchenia et al. [28] by the use of the neutron data from fission of ^{220}Th at E^*~40 MeV in the framework of the time-dependent statistical model also concluded that the hot fissioning nucleus spends a longer time beyond the saddle. Their estimation of the transient time amounted to 170 zs, and a tendency to shorten this time with increasing the excitation energy was deduced.

Time scales deduced from the GDR γ-rays are in strong contradiction with those usually obtained from light particle multiplicities. Recently, van't Hof et al. [29] have analyzed the energy spectra of the GDR γ-rays emitted from the compound nucleus ^{156}Dy at excitations energies $E^* \sim 0.7$ MeV/nucleon, and concluded that the fission time scale is of the order of 100 zs. V. Kamanin et al. [30] related GDR to the very early stages of reactions, especially with $E_\gamma > 30$ MeV. Mechanism of the GDR γ-emission is probably connected with the angular momentum dissipation. Measured time scales are then of course quite different from the fission ones. Adding to the controversy, Siwek-Wilczynska et al. [31] concluded that the fission time scale was indeed of the order of 100 zs when they confronted the neutron data by Hinde et al. [15] with simulations of a dynamical one-body dissipation model coupled to a time-dependent statistical model.

2.3 LCP emission studies

Different sources for the emission of γ-rays, neutrons, LCP and intermediate mass fragments (IMF) during the decay of the composite system are experimentally distinguishable due to, on the average, their different properties. However, the origin of a given particle being emitted can generally not be identified.

Emission of particles and γ-rays proceeds on quite different time scales, e.g. starting from bremsstrahlung before nuclear forces are active and up to the de-excitation of heavy remnants. Generally, in order to reach the high excitation energy of the compound-like system it is necessary to increase the incident energy. With the increase in the incident energy, more and more nucleons and complex fragments drop out of the further interaction due to the projectile break-up and pre-equilibrium emission [32]. Additionally, the multifragmentation channel opens already in the Fermi energy domain. This means that much more information can be obtained on the nuclear cohesion and nuclear response, as compared with the low energy region. Full understanding of those nucleus-nucleus collisions and, in particular, fusion-fission-like processes requires the inclusion of heavy remnants and both LCP and IMF data. The idea of a complete experiment led to the compromise principle of the FOBOS array being a *logarithmic detector* [6].

The bulk of data collected so far concerns sequential emission of LCPs and IMFs. The shape of their spectra has been well studied in selected experiments with high statistics and is well described in general by statistical models. The subdivision into LCP and

IMF by means of cutting $Z \leq 2$ and $3 \leq Z \leq 8$ is mostly operational, since they are complementary data.

Similarly to LCP data, the emission of IMF during fission has been recently studied in order to probe nuclear dynamics. Bowman et al. [33] investigated a variety of collisions at an incident energy of 50 AMeV and reported a strong dependence of element distributions and multiplicities of IMF on the LCP multiplicity. The importance of pre-equilibrium IMF emission is also deduced. Chen et al. [34] studied the reaction ^{4}He + ^{232}Th at the same projectile energy. The neck and isotropic component of IMF emission are separated by means of energy, angular and charge distributions. Similar data were obtained recently with the FOBOS detector. For instance, the isotopic composition of neck matter was found to be almost identical to that of the compound nucleus; however, sequential IMF have a composition in accordance with the β-stability systematics [35]. LCP data also distinguish between emitter configurations, therefore, the so-called near scission emission of α-particles is treated separately (see, for example, Siwek-Wilczynska et al. [26]). The above mentioned arguments clearly show the necessity to perform the LCP data analysis *together* with the analysis of IMF and massive fragments.

The "usual" sequential emission is found to lead to some unexpected results. Gui et al. [25] concluded, that symmetrically fissioning nuclei as light as $A \sim 180$ at E^* of about 3 MeV/nucleon in the initial state are cold at scission. This is because the time needed for the hot nucleus to change shape into two nearly equal sized nuclei is estimated to be ~ 10 zs. During this time, the very rapid evaporation of light particles can remove a large portion of the excitation energy, leaving the system relatively cold. The cooling down of a compound nucleus during the descent from saddle to scission has been observed recently with the FOBOS detector [35] in experiments described in the present thesis.

2.4 Contribution of FOBOS and motivation of further work

Mass-energy distributions of fission fragments of hot nuclei with excitation energies $E^* >$ 40–50 MeV in the fissility range of $Z^2/A = 20$–33 have been extensively studied in heavy-ion reactions [11] and a large amount of experimental data on the mass dispersions of fission products is collected within the so-called stiffness systematics [10]. The dispersion of a mass distribution σ_M is related to the effective nuclear temperature θ_{eff} in first approximation as

$$\sigma_M^2 = \theta_{eff}/q_{eff} \tag{2.1}$$

where q_{eff} is the parameter of stiffness with respect to mass-asymmetry deformations. The value q_{eff} can be calculated exploiting the liquid drop model. The diffusion model in [36] gives reasonable stiffness values also for high excitations $E^* > 80$ MeV and fissility $Z^2/A > 32$. The term "effective" reflects a substantial duration of the fission process.

The above described method is used to get information on the temperature of fissioning nuclei in the analysis of mass dispersion data measured with the FOBOS detector [35]. Hot heavy nuclei were produced by incomplete fusion in the reactions ^{14}N (34 AMeV) + ^{197}Au and ^{7}Li (43 AMeV) + ^{232}Th, and the mass distribution of binary disintegration has been investigated using the 4π-array FOBOS.

First of all, the correctness of the mass and excitation energy determination was

checked [37]. A decrease in total mass (fragment mass sum) with an increase in linear momentum transfer (LMT) has been observed. This is caused by enhanced particle evaporation, since within a massive-transfer approach LMT is used as a measure of the excitation energy E^* (fig. 2.1, left panel). The obtained value of 13 MeV per lost nucleon agrees well with that from direct measurement of particle multiplicities [38].

At E^*=50–90 MeV, the fragment-mass distribution width, σ_m, reveals good agreement with the mass-asymmetry stiffness systematics represented by the solid line in fig. 2.1 (right panel). However the rise of σ_m at higher excitation energy was found to be considerably smaller. The narrowness of the mass distribution is attributed to the relatively long saddle-to-scission transient time, allowing the system to substantially cool down by evaporation of light particles [35]. However, a steep rise of the mass distribution width at E^*>250 MeV cannot be accounted by the interplay between the nucleus' heating and the removal of excitation energy by the particle evaporation.

A preliminary analysis of the mass dispersion data obtained from the reaction ^{14}N (34 AMeV) + ^{197}Au produces θ_{eff} ~2.3 MeV when applying q_{eff}=0.009 MeV/amu^2 in the saturation region. The average duration of the cooling cascade in the reaction ^{7}Li (43 AMeV) + ^{232}Th, where the cooling effect was observed for the first time [37], is consistent with the time of ~60±20 zs [7]. In this respect the related temperature measurements from the LCP data (corresponding to an earlier decay stage) become of top interest.

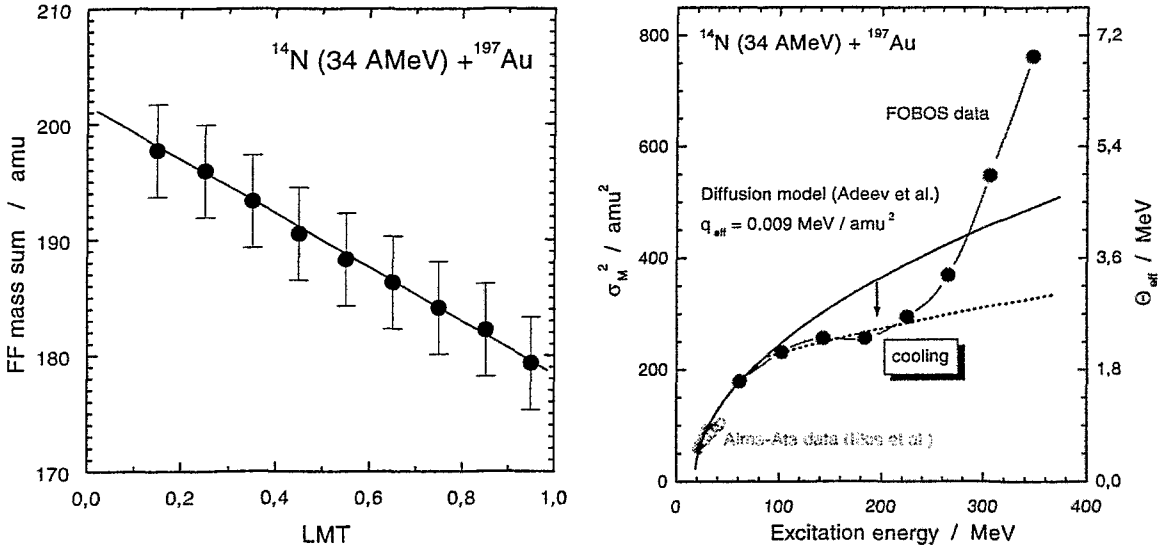

Figure 2.1: *Left panel: Linear correlation between LMT and average total mass. Right panel: Saturation of the mass dispersion at E^*=100-250 MeV. Dashed line is an eye-guide.*

The analysis of the fragment mass distribution reveals two components with essentially different mass dispersions (fig. 2.2). The first narrow component qualitatively follows the stiffness systematics. The second broadened component becomes notable at E^*~ 250 MeV and is predominant at 350 MeV. Mass distributions corrected for geometrical acceptance effects have been created in dependence on E^* (fig. 2.2, left panel). The widths of these spectra steadily increase with increasing E^*. The data have been fitted by a sum of two Gaussians with dispersions of the components taken from the distributions at the extremes of E^*. One observes, that at E^*≈140 MeV the contribution of the broad component is

about 10%. It steadily increases with increasing E^*, whereas the yield of the narrow component reaches its maximum near E^*=250 MeV and then decreases again (fig. 2.2, right panel). It was concluded, that a substantial change in the two-fragment decay mechanism of hot nuclei was observed. A valid argument was found for distinguishing between the two superimposed processes, namely between *ordinary fission* and *hot binary fragmentation* (BF)[39]. One can expect a manifestation of these trends also in the LCP emission channel.

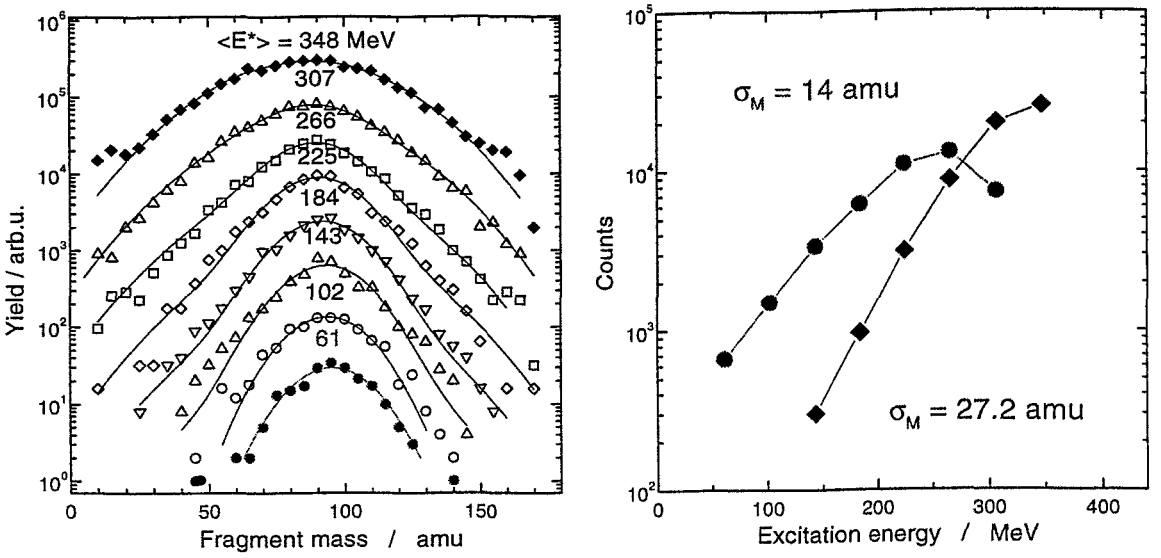

Figure 2.2: *Left panel: The experimental fragment mass distributions for excitation energy bins can be fitted by the sum of two gaussians. Right panel: Dependence of the amplitudes of these gaussians on excitation energy.*

2.5 Particular tasks of this thesis

The analysis of the experimental data obtained to date nourishes great hopes that LCP data from the FOBOS scintillator shell especially in combination with the forward phoswich array can deliver vital physical information which can be used in the sense of a nuclear "clock", nuclear "thermometer", or "calorimeter". It could probe the nucleus shape and can be used as an entrance channel filter. The complexity of the studied subject and the experimental equipment require, however, to pay particular attention to the reliability of the data and the limitations of the used methods. It has been numerously highlighted, that the implicit averaging over a large number of reaction channels plays a significant role in the Fermi energy domain. Therefore, even assuming a good separation of the incomplete fusion and subsequent fission from other reaction modes, one should take into account this averaging before interpreting any data.

The present thesis contains for the first time an analysis of the LCP data obtained from the FOBOS scintillator shell and the prospects of more advanced investigations are shown. First of all, the data derived from gas detectors (masses, coordinates, LMT etc.)

should be checked by proper correlations with LCP-observables. The effects observed in the massive fragment analysis could be reflected in the LCP data.

General problems to be solved in connection with the present thesis are as follows:

- to set up and put into operation the scintillation shell [2];
- to develop and test methods of data analysis and, first of all, methods of energy calibration adequate to actual experimental conditions;
- to perform full scale measurements, delivering the LCP data;
- to demonstrate the reliability and consistency of the measurements;
- to extract the temperature of emission sources and the associated LCP multiplicities;
- to search for indications of the dependence of the fission time on mass-asymmetry.

The following experiments aiming in particular at that tasks have been performed.

The September'95 experimental session (incomplete FOBOS configuration)
^{14}N (34 AMeV)+^{197}Au

The June'96 experimental session (commissioning of CsI-shell)
^{14}N (53 AMeV)+^{197}Au

The January'96 experimental session (complete FOBOS, but without ARGUS)
(to be called in the following as JAN96)
^{14}N (53 AMeV)+^{197}Au
^{14}N (53 AMeV)+^{232}Th

The March'97 experimental session (complete FOBOS, together with ARGUS)
(to be called in the following as MARCH97)
^{40}Ar (36 AMeV)+^{248}Cm
^{40}Ar (36 AMeV)+^{nat}Ag

In all above sessions thin spectrometric targets (100-300 μg/cm^2 deposited on C or Al_2O_3 backing) were exposed to a beam of several units (2-3) of 10^9 ions/s.

The present thesis is mostly based on data obtained during the January'96 session. There are approximately 2×10^6 selected binary fission events available for the analysis for each reaction, including $\sim 1\%$ of ternary events.

[2] this is a small violation of the chronology – the idea appeared some years ago

Chapter 3

The experimental setup

3.1 Design of the FOBOS detector

The 4π fragment spectrometer FOBOS [6] is set up at the Flerov Laboratory of Nuclear Reactions of the Joint Institute for Nuclear Research in Dubna at the beam of the isochroneous cyclotron U-400M [40] recently supplied with an ECR ion-source [41]. FOBOS was finally completed in 1996 and a series of full-scale experiments has been performed.

]

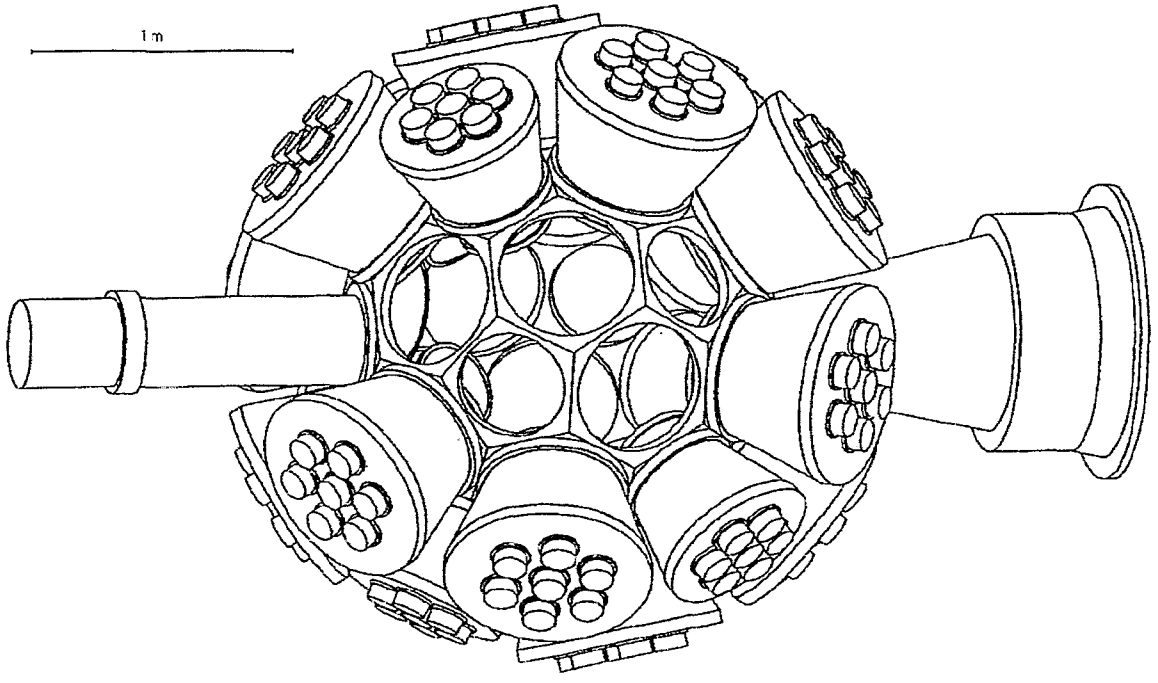

Figure 3.1: *General view of the FOBOS central vacuum chamber with some inserted detector modules. The beam enters from the left side. The exit cone at the right side houses the forward array.*

The spectrometer is designed for studying reactions at incident energies of 10-100 AMeV in direct kinematics, i.e. a light projectile impinges upon a heavy target nucleus. The decay of a compound-like system from such reactions is characterized by the following

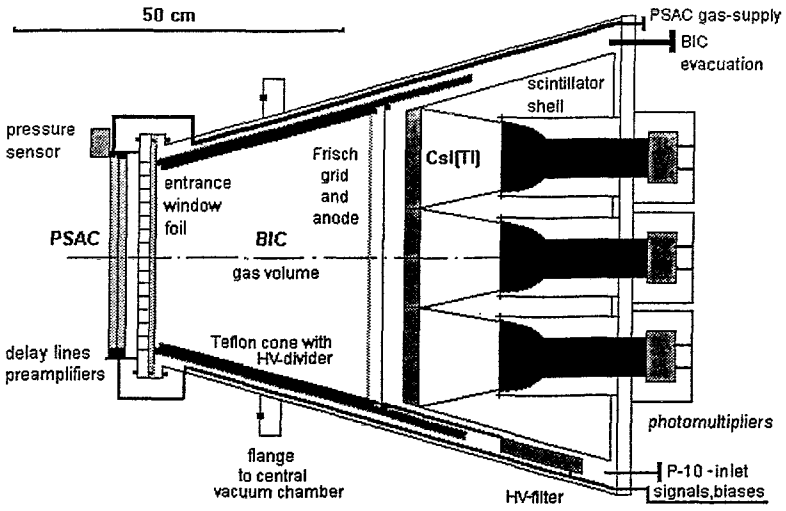

Figure 3.2: *General layout of a FOBOS detector module.*

products: 1-3 heavy fragments (e.g. fission fragments (FF)or heavy residues (HR)), few intermediate mass fragments (IMF),conventionally defined as being heavier than α-particles but lighter than FF, a fairly large number (10-30) of neutrons and 5-10 light charged particles (LCP).FOBOS is able to register *charged* reaction products only, from protons up to HR.

The intention to perform exclusive spectroscopy of charged fragments within a broad dynamic range, covering large intervals of atomic number (Z), mass number (A), and simultaneously a considerable part of the solid angle of 4π as well, requires some reasonable compromises between registration efficiency, detector granularity, detection thresholds, possible counting rates etc. For this purpose, the so-called *logarithmic detection principle* is applied. This principle assumes a successive increase of the stopping power along the flight path of the particles. This principle has been used in the construction of experimental setups such as PAGODA [42], INDRA (Ganil) [43], FOPI (GSI) [44].

Due to reaction kinematics, most of the ejectiles are directed into the entire solid angle. Therefore, the basic geometry of the detector set-up turns out to be a sphere surrounding the target.

The general lay-out of the spectrometer FOBOS is schematically shown in fig. 3.1. The central vacuum chamber has an inner diameter of 1330 mm [45]. From outside the basic shape is a precisely manufactured ($\pm$0.2 mm) 32-face truncated icosahedron with circular holes in the centers of 20 regular hexagonal ($\varnothing$480 mm) and 10 regular pentagonal ($\varnothing$380 mm) surface elements for mounting the 20 large and 10 small detector modules, respectively. Two of the oppositely placed pentagons of the central vacuum chamber are used for beam entrance and exit.

The spectrometer FOBOS consists of three consecutive shells of particle detectors and a more granular forward array. One position-sensitive avalanche counter (PSAC),one axial Bragg ionization chamber (BIC),and a mosaic of 7 CsI(Tl) scintillators (CIS) are arranged in 30 separate detector-modules [46] which are mounted onto the central vacuum chamber from outside. The sketch of a module is shown in fig. 3.2. Groups of detector modules are placed axial-symmetrically at the same polar angle with respect to a beam

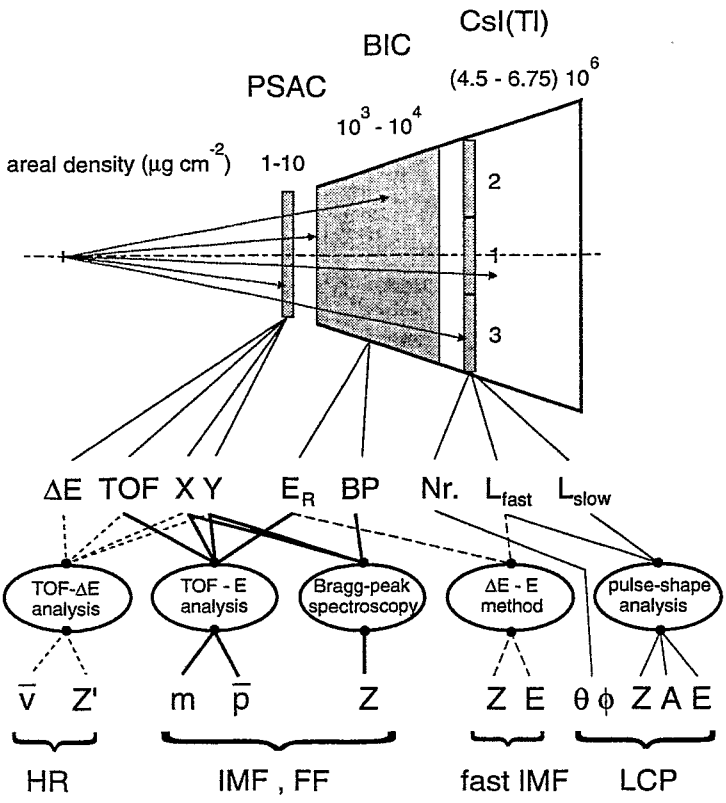

Figure 3.3: *Parameters of charged particles, measured or derived from the signals delivered by a detector module. Different methods of analysis are applied, if (see the lower part of the figure) (i) only the PSAC has fired (dotted lines), (ii) the PSAC and BIC have fired (thick solid lines), (iii) only a CsI(Tl)-detector (1,2,3, ... 7) has fired (thin solid lines), and (vi) the BIC and a CsI(Tl)-detector have fired (dashed lines). The logarithmically increasing stopping power of the different detector shells is illustrated by the given mean areal densities of the detector materials of the PSAC, BIC, and CsI(Tl)-crystals for typical experimental conditions.*

thus forming six detector rings at $< \theta >= 37.38°$, 63.44°, 79.19°, 100.81°, 116.56° and 142.62°. (See tab. A.1 and fig. 4.3 for details).

A relatively long flight path of 50 cm between the target and the inner detector shell of PSACs is available for a precise time-of-flight (TOF) and coordinates (θ, ϕ) measurement of fragments with $Z > 2$. Analysis of TOF and pulse-height (ΔE) information from a PSAC provides a rough Z-identification of heavy species not reaching the next detector shell, e.g. evaporation residues (HR).

The second detector shell consists of axial Bragg ionization chambers (BIC) which register the full energy-loss distribution (Bragg-curve) of the fragments stopped within the gas-volume. The residual fragment energy (E_R) and the magnitude of the Bragg-peak (BP), as a measure of Z, are directly derived. From the TOF- and the E_R-information the masses m_i of the fragments can be calculated applying a suitable correction procedure which takes into account the different energy losses in penetrated detector materials. Hence, the momentum vectors $\boldsymbol{p_i}$ can be derived independently for each fragment "i" event-by-event. This feature is a necessary condition for an exclusive measurement.

Since the PSAC and BIC are not sensitive to low-ionizing LCP (Z=1-2), a third, more granular, shell of CsI(Tl) scintillation detectors [1] is arranged behind them. The LCP are analyzed by their signal pulse-height and -shape. Fast LCP do not affect the registration of fragments in the PSAC and BIC. Therefore, the correlations between fragments and LCP can be studied for all possible relative angles. Furthermore, the well known ΔE-E-method can be applied for the identification of high-energetic IMF which penetrated the BIC and are stopped in the scintillators.

The parameters of a particle, measured or derived from the signals delivered by a FOBOS module, are schematically drawn in fig. 3.3. In addition, an array of phoswich detectors is placed inside the central vacuum chamber covering forward angles of $\theta = 4.5°$-$26°$. It provides registration of LCP and projectile-like fragments (PLF) by means of a principle similar to that for CsI(Tl) scintillators.

It has to be mentioned, that a similar 4π-array for charged fragments has been built at the Cyclotron Laboratory of the Michigan State University, East Lansing, USA [47]. The concept of the spectrometer FOBOS resembles it in general design, and several detection principles applied at these two devices are almost identical.

Two advantages of the FOBOS detector concept should be emphasized:

- The long flight path and the excellent timing properties of the PSAC make it generally possible to apply the TOF-E_R method for the mass determination of the fragments instead of the ΔE-E-method which has its natural energy limits caused by the ΔE-detector. In other systems heavy fragments (FF, HR) often cannot be identified, e.g. at the 4π-array INDRA [43] where small ionization chambers deliver the ΔE-information, but timing cannot be used, or at the MSU 4π-array [47] where the compact detector design requires thicker entrance windows of the BIC leading to considerably higher registration thresholds.

- The excellent spatial resolution of the PSAC together with the mentioned principle of mass determination provides a more precise determination of the linear momenta of the fragments.

3.2 Position-sensitive avalanche counters

Following the general construction the PSACs of the first detector shell form a truncated icosahedron-like shape at a distance of ≈50 cm from the target. The hexagonal- and pentagonal-shaped frames of PSACs are mounted separately in front of the BIC entrance windows on big and small modules, respectively.

The PSAC are based on the principles described in ref. [48]. Three thin Mylar foils (1.2 μm) serve as cathode and entrance/exit windows. The central cathode-foil is covered by 40 μg /cm^2 thick Au-layers. It delivers the timing signal. Two perpendicular wire-planes (made of 30 μm thick Au-plated W, spaced by 1 mm) are positioned at both sides from the common cathode at the distance of 3 mm $\pm$50 μm . They serve as coordinate grids. The window foils are glued to special frames which can be changed individually in the case of leakage. The transparency of the PSAC amounts to 92%. Their sensitive areas

[1] Their detailed description is given in the next chapter because it was an essential part of this thesis to assemble and put into operation this scintillator shell.

are circles of a diameter 327 mm and 243 mm for the large and small detector modules, respectively. A total solid angle covered by the PSACs amounts to 7.1 sr (56.5% of 4π). The spatial resolution of the PSAC amounts to $\Delta x = \Delta y \approx 1.5$ mm.

The counter-gas is pentane at a pressure between 200 Pa and 800 Pa. A high voltage level is chosen for an effective registration of heavy fragments with a threshold of $\approx$0.05 AMeV. The efficiency of registration drops for α-particles at energies of $\geq$1.5 AMeV because of the decreasing energy loss in the sensitive volume.

A rough selection of heavy fragments by their mass can be carried out using the ΔE *vs* TOF scatterplot of the PSAC, delivering also the information on correlated and random events, which is necessary in the case of a pulsed, micro-structured ion beam.

The timing resolution amounts, typically, to $\approx$200 ps FWHM if only a small central area of the counter is irradiated. When the whole sensitive area is exposed, the resolution becomes worse by a factor of about three. However, a special coordinate-dependent correction allows to determine the TOF of the fragments with an accuracy of $\approx$300 ps. In addition, the PSAC electronics can withstand a considerable high δ-electron background ($\approx 10^7$-10^8 s^{-1}) correlated with the beam bunches.

3.3 Axial ionization chambers

The principle of a BIC was first described in ref. [49]. Since the electric field is parallel to the direction of the incoming particles, the registered pulse-shape of a fragment stopped in the BIC gas-volume represents the image of the specific energy loss along the ionization path, which is characterized by the Bragg-curve. The integral of the electronic charge created is proportional to the energy (E_R) of the fragment, and the maximum of the ionization-density distribution of the fragment along its stopping path (Bragg peak height, BP) is a smooth function of Z. A special, new processing method has been developed which derives the E_R- and BP-values directly from a digitized signal [50] (see also Section 3.5). An example of a BP *vs* E_R scatterplot is shown in fig. 3.4. The charge resolution obtained around Z=13 is $Z/\Delta Z$=65. Elements are resolved from He up to $Z \approx 26$ (Fe).

A sketch of the lay-out of the detector module is shown in fig. 3.2. The conical shaped BIC have apertures of 260.0 msr (large module, $\oslash$385 mm, $\Delta\theta = 33.08°$) and 167.8 msr (small module, $\oslash$285 mm, $\Delta\theta = 26.54°$). The entrance windows are made of 1.5-3 μm thick aluminized Mylar. The total solid angle covered by the BICs amounts to 6.88 sr (54.7% of 4π).

The sensitive depth of the BIC is 250 mm. To withstand the pressure of the working gas, the delicate window foil, which at the same time serves as cathode, is supported by a twofold structure, i.e. an etched Ni-mesh with cell dimension of 2.7 mm carried by a solid concentric grid with a transparency of 94%. Otherwise, the extremely thin foils would not withstand gas pressures up to 100 kPa needed to stop most of the IMF within the sensitive depth. This mesh, however, reduces the transparency of the entrance window to 75%, causing a serious reduction of the effective solid angle of the spectrometer.

The shaping of the axial electric field is performed by 5 mm spaced Cu-strips coated on the inner side of the conical Teflon insulator [51]. The Frisch grid is placed 10 mm in front of the anode. It consists of two perpendicular wire-planes (50 μm thick Cu-Be spaced by 1 mm). The anode is a 10 μm thick aluminized Mylar foil. In typical experiments the BICs are filled with a P-10 gas-mixture (90%Ar+10%CH_4) at a pressure of 20–40 kPa

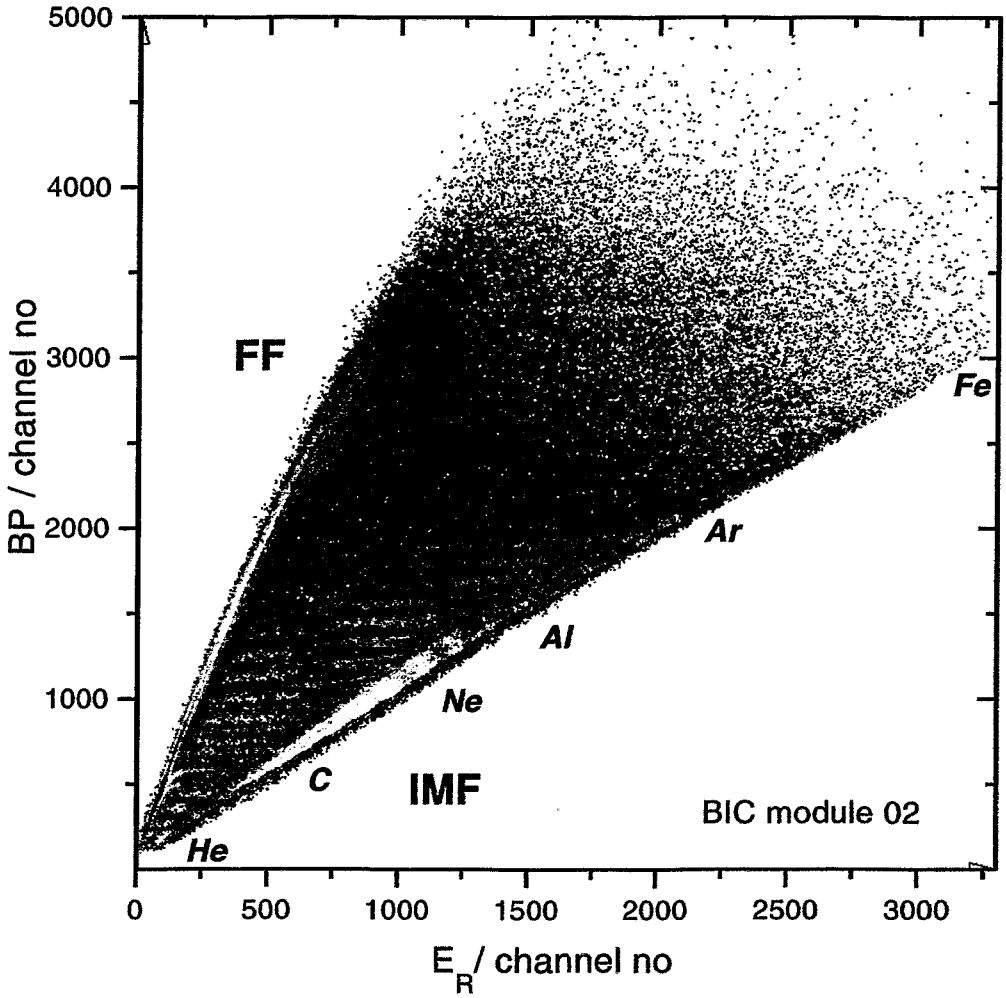

Figure 3.4: *Scatterplot of Bragg peak-height (BP) vs residual energy (E_R) for fragments measured by a BIC for the reaction ^{40}Ar (36 AMeV)+^{248}Cm. Branches of resolved elements are clearly visible (FF – fission fragments; IMF – intermediate mass fragments).*

and are operated with an anode voltage of 1.5–3 kV. At the design limit of 100 kPa this voltage reaches 8 kV.

The PSAC foils and the BIC window foil together cause a dead layer of $\approx$ 510 μg /cm^2 for fragment spectroscopy. For the registration of FF, having typical energies of 0.5–1.5 AMeV, the residual energy threshold amounts to $\approx$ 0.3 AMeV. An energy resolution of the BIC of 89 keV has been achieved for ^{238}Pu α-particles. In order to maintain the energy resolution during long-time experiments, the P-10 gas is mixed on-line and the gas composition is permanently controlled [52]. The gas-supply/vacuum system is computer controlled [53].

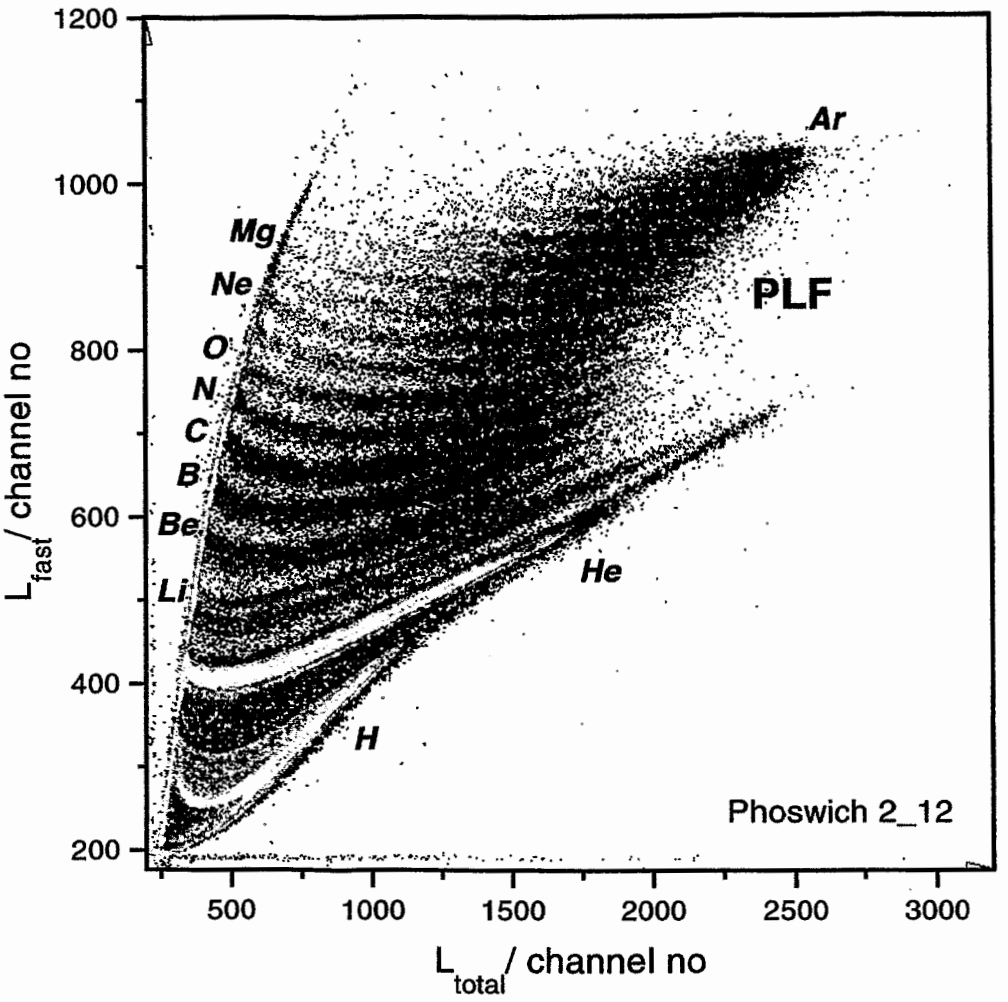

Figure 3.5: *Charged-particle identification matrix as measured by a phoswich detector of the forward array at $\theta = 8°$ for the reaction ^{40}Ar (36 AMeV)+^{248}Cm (PLF – projectile-like fragments).*

3.4 Forward array

For geometrical reasons the smallest acceptance angle of PSAC and BIC of the FOBOS spectrometer is $\theta \approx 21°$. Forward-directed fast reaction products are not registered by the gas detectors. Therefore, part of the former ARGUS detector array [54] has been modified for use as a forward array of FOBOS. It has been installed inside the central vacuum chamber through the forward (exit) cone (fig. 3.1).

The forward array consists of six concentric rings of altogether 92 phoswich detectors, each being a combination of a 0.5 mm thick fast scintillator (Pilot-U) and 20 mm thick slow BGO scintillator (phoswich detector) read-out with one PM. The detector geometry of the forward array is the following: one ring of 12 detectors at $< \theta >= 5°$ and 5 rings each of 16 detectors at $< \theta >= 8°$, 10.5°, 14°, 18.5° and 23.5°. The outer ring of the forward array slightly overlaps with the BIC positioned in forward direction at $< \theta >= 37.4°$. The phoswich detector allows to stop protons (α-particles) with energies

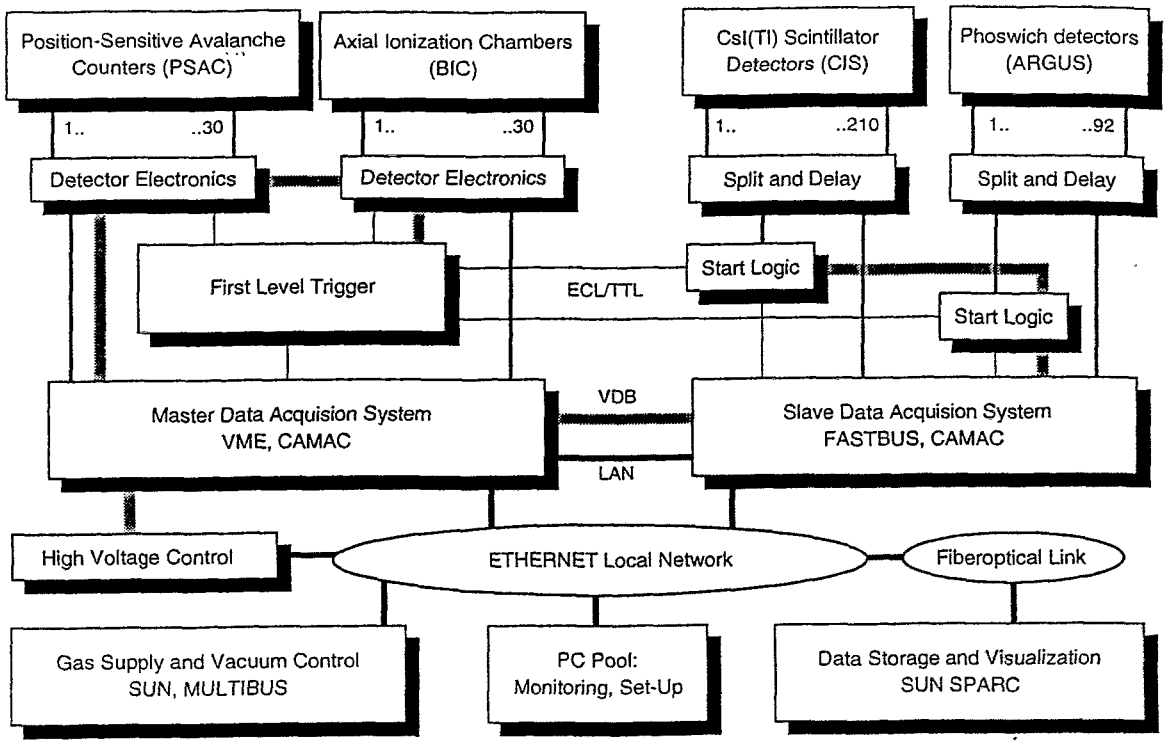

Figure 3.6: *Electronic systems and computer net of the FOBOS setup.*

phoswich light pulse (L_{total}) by an analog differentiation of the photomultiplier current signal. Only two integration gates ($\Delta t_{fast} = 100$ ns and $\Delta t_{total} = 400$ ns) common for all phoswich detectors are necessary [56].

A particle-identification matrix (L_{fast} *vs* L_{total}) of a phoswich detector representing PLF from incomplete fusion of ^{40}Ar (36 AMeV) with ^{248}Cm is given in fig. 3.5. Fast PLF can be observed at all possible Z, and also broad particle branches of H- and He-nuclei. Since the element resolution of a phoswich detector strongly depends on the exact setting of the integration gate for the fast component, a slightly worse resolution compared with the case of using individual integration gates for each detector [54] is expected. However, this read-out system is very compact and less expensive.

3.5 Data acquisition system hardware

The simplified structure scheme of the FOBOS electronic systems together with the local computer net is shown in fig. 3.6. A detailed description of the system is given in [57].

The electronics of the gas-detectors occupies ten CAMAC crates housing the special digitizing electronics (8 crates) and the control logic together with some service modules (2 crates). Splitter and delay boxes and CIS-electronics (4 crates), and FASTBUS mini-crate are used for the photomultiplier read-out of the scintillator shell and the forward array.

In order to minimize expense and occupied volume special CAMAC blocks (Bragg digital processors, BDP) have been designed in the Research Center Rossendorf for the

BIC data [50] processing. The BIC signal is shaped with a short time constant (τ=0.2 or 0.4 μs) in a spectroscopic amplifier and digitized by an 8-bit flash-ADC with a quartz-stabilized sampling frequency of 10 MHz. When a signal is recognized by the threshold comparator, two special arithmetic units extract the values for E_R and BP from this digitized curve. The control logic provides the coincidence condition with respect to the PSAC, a pile-up inspection, and the connection with the first-level trigger.

The first-level trigger signal of FOBOS [58] is usually generated by the gas detector part, and the scintillators are read-out in the slave mode. However, a trigger signal can also be generated by the scintillator shell and/or the forward array. The entire TTL/ECL-based hardware of the trigger logic fills one CAMAC crate. The logic delivers either the LAM demand ("look at me") for data storage or a general RESET if the event inspection leads to a rejection of the event.

Provided the BDP is not busy, a timing signal of the corresponding PSAC passes a special blocking and pile-up inspection unit (LBIN) connected with the control logic of the BDP, opens an event gate of Δt=200 ns duration, sets a bit in the coincidence pattern register and starts a TDC which will be stopped by the next RF-signal from the cyclotron. The event pattern is analyzed by a majority coincidence unit connected with the central event selector which induces a LAM demand if a preset multiplicity condition was fulfilled and there was no signal pile-up.

After a LAM demand has been recognized, the VME processor reads the coincidence pattern register first and then the conversion results of the TDCs (TOF) and BDPs (BP, E_R) which had fired. Subsequently, the QDCs of the scintillator shell and the forward array are serviced. The blocking signals of the LBINs are then removed, and the system waits for the next event.

The counting rates of events of different fragment multiplicity naturally differ by orders of magnitude. A special unit (major divider) which allows to modify the accepted rates concerning the event multiplicity has been developed to optimize the data storage.

All CAMAC- and FASTBUS-crates are connected with a main VME crate by means of the parallel VSB Differential Bus Extension (VDB). The VDB is well suited for multi-crate systems where different bus standards have to be controlled. The CAMAC-to-VSB interface is a single-width CAMAC crate controller STR 610/CBV [59] driven from the VME Subsystem Bus (VSB) via the VSB Differential Cable. The specification of the CBV is similar to the CAMAC crate controller of type A1. It maps a portion of the VSB address space to the CAMAC (C,N,A,F) and generates single CAMAC cycles from each proper VSB cycle.

The FASTBUS mini-crate contains a 68030-processor board (CERN Host Interface, CHI), an I/O-Port, a LAN Ethernet module [59] and six 96-channel FASTBUS QDCs (4 of the C.A.E.N. F683C [60] type for CsI-data and 2 of the LeCroy [61] type for phoswich-data). The VSB I/O-port provides an efficient interface between the CHI and the VME workstation where the CHI is operating in the VDB-slave mode. The CHI data memory is directly mapped into the local VSB address space, and the EUROCOM-6 processor module is treated in the same manner as any local memory.

A single-board computer EUROCOM-6 with a 68030 CPU builds the event data blocks [62]. The VME workstation sends the data blocks via Ethernet (LAN) and a fiberoptical link to a SUN SPARC-station 10 which records them to the mass storage memory event-by-event. The maximum data rate with respect to the gas-detector part of FOBOS is about 200 kbyte/s. Due to the conversion time of the FASTBUS QDCs (1 ms) rates of

50-100 kbyte/s are typical for the whole spectrometer. Therefore, the maximum permitted counting rate of FOBOS becomes 500-1000 events per second. It is mostly restricted by other experimental considerations like the rate of random coincidences etc.

3.6 Experimental data structure and software

The EUROCOM-6 and the CHI are operating under the Microware real-time operating system OS-9 (professional). All time-critical tasks are moved to the module processors. The data acquisition control program TINH [63] runs on the SUN SPARC-station 10. Quasi-on-line monitoring of the recorded data is performed using several PC AT as well as X-terminals and the ATHENE data analysis software [64, 65], which via LAN organizes a direct access to the data just written to the disk memory of the SUN SPARC-station 10.

The data file structure is characterized by sequential event storage into closed blocks of fixed length (512 bytes). A header contains information on defined parameters. The list-mode data structure is adopted from the VMS-based data acquisition system HOOPSY [66] in order to use the available OLYMP data analysis package [67]. It is module-oriented information on fired detectors, listed by number in an event-pattern register. Up to 10 parameters can be assigned to be read out per one pattern bit, and altogether 2000 parameters can be handled by the program TINH as well. A valid event is characterized, on average, by 20-30 parameters which are stored within ≈ 2.5 ms.

The PC-oriented ATHENE code [64] was especially designed for a distributed analysis of the data obtained at the FOBOS spectrometer using IBM PC of a type AT 386 and higher. The program allows to read data written in the formats of the programs CAMDA [68], HOOPSY and OLYMP. Special transformation algorithms to read data written in other formats are available. The version for 16 megabytes of XMS-memory is capable to accumulate and to visualize simultaneously 20 ordinary histograms together with 50 color scatterplots (350×350 cells). The new and more powerful version ATHENE94 [65] written in the object-oriented language C++ has been developed for real-time data processing on computers with UNIX-like operation systems and an X-WINDOWS environment.

The first step of the data processing consists in sorting out the so-called single-files containing information on each fired detector separately. This reduced subset of the primary experimental data is used for calibration purposes (see [6] and refs. therein). The calibration is performed by utilizing specially developed software, except of stopping power calculations.

Finally processed experimental data are transformed into a particle-oriented structure. This means, that each event is represented by a set of particles of a certain type and velocity vector or/and energy and angular coordinates, where the fired detector number is also a parameter. Some calculated event-values are also added to the data (multiplicities, transferred linear momentum components etc).

Chapter 4

Scintillator shell of the FOBOS detector

4.1 Design of the scintillator shell

The scintillation process is studied, and photomultiplier-coupled scintillation detectors are widely used for the registration of ionizing radiation for about fifty years [69]. In particular, inorganic CsI(Tl) crystals have some attractive features. They are mechanically rugged, plastic, easily machinable and only slightly hygroscopic. The relative compactness of CsI(Tl) counters due to the large stopping power of the scintillator, the high scintillation efficiency due to low quenching, and, last but not least, the market price make CsI(Tl) one of the most appropriate scintillating materials for the detection of light charged particles and medium mass ions in nuclear research [70, 71]. The CsI(Tl) material has a moderate dependence of the light output on the crystal temperature of 0.28%/K in an usual temperature range (to be compared with –0.73%/K for BGO) [72]. Mainly these reasons caused the choice of CsI(Tl) for the scintillator shell [73] of the 4π-array FOBOS [6].

The shell of CsI(Tl) scintillator (CIS) detectors is arranged behind the BIC to register less ionizing LCPs and energetic IMFs which penetrate the gas-filled detectors. It consists of 210 hexagonal-shaped large-area crystals covering angles $\theta \approx 19° - 162°$. The geometrically covered solid angle is 5.6 sr, the effective solid angle amounts to about 4 sr because of the reduced transparency of the inner detector shells. The angular resolution is limited by the dimensions of crystals to $9° - 11°$. Mosaics of 7 CsI(Tl)-crystals are grouped together with their light-guides and photomultipliers inside the BIC cases covering 84% of the BIC aperture. Rubber rings pressed to the phototubes serve as seals between the gas-volumes of the BIC and the atmosphere.

The LCP-identification is carried out by applying the pulse-shape analysis method [74]. Governed by the intrinsic features of Tl-activated CsI the pulse-shape of the scintillation light depends on the ionization density produced by the incoming particle. The pulse-shape is characterized by several components of different decay times. The decay time of the fast component (τ_{fast}) and the ratio of magnitudes of the major slow component to the fast component (h_{slow}/h_{fast}) are smoothly decreasing functions of the stopping power (dE / dx) [75].

Signals from photomultipliers are integrated within two time gates in accordance with the pulse processing necessary for the pulse-shape analysis (PSA) [76]. Due to the particle-

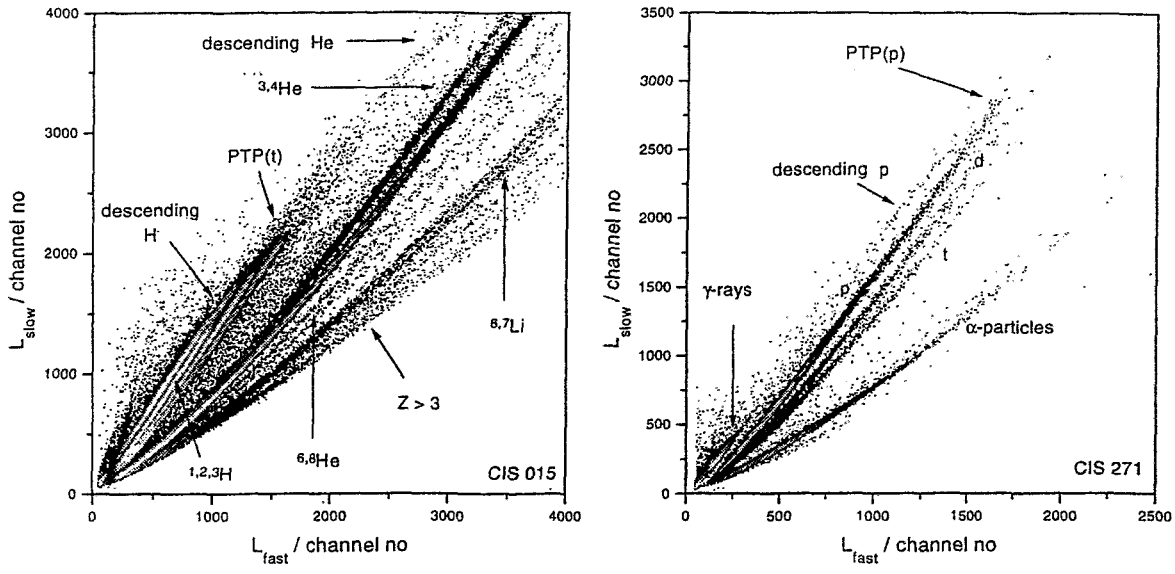

Figure 4.1: *Examples of the best particle identification matrixes at the utmost forward (left panel) and backward (right panel) angles. A very good particle resolution is achieved for $Z < 3$, punch-through points (PTP) for H isotopes are easily recognizable. A descending branch consist of particles piercing a crystal. Because of the large amplification applied for backward oriented crystals a γ-line appears above threshold.*

and energy-dependent decay constants of CsI(Tl) ([75, 74] and refs. therein), the best LCP separation in the particle identification matrix (PIM) is observed with the time gates $\Delta t_{fast} = 0$ to 400 ns and $\Delta t_{slow} = 1600$ to 4600 ns. Initial values for these gates were estimated by simulations like those made in ref. [75] (Appendix, fig. B.1). Real experimental conditions (timing, trigger logic etc.) in measurements with the whole detector array required some modification of these time gates.

LCP with $Z < 3$ are well separated with respect to their atomic and mass numbers. The scatterplots illustrating the LCP-identification and the particle branches in a particle identification matrix (PIM) are given in fig. 4.1. An *ascending* particle branch corresponds to completely stopped particles in a scintillator. Values of L_{fast} and L_{slow} parameters grow with particle energy. Those particles which punch through a crystal deposit only a small amount of energy and this portion decreases as the particle energy increase. These particles form an *descending* particle branch. There is no Bragg peak in a crystal from piercing particles, therefore their signals differ only in amplitude and all descending lines are overlapping.

The resolution for heavier particles $Z > 3$ is not as good. On the other hand, the efficiency of $Z > 2$ registration in gas detectors is high (hydrogen is not seen in PSAC at all, except only for fairly high voltage). If particles pierce a BIC their lines in the BIC plot (E_R *vs* BP) are overlapping. The particle identification of such energetic IMF can be performed applying the ΔE-E-method (fig. 4.7, left panel) using the energy loss in a BIC and the light output of the scintillator. By this means the dynamic range of the FOBOS detector is considerably enlarged for IMF spectrometry.

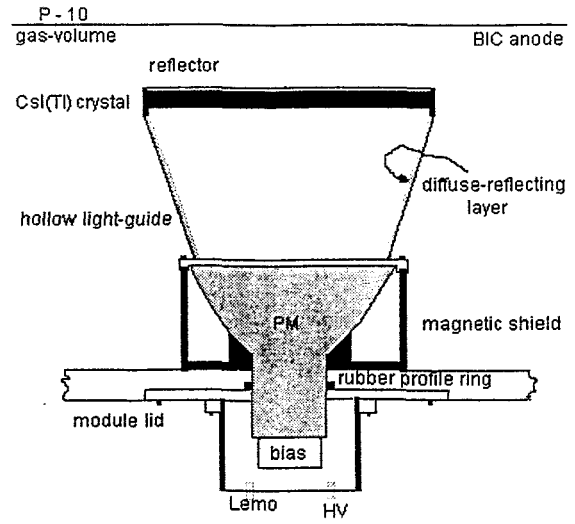

Figure 4.2: *Sketch of the general layout of a CsI(Tl) scintillation detector unit (CIS).*

4.2 Scintillation detector unit

A single CIS detector unit [77, 78] (fig. 4.2) consists of a large-area (260 cm^2 or 146 cm^2) crystal which is grown under vacuum applying Kyropoulos' method (MONOCRYSTAL-REACTIV Company, Kharkov, Ukraine) and a hollow diffuse-reflecting light guide coupled to a spectroscopic photomultiplier (SPM) of the type FEU-173, ⌀170 mm or FEU-167, ⌀120 mm (EKRAN Company, Novosibirsk, Russia). The photomultipliers are surrounded by cylindrical anti-magnetic shields.

The thickness of the CsI(Tl) crystals in forward-positioned detectors at polar angles of $\vartheta = 23^o$ to 52^o amounts to 15 mm, the other part of the scintillator shell in the angular range of $\vartheta = 53^o$ to 157^o consists of 10 mm thick crystals. These thicknesses allow to stop protons and α-particles with energies up to $\approx$ 64 AMeV and 51 AMeV, respectively (tab. 5.1)

The content of the Tl-activator in crystals amounts to 0.07-0.08%, which is an empirical optimum for high light output as well as good pulse-shape properties for LCPs. The samples of a regular hexagon shape were cut from the central part of ⌀500 mm ingots. In order to enhance the light output, the front side of the crystal is polished using organic solvents to avoid a dead layer at the surface. For the same reason it is covered with a 1.5–3 μm thick reflector foil of aluminized Mylar mounted at a distance of 3 mm from the surface. The rear side of the crystal is rough to avoid inner total reflection at the read-out surface and subsequent absorption losses of light. The output was measured to be nearly 30% higher as compared with double-sided polished crystals.

The photomultipliers have large area trialcali photocathodes with high photocathode sensitivity of typical 1.5–2.5$\times 10^{-4}$ A/lm and due to their spectral sensitivity range of λ=300–850 nm are ideally matched to the emission spectrum of CsI(Tl) ($\lambda_{max} \approx$ 500 nm).

The main problem of using large scintillators consists in the position dependent detector response induced by (i) the nonuniform light output of the crystal, (ii) the nonuniform photocathode sensitivity and photoelectron collection efficiency of the photomultiplier, (iii) the position dependent light collection efficiency.

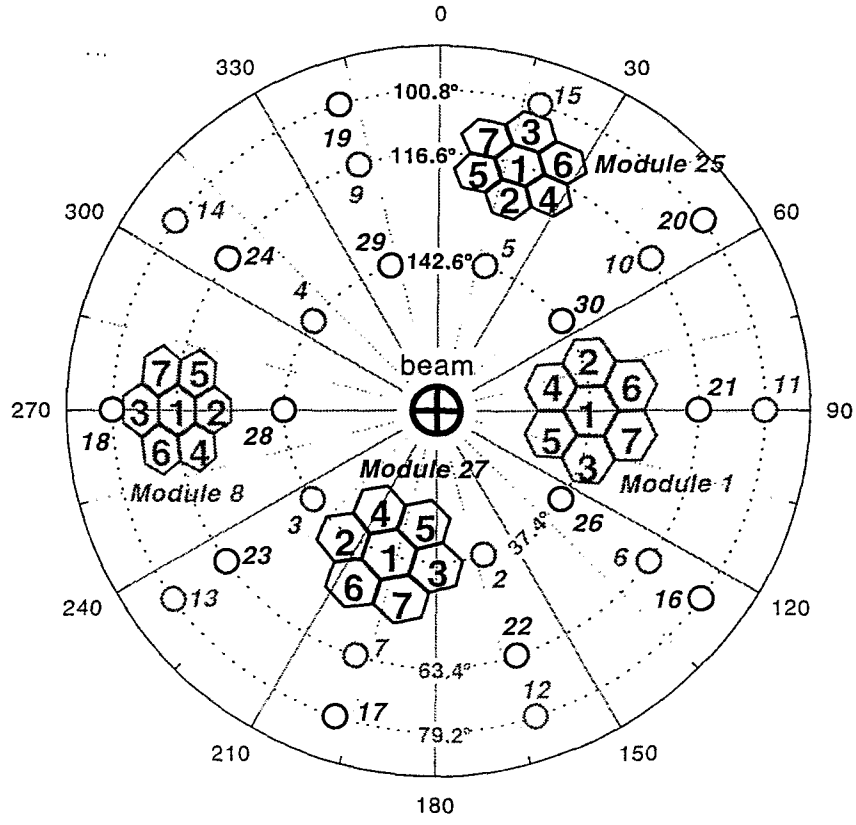

Figure 4.3: *The principle of the CIS detectors layout in polar coordinates. CIS detectors (four modules) and other module centers (circles) are shown as they can be seen from the backward hemisphere from outside towards the beam direction. Concentric circles correspond to polar angles of modules' centers. Gray contours, circles and letters correspond to the projection of the forward hemisphere.*

Scanning the crystals with the help of an α-source and collecting the light with a small diameter phototube, the radial non-uniformity of light output induced by the inhomogeneous dopant concentration was checked to be less than 2%. Coupling of a crystal with conventional plexiglas light guide leads to a very large radial variation of light collection up to a factor two. Monte-Carlo simulations of light transport were carried out for several types of light guides. The hollow light guide (hexagonal at the crystal side and round at the opposite end) with a diffuse-reflecting inner surface was found to be the best solution. It is made from zinc plated sheets of metal, painted with white TiO_2-based enamel solved in butanol with a boron acid admixture. The inner surface of the light guides have been pre-processed with a sand-jet for best adhesion. The reflectivity of the inner surface amounts to 90%. Such a light guide diminishes the position dependence of the light collection to about 5%. The light guide serves also as a crystal support allowing easy inclusion into a crystal mosaic.

Due to the rough read-out surface and the diffuse reflecting surface of the hollow light guide the serious radial nonuniformity of the photocathode response is smoothed due to a nearly homogeneous illumination and, therefore, its influence on the energy resolution is

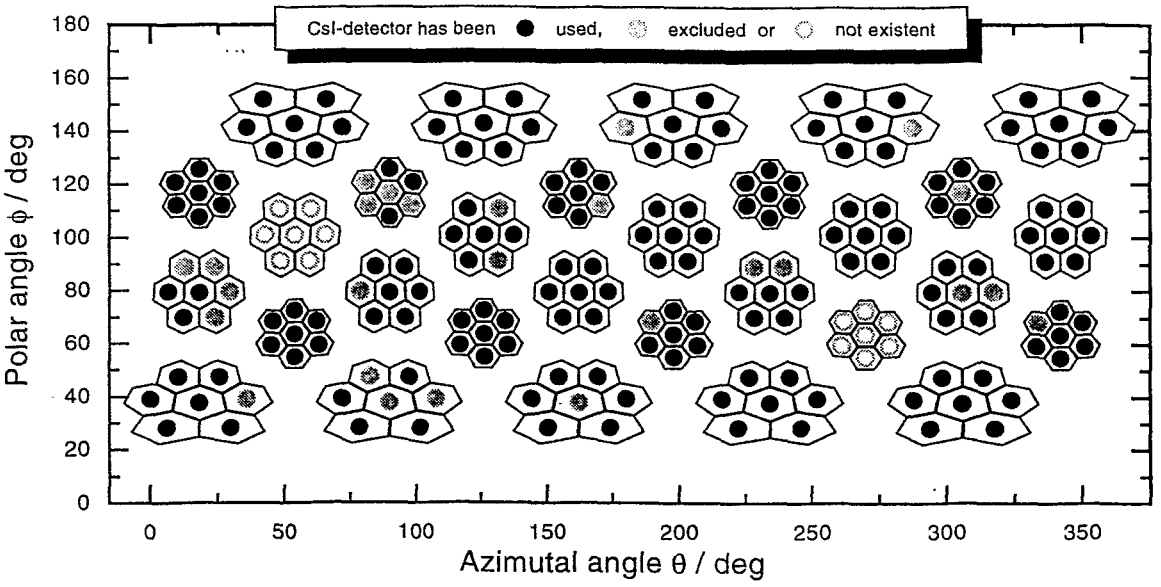

Figure 4.4: *The layout of CIS detectors in θ-ϕ-plane. Detectors marked with black spots have been used in a data analysis of the JAN96 experiment.*

minimized. The energy resolution for 5.5 MeV α-particles amounts to 6–7% for collimated particles and 9%, if the entire surface of the crystal is illuminated [77].

4.3 The geometry of the scintillator shell

The geometry of the CIS shell follows the modular structure of the gas-ball. The principle is illustrated in fig. 4.3. The numbering rule for individual crystals reflects the module number itself and the position of a crystal in a module related to its θ and ϕ coordinates.

Seven individual crystals in one module are placed side-by-side in a plane at a certain distance between their centers h (tab. 4.1) mounted together on a lid. The diameter d of a crystal is measured between opposite corners. The inner (central) crystal is placed at the distance R from the center of the FOBOS (the target position). Since the arrangement of the CIS-lids is also regular (as shown in fig. 4.3), the angular coordinates θ and ϕ of crystal centers can be calculated. The true center of an outer crystal in a lid differs from the visible one due to a geometrical perspective. The correction for the angle β between inner and outer crystals amounts to about 1%. This has to be taken into account also in the calculations of the solid angles of crystals Ω_{in} and Ω_{out}. These important parameters are collected in tab. 4.1. Angular coordinates of crystals are listed in tab. A.1 (Appendix). Oppositely positioned crystals' numbers are to be found in tab. A.2.

The layout of crystals in the θ-ϕ-plane is shown in fig. 4.4. Two modules (# 8 and 20) have not been plugged in during the JAN96 experiment, and some of detectors have been switched off or excluded from the processing mainly due to failing of a corresponding QDC-channel and only two of them because of a poor detection quality. The values of average polar angles and total solid angles for this experiment for particular detector rings are presented in tab. A.3.

Table 4.1: *The geometry of crystal mosaics.*

parameter		"large" module	"small" module
distance from the center	R / mm	896	861
crystal diameter	d / mm	200	150
intercrystal distance	h / mm	178	135
intercrystal angle	β / deg	11.14	8.86
inner crystal solid angle	Ω_{in} / msr	32.06	19.60
outer crystal solid angle	Ω_{out} / msr	30.28	18.90
total solid angle in a lid	Ω_{tot} / msr	213.7	133.0

The nominal solid angle covered by CIS detectors amounts to 5.602 sr, i.e. 44.6% of the whole sphere, however it is reduced because of supporting grids (see Section 3.3). The Ni-mesh is not thick enough to stop all particle passing through the grid material, thus distorting the energy spectra and making the transparency energy- and particle-dependent. Gas volumes and foils in the flight path to scintillators also restrict the efficiency. The corresponding correction is described later.

4.4 Scintillator shell electronics

The complexity of the electronics associated with the large number of channels raises some difficulties related to their tuning, control and general management. Consequently, a number of additional demands need to be met by the design of CIS electronics and data acquisition, beside of usual requirements such as low noises and wide dynamic range: namely, a minimum number of connectors, a uniformity of signal processing, a fast read-out of fired channels, a software control of settings and the lowest possible cost per channel. A compromise has been found in the following way.

The block-scheme of CIS electronics is given in fig. 4.5. The corresponding signal structure is presented in fig. 4.6. Current signals from photomultipliers via 25 m 75Ω-cables are fed to the passive split-and-delay box consisting of 16-channel plates (crate 6U-type, Euromechanics), specially manufactured in the Research Center Rossendorf. For the purpose of the pulse-shape analysis the signals are split into "fast" and "slow" branches. The "fast" signals are delayed by 200 ns delay-line chips FLOETH PD24-20051D. The branches are directly connected with respective four CIAFB 96-channel current integrating analog-to-digital convertors (QDC). The CIAFB F683C [60, 79] is a single width FASTBUS module, using IAHJ0485 [80, 81] fast charge integration mini-plates providing 12-bit resolution for 15-bit dynamic range. (For missing QDC-channels the 8-channel CAEN QDCs in the CAMAC standard are used.)

The integration gates for the "fast" (400 ns) and "slow" (3 μs) signals are delivered by the REDUV gate-and-delay generator [82], supplied with a fast clear logic. High frequency (HF) from a cyclotron is fed through a discriminator to a NIM strobe generator. The HF-signal has a separate tunable delay line. Gates are opened by the first HF-signal coming after the TOF signal from the PSAC is accepted with the delay of about 100 ns.

An analog sum of signals from each of the 7 detectors, corresponding to one detector

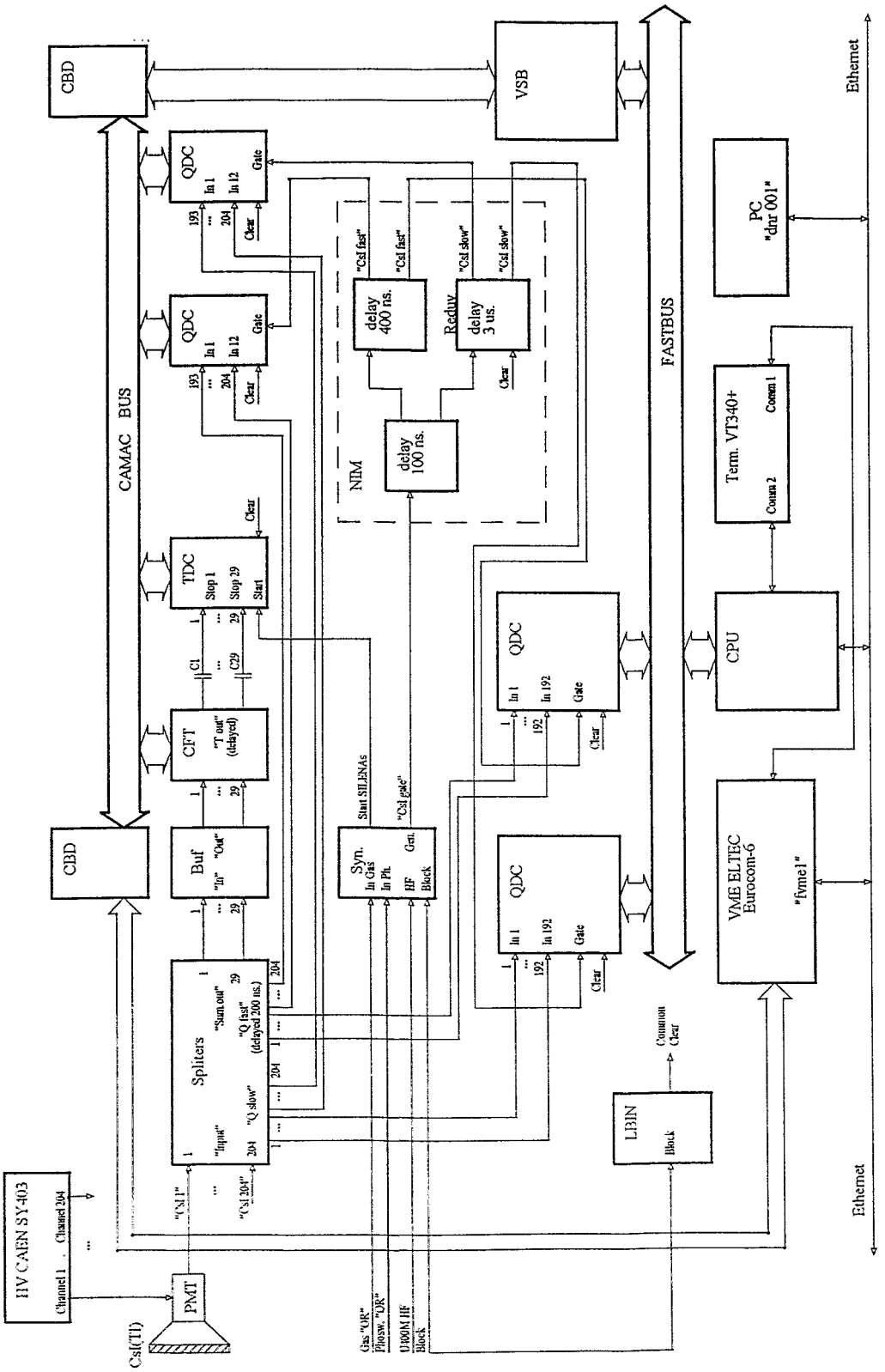

Figure 4.5: *The block-scheme of the CIS shell electronics.*

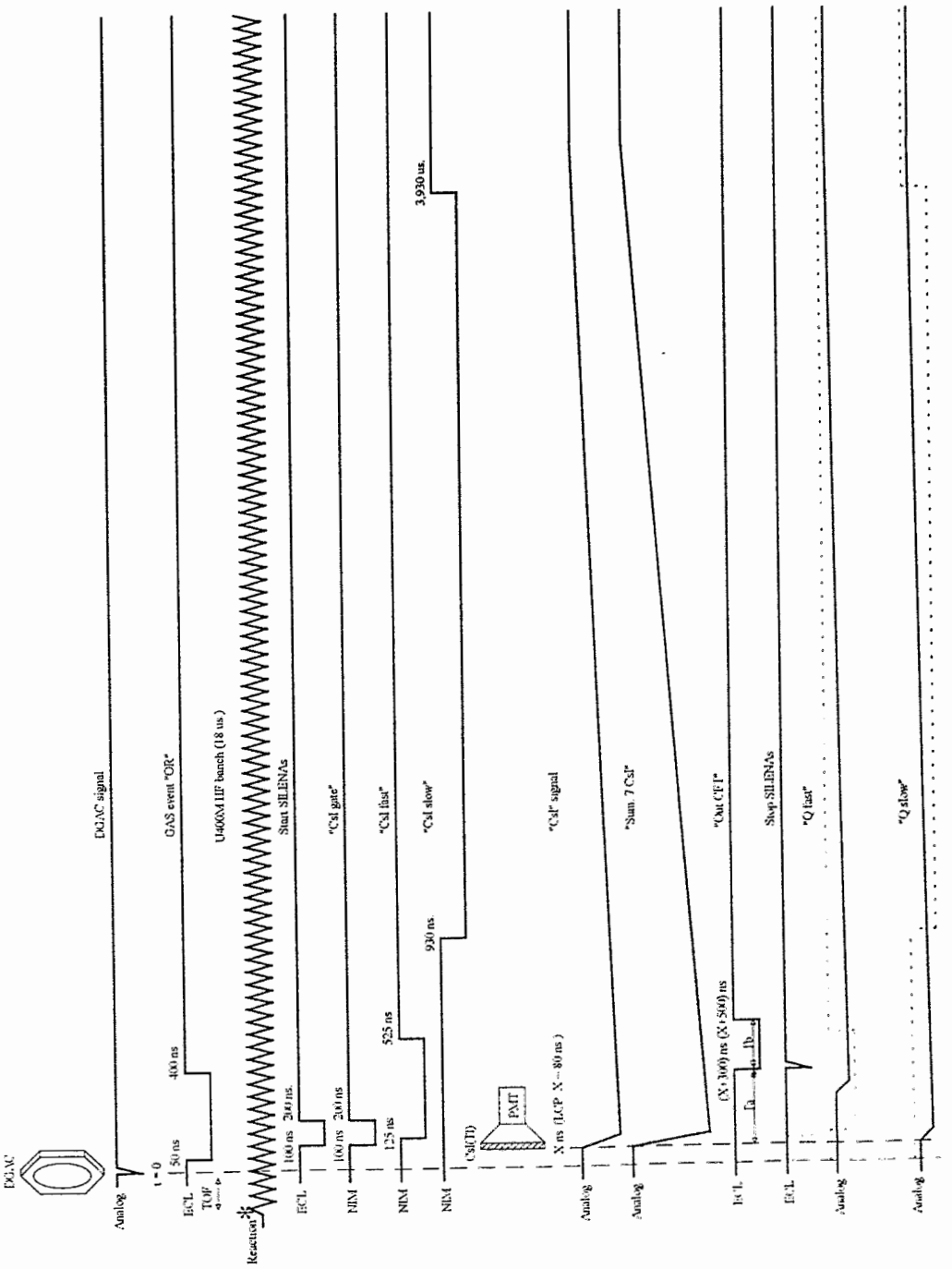

Figure 4.6: *Timing structure of CIS signals and the start from PSAC in the "CsI-slave" mode. DGAC (double-grid avalanche counter) means the same as PSAC.*

module, is fed via buffer to a discriminator. Four CF8101 8-channel blocks [83] with program-controlled thresholds serve as discriminators. A simple first-level trigger signal of the CIS shell ("CsI-fired") is derived from the discriminator outputs "OR" and fed into a gate-and-clear logic. The signal "CsI-fired" is sent into the central event selector and used as a "start" in "CsI-master" mode only. The ECL outputs of CF8101 are fed through a differentiating chain into corresponding four SILENA 8-channel timing ADCs [84]. These blocks provide time-of-flight signals of CIS detectors and also serve as pattern registers for CIAFB QDCs readout, one KOI-bit per a 7-crystal module.

Getting a LAM the EUROCOM-6 VME CPU after reading the front-ends of the gas detectors looks for CIS KOI bits. If a bit is set, the corresponding data portion (7 "fast" and 7 "slow" signals) from QDC blocks are transferred after conversion to a VME buffer. The conversion time amounts to about 1 ms for the 96 channels of the CIAFB QDC. Then all conversion results are scanned and those exceeding a given threshold value are added to the event data. If there is an event in gas detectors but not in the CIS shell or an event has been rejected by the fast trigger of the gas detectors, the "Fast Clear" signal prevents the conversion in the CIAFB thus shortening the dead time by 1 ms.

Because the multiplicity of fired CIS in one module not often exceeds one and timing signals of CIS are not used in data processing directly, one common timing signal (CT) per module seems to be a good compromise between TDC costs and data quality. If at least one CIS in a module has fired, it causes the read out of all QDCs in that module. The output of non-fired detector QDCs contains then a QDC-pedestal value, thus forming a sharp peak in spectra of parameters CF (L_{fast}) and CS (L_{slow}) in the raw data. A parameter CT and 7 pairs CF-CS correspond to one bit in the event pattern.

The high voltage power supply system is based on CAEN SY403 blocks [85] (64 independent channels per crate). They are filled with 16-channel A503 series plates providing a bias of up to 3000 V by 0.2 V steps and a current of up to 3 mA independently for each channel. The typical bias is around 1600 V. The values are chosen such as to fill the whole dynamical range of a QDC. The HV blocks can be controlled via coaxial 50Ω-cable with the CAMAC block C117B [86] utilizing the H.S.CAENET protocol (1 Mbaud).

4.5 Test of self-consistency and stability of data

The separate processing of the gas- and CIS shell data in the data acquisition system might lead by a number of reasons to a synchronization violation in the data flow. It means, that fission fragments, registered in the gas-modules for a certain reaction would be combined with light charged particles from either a preceding or a succeeding events. If this happens, it can significantly affect the physical results obtained. The strong correlation between physical observables such as linear momentum transfer (LMT) and LCP multiplicity, as it will be shown below, demonstrates, that such event mixing does not really happen in most of the events. However, it is necessary to look for the direct correlations between data from the gas- and the crystal-shell. It has been done also in the ^{14}N (34 AMeV)+^{197}Au experiment [87].

Indeed, most of particles with $Z \geq 2$ and also a fraction of Z=2 particles are tracked in PSAC, thus forcing a read out of BIC data. If particles have enough energy to punch through a BIC and are registered in a CIS, one can set-up a ΔE-E-telescope, utilizing the E signal from a BIC (E_{BIC}) as ΔE and the "fast" signal of a CIS detector (L_{fast}) as

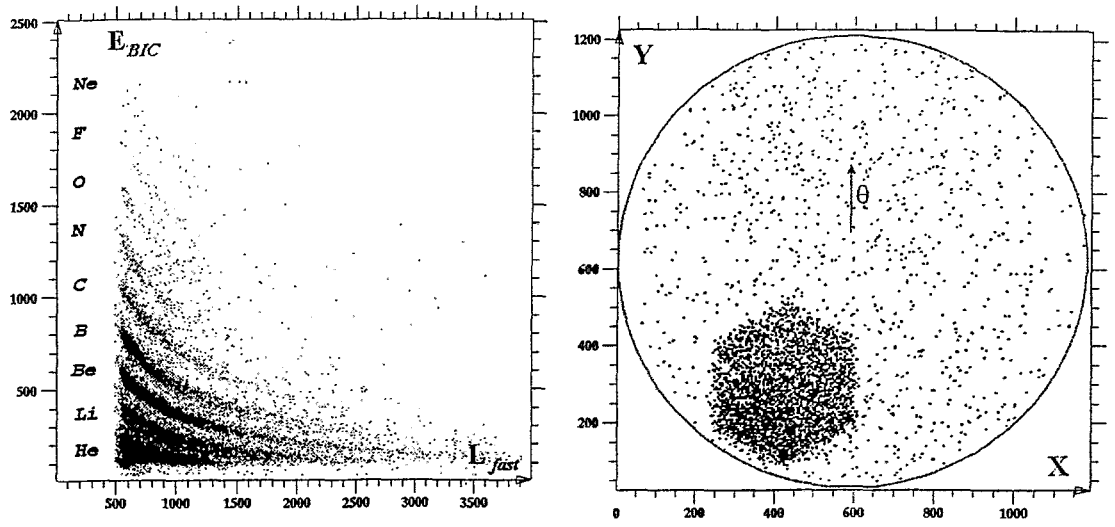

Figure 4.7: *Coincidences between gas detectors and CIS-data under the condition of $Z \geq 2$ in a CIS detector: the $\Delta E - E$ telescope (left panel) and the $X - Y$ PSAC matrix (right panel). The ring corresponds to the PSAC frame and the arrow shows the direction of growing θ. All the coordinates are given in channels.*

E. This check has been done on-line during the experiment. The observed matrix for the detector #015 is presented in fig. 4.7 (left panel). One can see separated particle lines up to Ne, also isotopes of ^{6}Li and ^{7}Li seem to be resolved. Such a nicely resolved structure has been observed also in a Z_{BIC} *vs* L_{fast} projection.

In order to get rid of most of the accidental coincidences and thus to get a clearer picture, only He and heavier particles registered in the scintillator have been selected by means of gates in corresponding particle identification matrices (PIM). In case of only piercing particles being selected in a E_{BIC} *vs* Z_{BIC} matrix, one can expect, because of the good angular resolution of a PSAC, a perfect projection of the hexagonal crystal shape onto the coordinate plane of a PSAC. This hexagon should be accompanied by some moderate number of dispersed counts mostly due to coincidences with slow alphas and fission fragments. Such a picture is presented in fig. 4.7 (right panel). One can see more counts concentrated in a lower part of the hexagon, because it corresponds to a smaller polar angle, thus reflecting an angular dependence.

The other source of errors in the data is an instability. If it is caused by a slow drift of parameters, and reasons for it are known (see below), it can be corrected by fixing of run-by-run averaged parameters at an overall mean level. Such a procedure is used to correct the time-of-flight in the gas part of FOBOS. This procedure cannot be applied to an individual CIS so easily, because the mean number of counts per detector in the scintillator part is approximately tree times lower, and, because LCP are mostly forward peaked, an order of magnitude worse in backward scintillators. Therefore the main problem is to distinguish short term deviations from a real parameter drift, especially in the automated processing mode.

A number of sources of instabilities during the experiment must be considered. Some of them can be excluded: namely, (i) the photomultiplier (PM) HV-supply is digitally stabilized, (ii) positions of QDC-pedestals are found to be the same for each run. However,

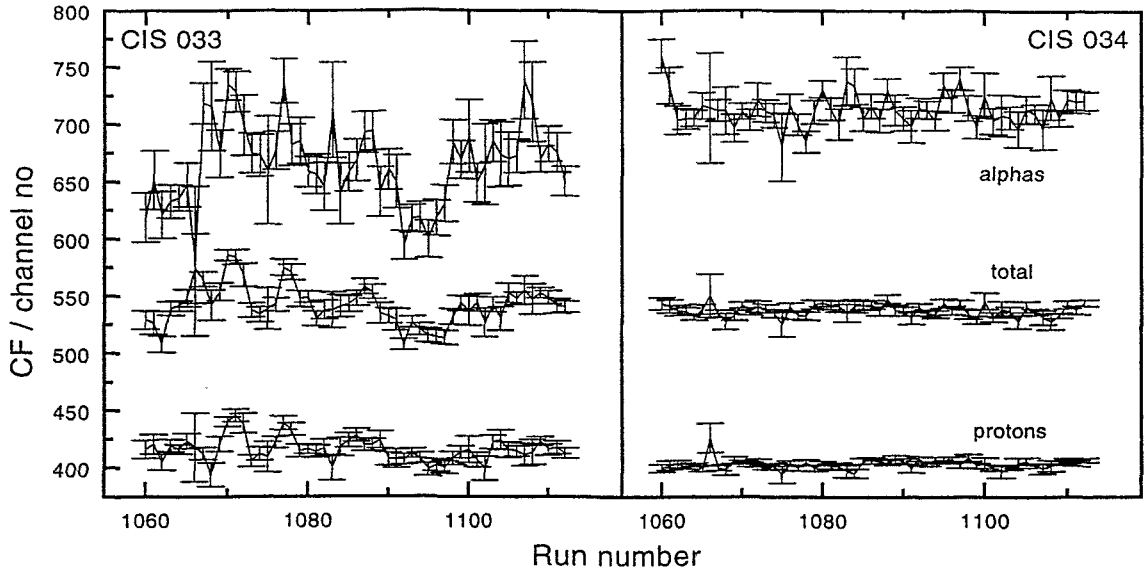

Figure 4.8: *The drift of the CF parameter for two CIS in the second part of the JAN96 experiment. The correlation between alpha and proton CF oscillations in CIS 033 is obvious. Data without particle identification are marked as "total". Oscillations in CIS 034 deserve no correction.*

light output from crystals, PM efficiency and electronic thresholds can drift. It is known, that a PM comes to the steady state of operation only after some days. A PM amplification can be affected by magnetic stray fields from beam line and cyclotron which depend on operation conditions due to insufficient shielding. The light output of CsI(Tl) in low radiation fields is mainly affected by the temperature. Bad contacts in a HV power supply, if any, can cause serious oscillations, and electronical noise is supposed to deteriorate mainly energy- and particle resolution.

In order to check the stability of the detectors' output during the experiment, some measured values are utilized. Average values for the parameters CF and CS, also with respect to different particle types, are analyzed as a function of the run number. The total number of counts per detector and the dispersion of parameters are also considered. An example of the oscillations of average values is given in fig. 4.8 (left frame). If there was a drift in parameters, caused by reasons mentioned above, the behaviour of average values <CF> and <CS> for protons and alphas should be strongly correlated. Moreover, in the case of a non-stochastical slow drift of parameters a correlation between neighboring runs should occur. In order to get a feeling of the correlations' level, one can look first at the correlation coefficients for a special case.

The correlation coefficient between two sets of values x_i and y_i is given by [1]

$$r = \frac{\sum_{i=1}^{n}[\omega_{x_i}(x_i - \bar{x})][\omega_{y_i}(y_i - \bar{y})]}{\sqrt{\sum_{i=1}^{n}[\omega_{x_i}(x_i - \bar{x})]^2 \sum_{i=1}^{n}[\omega_{y_i}(y_i - \bar{y})]^2}}, \tag{4.1}$$

where $\bar{x}$ and $\bar{y}$ are average values of x_i and y_i. Setting, for example, $y_i = x_{i-1}$, one obtains the self-correlation value.

[1] modified from that of [88], where statistical weights are not included

The statistical weights ω_{p_i} are normalized to unity by means of the equation $\sum_{i=1}^{n} \omega_{p_i} = 1$, where p denotes either x or y. The weight of the value p_i is proportional to the number of measured counts N_i from which p_i is determined. Then

$$\omega_{p_i} = \frac{\Delta p_i^{-2}}{\sum_{i=1}^{n} \Delta p_i^{-2}}, \tag{4.2}$$

where $\Delta p_i = \sigma_{p_i}/\sqrt{N_i}$ and σ_{p_i} is the dispersion of p_i.

For a large number of probes n (according to ref. [88] for $\omega_{p_i} = 1$) the values x_i and y_i are correlated (or anticorrelated) at the confidence level of $1-\alpha$ if the following inequality is fulfilled:

$$z_\alpha < \sqrt{n}\frac{|r|}{1-r^2}, \tag{4.3}$$

where r is the correlation coefficient given by eq. 4.1, and z_α corresponds to the confidence level 1-α in terms of the Error-function:

$$1 - \alpha = 2\Phi_0(z_\alpha) \tag{4.4}$$

The inequality 4.3 is true for any $r \in [-1;1]$ if $|r| > r_n$, where r_n is the critical correlation coefficient defined by this inequality. Some values of r_n are given in table 4.2.

The typical analyzed chain of runs is of a length about n=50. The reasonable critical value of $r_n \approx 0.25$ is deduced from the data analysis. Experimental values of the correlation coefficients are given in Table 4.3 for the detectors shown as an example in fig. 4.8. A visible difference in the data is reflected in the coefficients. The obvious correlation of the <CF> parameter for alpha and protons in CIS 033 results in large coefficients r for the detector 033. Large self-correlation values correspond to visible macro-drifts of the parameter <CF>. On the contrary, correlation and self-correlation coefficients for CIS 034 are smaller than 0.25, indicating less correlation. Coefficients calculated with statistical weights reveal obviously larger values than those without weights, because weighted coefficients are less sensitive to stochastical noises. The correlations between <CF> for protons and alphas on the one hand side and the total data (e.g. without particle-separation) on the other hand side are rather strong. A low correlation level of even the anticorrelation would indicate problems with particle separation, because the proton- and alpha-data are major components of the total data.

The correlation analysis revealed 26 detectors in the forward hemisphere, where some instability occurs. In general, the stability of the data seems to be rather good (see the last line in Table 4.3), however some problems still remain. The application of the correlation analysis in the backward hemisphere is questionable because of the low statistical

Table 4.2: *Values of the critical correlation coefficient r_n, calculated for the n=25-200 probe points. The (anti)correlation occurs with the probability of $1-\alpha$ if $|r| > r_n$.*

$1-\alpha$	z_α	r_{25}	r_{50}	r_{100}	r_{200}
0.50	0.665	0.13	0.09	0.07	0.05
0.90	1.645	0.30	0.22	0.16	0.11
0.95	1.96	0.35	0.26	0.19	0.14
0.99	2.58	0.42	0.33	0.24	0.18

Table 4.3: *Values of the experimental correlation coefficient r, calculated for CF signal from detectors presented in fig. 4.8. The index w means, that weights are used, "all" denotes no particle type selected, "self" correspond to self-correlation in the given particle data. The last line represents mean values over 82 selected detectors in the forward hemisphere (FH), the standard error is* ≈ 0.02 *for each coefficient.*

CIS	r^w_{p-He}	r_{p-He}	$r^w_{p-total}$	$r^w_{He-total}$	$r^w_{p,self}$	$r_{p,self}$	$r^w_{He,self}$	$r^w_{total,self}$
033	0.70	0.38	0.86	0.88	0.56	0.47	0.63	0.57
034	0.14	0.05	0.27	0.73	0.14	-0.03	0.08	0.02
Mean (FH)	0.21	0.12	0.51	0.54	0.17	0.09	0.27	0.30

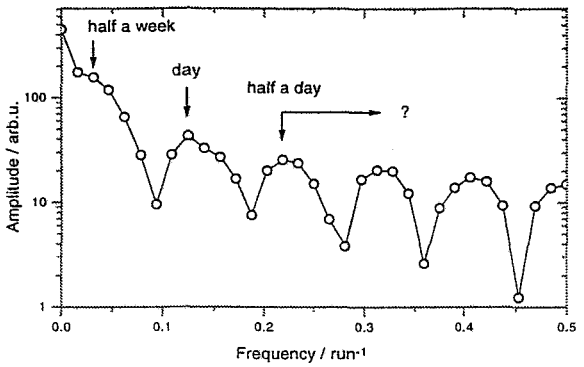

Figure 4.9: *The Fourier-frequency spectrum for CIS 017. Half-a-week and daily peaks are recognizable, other peaks are not reliable. See text for detailes.*

accuracy. The origin of instability is not clear, however, the correlation analysis is useful in checking different hypotheses. For instance, the possibility of the QDC-amplification drift is excluded by considering the correlation coefficients between <CF> and <CS>. They are found at the level of $\approx$0.96. Such a high correlation level is not possible in the case of a drift in the individual channel, because "fast" and "slow" signals are processed even in different QDC plates.

In order to understand the origin of the parameters' drift it was tried to perform a Fourier-frequency analysis (FFA) of the average-value oscillations like in ref. [89]. It is rather difficult to calculate frequencies precisely, because there is no real time parameter in the data, however one can assume a rough time scale of $\approx$3 hours/run. Some results, for example, for CIS 017, are shown in fig. 4.9. One cannot rely on sub-daily frequencies, but the existence of half-weekly period and daily period seem to be obvious. Similar results are obtained for all analyzed detectors. Subtracting a linear trend or simply a constant fraction before FFA, one can locate these peaks even better, but only the analysis based on a real time parameter would provide reliable results.

The half-week period can be compared with that from ref. [89], but it originates more probably from the limited observation time. The daily period can be attributed to a number of reasons, first of all to the day-night temperature difference and also to an often observed day-night difference in the beam quality. The latter is, of course, incorrectable.

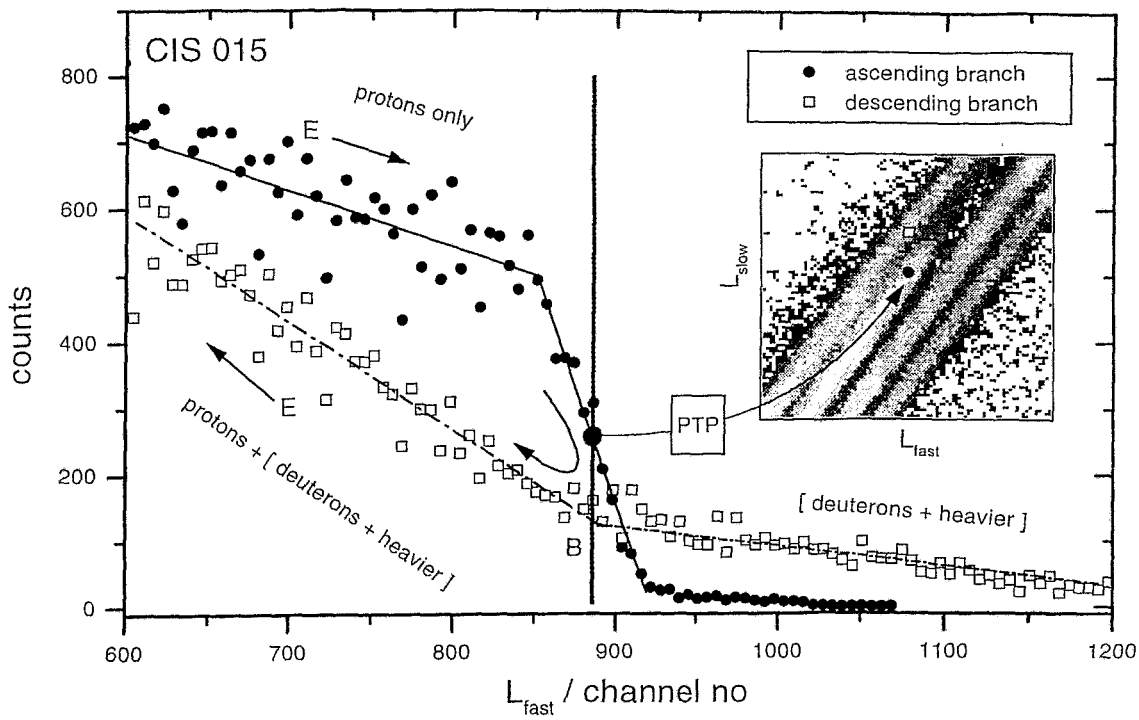

Figure 4.10: *The position of the punch-through point (PTP) at the end of the ascending proton branch (solid circles) and its position in the CF vs CS scatterplot (PIM). The PTP position corresponds to the salient point of the descending proton branch (open squares). Lines mean a linear fit in their regions between salient points.*

The second half of the experiment JAN96[2] generally satisfy the beam and detector operation stability requirements. The CIS data from the second half of the experiment reveal the better particle resolution. During the first half of the experiment there were changes in tuning of some detectors, what introduces an additional complexity of a data processing. Due to these reasons the data from only the second half are used in this thesis.

4.6 The scintillator shell data processing

The first step the data processing consists in sorting out the data accumulated in each module separately (single-files). A CIS single file consist of the values of signals CT, CF, CSi (i=1..7); the values of the coincident signals from gas detectors CTOF (PSAC TOF), CX and CY (PSAC coordinates), CE and CZ (BIC E_R and BP) can be also added.

The typical space occupied by the raw data from one experiment amounts to some tens of gigabytes. In order to save processing time and to reduce the amount of storage media needed the bulk of data is reduced by means of validation gates in raw parameter distributions. CIS data are reduced by cutting off pedestals. The latter reduces the data volume at least to 1/4 of the initial volume. The position of pedestal peak is used as zero in the CIS energy calibration.

[2]according the internal designation: 1st half — NTHA and NAU; 2nd half — NTHB and NAU2

The punch-through points (PTP), needed for the calibration, are defined in the middle of the steep spectrum slope at the end of the ascending particle branch (fig. 4.10). The choice of the point is based on the idea, that a thick scintillator can be imagined as a sandwich of two thin crystals. The corresponding continuous spectrum of the thick crystal should be a sum of symmetrical spectra of the thin crystals. The punch-through point for one thin crystal should be at the same time the "punch-in" point for another one. This PTP position corresponds also to the salient point on the descending particle branch.

The energy calibration is described in Chapter 5. The particle energy at the target position is reconstructed taking into account all penetrated media on a particle fight path. Every individual PIM is scaled by means of a linear transformation to an "ideal" PIM, for which the geometry of particle branches and inter-branch separators are calculated (see Appendix, tab. B.2). Using these data one gets automatically a particle type together with the energy calibration. This saves a lot of time as compared to manually set particle identification gates in each individual PIM. Because particle separators are defined as some non-intersecting functions, particle lines for H isotopes are additionally cut-off near a PTP position. The other way to separate particles without gates might be to use some particle identification functions, like in ref. [90].

The above procedures are applicable to event-by-event processing. There are some reasons leading to a distortion of the shape of spectra. A thin supporting grid of 50 μm Ni on the flight path affects one forth of all particles. The same happens because of coordinate wires in PSACs. This leads besides energy loss to an additional reduction of transparency. The registration efficiency itself depends on the velocity of the emitting source as well. Corrections of these factors cannot be done event-by-event. Although the precise correction is impossible, two rough procedures can be applied.

The correction procedure in the case of an etched Ni-mesh is the following. The affected energy spectrum is split first into small energy steps. The distribution of counts among split channels plays no role — the smooth interpolation instead of uniform distribution results only in some small corrections (fig. 4.11, left panel). The total number of counts in the spectrum remains, of course, the same. In order to get a reasonable statistical accuracy experimental LCP spectra are accumulated into 2 MeV energy bins. A reasonable steps for split spectra are found to be 0.2 MeV .

The split spectrum is treated in the following way. The channel number H with the highest energy E_H is treated as containing N_H only non-affected particles (with the probability 3/4). Because of the 3/4 mesh transparency the number $\Delta N = N_H/3$ should be added to N_H, at the same time ΔN is subtracted from the channel number L corresponding to the energy $E_L = E_H - \Delta E(E_H)$, where $\Delta E(E_H)$ is the energy loss in 50 μm Ni. Then the same step is performed with the channel number $H - 1$ and so on, down to the lowest energy. Afterwards the spectrum of redistributed counts is summed with the energy steps of the initial spectrum of 2 MeV. Such a simple procedure is able to reconstruct an affected spectrum. An example is given in the fig. 4.11 (right panel).

The next step aimed at a correction of the shape of a spectra modified due to particle emission from a moving source. Spectra analyzed below are assumed to originate from the compound nucleus. The registration efficiency then can be simulated using the experimentally measured source velocity distributions, restored from the fission fragment kinematics.

The registration efficiencies are explored by means of an event-by-event simulation. A source with the given velocity v_z (the component parallel to the beam axis) emits, in its

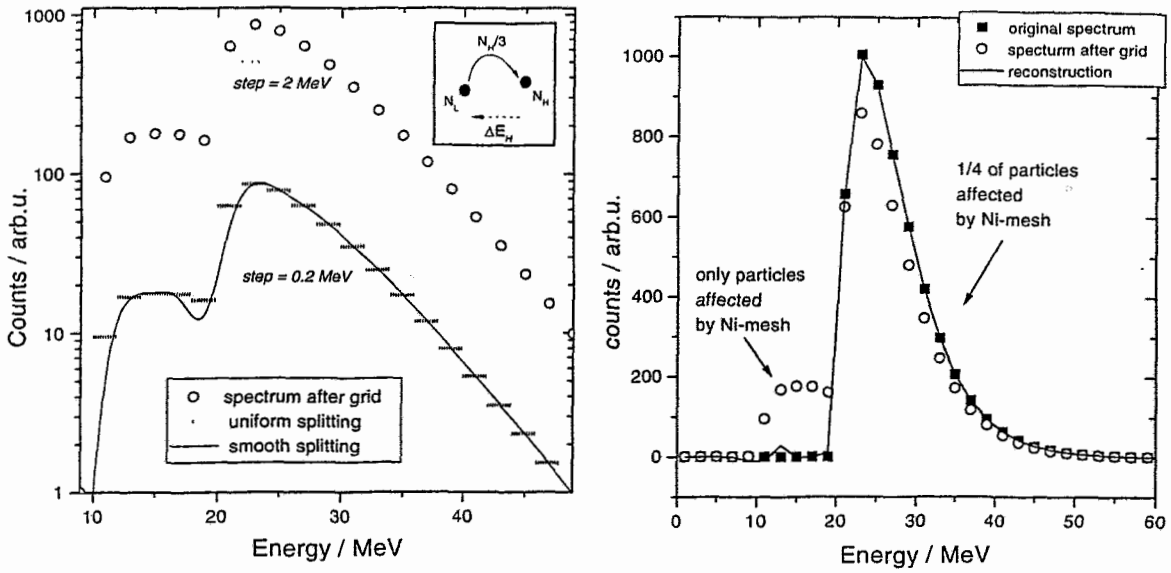

Figure 4.11: *Left panel: Splitting of the spectrum into small steps with the uniform and smooth distribution. The cut-in illustrates the method idea (see text). The model α-particle spectrum (squares) have been passed through 50 μm Ni-mesh with 75% transparency. Right panel: The affected spectrum (circles) has then been reconstructed (line). The agreement of initial and reconstructed spectra is very good, at least for a smooth spectrum.*

rest frame, particles into the whole sphere isotropically and with a uniform energy distribution. Orthogonal components of the source velocity are gaussian-like distributed. The distribution widths w_x and w_y depend on v_z because the contribution of the momentum removal by LCP grows with LMT. Experimentally measured $w_x = w_y$ are represented for convenience by a linear approximation (fig. 4.12).

The velocity of a particle in the laboratory frame is calculated as the vector sum of the particle's c.m. velocity and the source velocity. The energy spectra are accumulated if the particle hits the detector and produces a signal above threshold. The normalization of the resulting spectra to the initial one immediately gives the efficiency. An example of simulated spectra is given in fig. 4.13.

The quantitative results obtained from particle spectra which will be discussed later in chapter 6 are obtained after all necessary corrections, they will not be mentioned further.

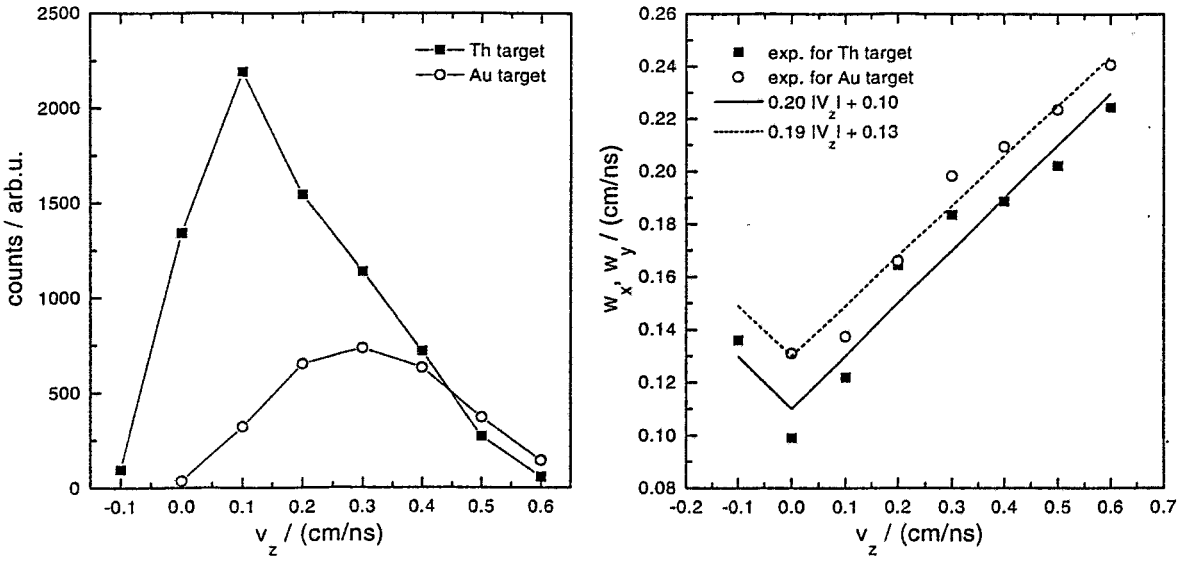

Figure 4.12: *Left panel: Distributions of emitter (c.m.) velocities v_z parallel to the beam axis. Right panel: The width of a gaussian distribution w of emitter velocities perpendicular to the beam axis. The dependence on $|v_z|$ is assumed for interpolation purposes to be a linear function.*

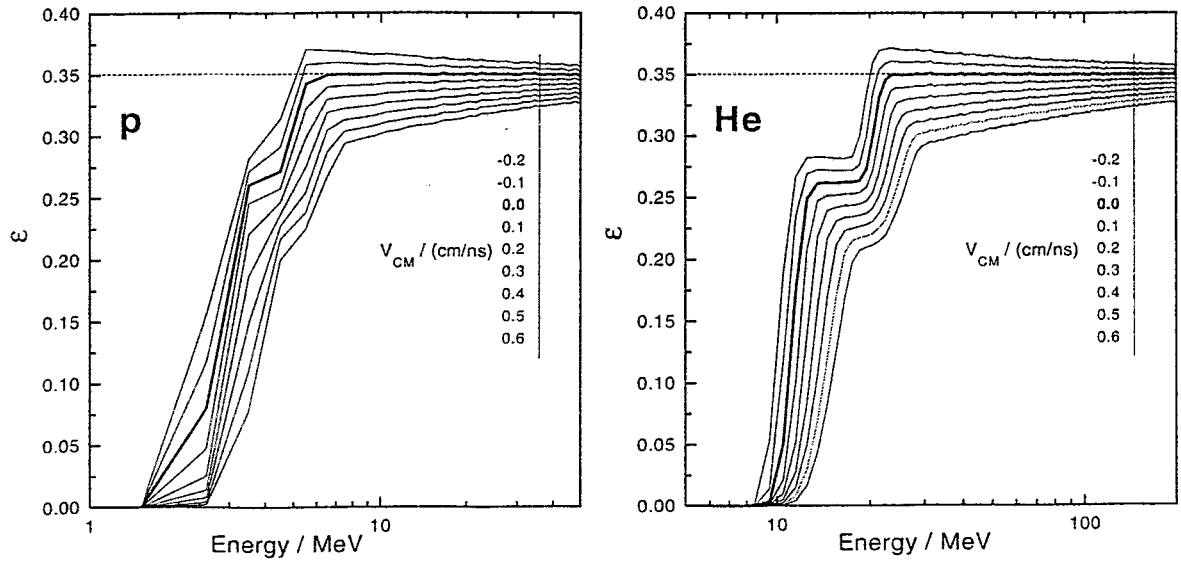

Figure 4.13: *The registration efficiency for protons (left) and α-particles (right) emitted into 4π sr calculated for the azimuthal angle region $\vartheta = 100 - 150°$. Each line corresponds to one emitter velocity in the listed order. The bold line corresponds to a resting emitter. The solid angle covered amounted to $0.35 \times 4\pi$ sr.*

Chapter 5

Calibration of the scintillator detectors of FOBOS

5.1 Calibration problem[1]

The energy calibration of a scintillator response is commonly based on the measurement of the total light output; the dependence on the shaping time has also to be considered [92]. Often a few calibration points are obtained by a direct exposition of the detector to radioactive sources or ion beams, exploiting then an additional ΔE or TOF information for further analyses. The energy calibration is then obtained by fitting the data with sophisticated empirical functions for the light output $L(E)$ [93, 94] or $E(L)$ [95]. Such functions can also be the result of analytical calculations based on models for both the energy deposition along the ion track in the scintillator and the luminescence process [96].

The light output of CsI(Tl) manifests a strong dependence on the energy (E) of the incoming particles and also on their atomic (Z) and mass number (A). Furthermore, the scintillation-light pulse-shape is a complicated function of the stopping power dE/dx (cf. ref. [75] and refs. therein). Hence, much attention has already been paid to the problem of detector calibration. There are some common features in the scintillation light processing in spite of the different operation modes of the CsI(Tl) crystals (e.g. utilizing them in the usual regime or in a phoswich combination with other scintillators [95, 97, 98], in ΔE(Si)-E(CsI) telescopes [75, 99], the TOF-E(CsI) analysis [100, 78], also applying photodiode read-out [101, 102, 90] etc.). In particular, the pulse-shape analysis (PSA) method [75, 74] is used to search for the best particle separation and energy resolution for light charged particles (LCP) in a wide dynamical range (Appendix, fig. B.1).

The aim of the present work is to perform an energy calibration of the CsI(Tl) scintillators (CIS) used in the outer shell of FOBOS [73] for the LCP spectra recorded in the absence of specially measured reference points. The only available information is given by the punch-through points (PTP) of different LCPs, and the corresponding energy values are the largest energies which can be deposited in the crystal by these particles. Moreover, the variant of PSA used at FOBOS for LCP separation does not deliver the total light output, i.e. the total integral of the light pulse, but only two partial ones. We, therefore, applied a rather simple model for the simulation of the CsI(Tl) light pulse in dependence on the type of the incoming ion (Z, A) and its energy E and, further, simulated the par-

[1]This chapter has been published by the author in the "Nuclear Instruments and Methods..." [91]

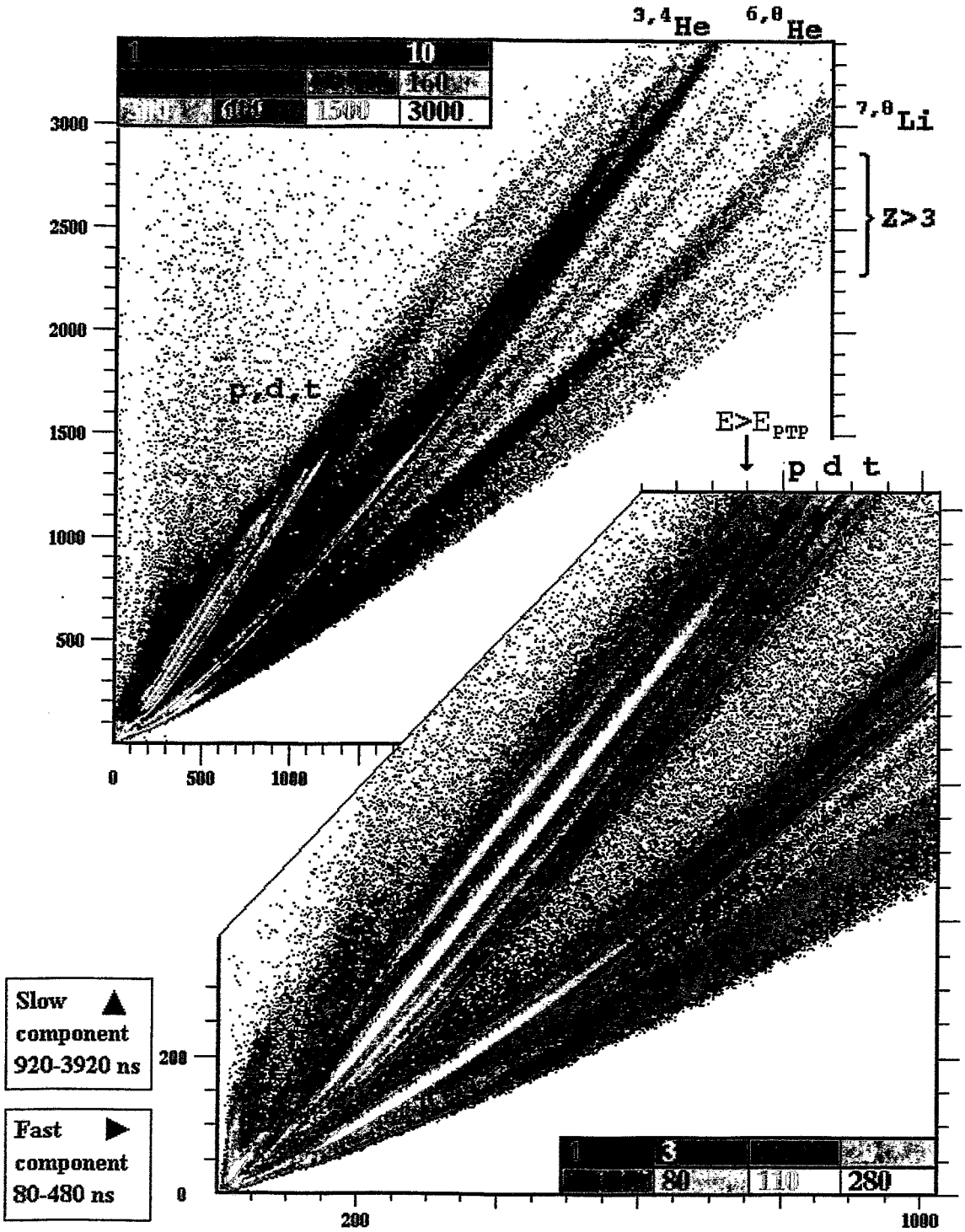

Figure 5.1: *Summed particle identification matrix (PIM) for the CsI(Tl) detectors positioned at ϑ_{lab} = 28° to 47° ($\Delta\Omega$ = 0.4 sr). This PIM represents 40% of the entire data body recorded for the reaction ^{14}N (53 AMeV) + ^{232}Th. The energy scale extends to ≈300 MeV.*

ticle identification matrix (PIM) as it follows from the application of the PSA method under real experimental conditions. These matrixes reveal very useful scaling properties for the calibration procedure of the altogether 210 CsI(Tl) detectors of FOBOS (fig. 5.1). In the following, the calibration method is described in detail. A first attempt to apply such a method has been published earlier [103].

5.2 Calibration method

Under the assumption that all CsI(Tl) crystals of the scintillator shell have similar properties (that was guaranteed by the manufacturer), that all photomultipliers are operated in a linear regime, and that all signals are processed in an equial manner, one expects that all PIMs look similar, and one can sum them up into one PIM after some linear transformation accounting for different gains. Therefore, we scaled the individual PIMs to each other by use of the point E=0 (pedestal position) and PTP. The summed PIM is shown in fig. 5.1. Indeed, resolved particle branches occur for the H and He isotopes, also for ^{6}He and ^{8}He. Furthermore, branches of heavier particles are clearly seen. Usually, these branches are very weak in the PIMs of the individual detectors due to low statistics. Note that the scaling procedure does not lead to a loss of resolution for the particle identification.

The largest energies of H, He and Li isotopes which can be deposited in the CsI(Tl) crystals by were calculated using the stopping power code STOPPOW [104], and are given in Table 5.1. Particles with these energies manifest themselves in PTP. Particles with higher energies are not stopped in the crystals. They pierce them, and the deposited energy becomes successively lower with increasing incident energy. Hence, the particle branches, after reaching the PTPs, turn backward (descending branch, fig. 4.1) approaching the branch of low-ionizing particles (electrons, γ-rays). The PTPs are well pronounced in the PIMs of forward-positioned detectors.

The CsI(Tl) crystals are manufactured with precision of 0.1 mm. Therefore, the PTPs can be treated as intrinsic energy reference points suitable for calibration purposes. The

Table 5.1: *Maximum energy losses of light ions in the CsI(Tl) crystals of the scintillator shell of FOBOS (PTPs).*

Particle	*AMeV*		*MeV*	
	10 *mm*	15 *mm*	10 *mm*	15 *mm*
p	51.0	64.5	51.0	64.5
d	34.2	43.2	68.3	86.4
t	27.0	34.2	80.9	102.5
^3He	60.3	76.1	180.8	228.4
^4He	51.1	64.5	204.2	258.0
^6He	40.4	51.1	242.3	306.3
^8He	34.2	43.2	273.4	345.8
^6Li	64.6	81.5	387.3	489.1
^7Li	59.1	74.6	413.4	522.1

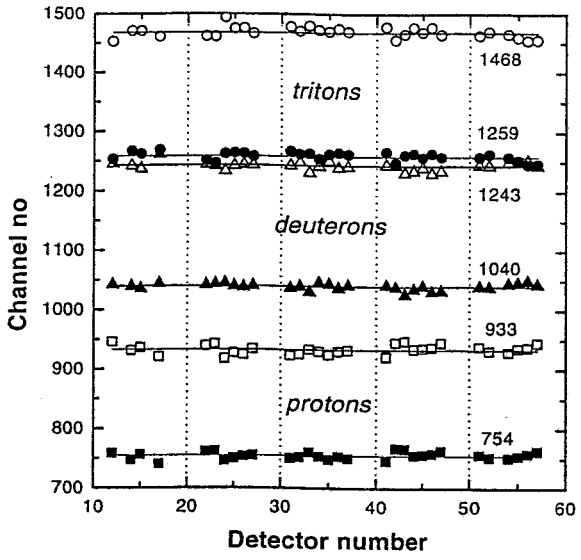

Figure 5.2: *Coordinates of punch-through points in individual CsI(Tl) detectors after application of the scaling procedure. Solid symbols denote the coordinates L_{fast}, open symbols denote the coordinates L_{slow}.*

clear indication that PTPs are really reliable is given in fig. 5.2. The relative error of the determination of the PTP-coordinates from PIMs of individual detectors is typically of about 2%. The scaling procedure, therefore, is based on PIMs with well pronounced PTPs. It brings the particle branches, and naturally also the PTPs, of all CsI(Tl) detectors to superposition.

The PTPs are weakly pronounced or absent at all in the detectors positioned in the backward hemisphere of FOBOS. To add these PIMs to the summed PIM too, we applied the following method. We first constructed an "ideal" PIM (Appendix, table B.2) out of such individual PIMs, where a good particle resolution is observed and the PTPs (mainly those of the H isotopes) are clearly pronounced as well. A special procedure was also developed utilizing the *shapes* of the particle branches in the PIMs for scaling purpose. It is based on the simulation of the PIM as it follows from the application of the PSA method. Simultaneously, relative energy scales for the individual particle branches are generated. The normalization of the simulated PIM at the PTPs then delivers the absolute energy scales. By a suitable variation of the energy- and particle-dependent parameters being model ingredients of the scintillation light pulse-shape, the experimentally observed *shapes* of the particle branches in the PIM can easily be generated. The obtained relative energy scales can then be used for the scaling of the PIMs without PTPs for adding them to the "ideal" PIM. In the following, this method is described in detail.

5.3 Simulation of the particle identification matrix

The simulation of the PIM as it follows from the PSA method used is based on the approximation of the CsI(Tl) scintillation light pulse-shape L(t) (eq. 5.1) by three exponential functions with the characteristic time constants τ_i; a few hundreds of nanoseconds for

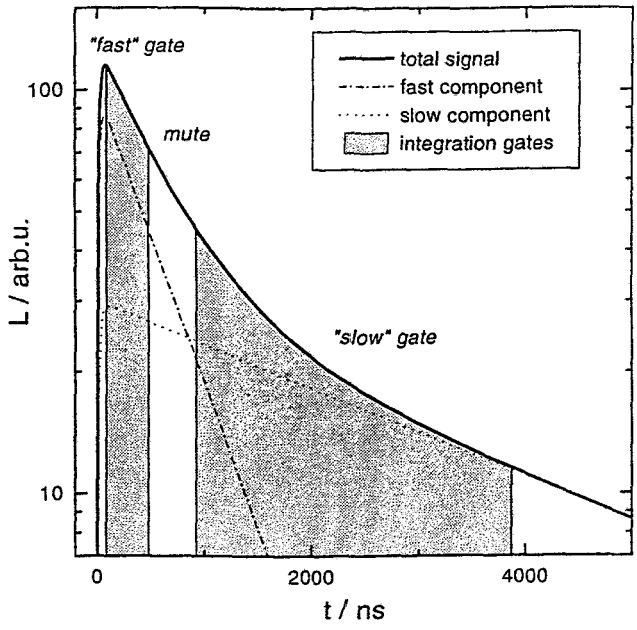

Figure 5.3: *Calculated shape of a scintillation light pulse of CsI(Tl), constructed by superposition of the fast and slow components of an α-particle of 50 MeV energy. The time gates are shown as they were set in the experiment.*

the "fast" light component (τ_{fast}), a few thousands of nanoseconds for the "slow" light component (τ_{slow}), and 10 to 100 ns to take into account the pulse rise-time (τ_{front}).

$$L(t) = \frac{h_{slow}}{\tau_{slow}} exp(-\frac{t}{\tau_{slow}}) + \frac{h_{fast}}{\tau_{fast}} exp(-\frac{t}{\tau_{fast}}) - \frac{h_{front}}{\tau_{front}} exp(-\frac{t}{\tau_{front}}). \tag{5.1}$$

h_{fast} and h_{slow} denote the magnitudes of the two light components. Coordinates of the PIM are the integrals L_{fast} and L_{slow} of $L(t)$ taken for the hardware-set time gates Δt_i. The values of $\Delta t_{fast} = [80, 480]$ ns and $\Delta t_{slow} = [920, 3920]$ ns are used in the experiment (fig. 5.3). The time constant τ_{slow} is known to be nearly particle-independent and to take values in the range of 4 to 7 μs. The ratio $R = h_{slow}/h_{fast}$ as well as the decay time constant of the fast component τ_{fast} are decreasing functions of the stopping power dE/dx ([75] and refs. therein). The function τ_{fast} shows some saturation effect near a stopping power of 1000 MeV/cm [105].

The properties of CsI(Tl) crystals strongly depend on their quality and Tl concentration. To obtain analytic expressions for the dependence of R and τ_{fast} on E and the type of particle (Z, A), the appropriate empirical functions $R(E, Z, A)$ and $\tau_{fast}(E, Z, A)$ are fitted to the experimental data from ref. [75]. The dependence on the type of particle is given in terms of the quenching parameter $q = AZ^2$. To limit the number of fitting parameters, the following expressions were found to be suited:

$$R(E, q) = \frac{R_0}{q^{1/4}}[1 - exp(-\frac{d}{q^{1/4}} E^Q)], \tag{5.2}$$

$$\tau_{fast}(E, q) = \tau_0 + \frac{\tau_1}{q^{0.1834}}[1 - exp(-\frac{d}{q^{1/4}} E^Q)], \tag{5.3}$$

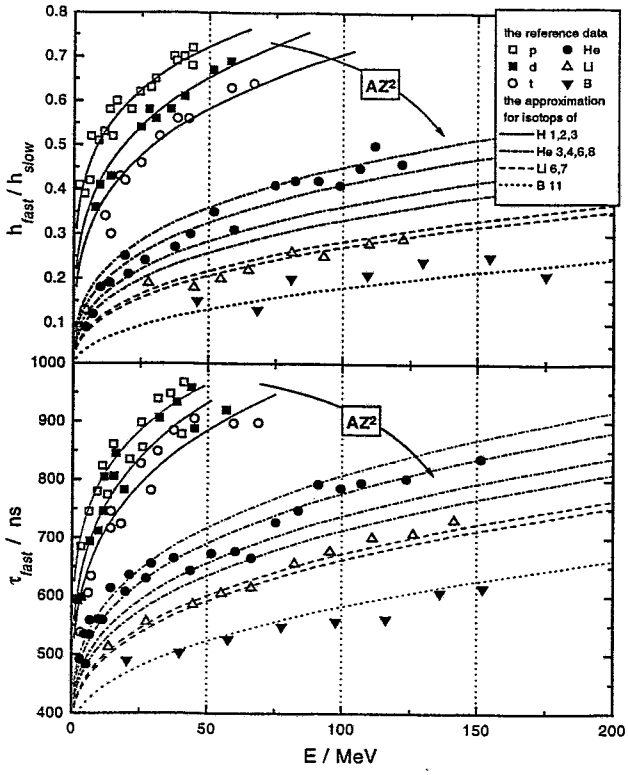

Figure 5.4: *Comparison of CsI(Tl) data of ref. [75] (symbols) with our approximations (lines) based on a quenching parameter systematics. The arrows show the rise of the decay time of the fast light component (upper panel) and of the ratio between the magnitudes of the slow and fast light components (lower panel) with AZ^2 as a function of the energy of an incident particle.*

where the fitting parameters assumed values of $\tau_0 = 365$ ns, $\tau_1 = 3323$ ns, $R_0 = 4$, and $d = 0.081$. The parameter Q was found to be slightly dependent on q. An analytic expression for extrapolation purposes was found in the form of

$$Q(q) = 0.285[1 - exp(-\frac{q}{0.611})]q^{0.102}. \tag{5.4}$$

The functions $R(E,q)$ and $\tau_{fast}(E,q)$ may not represent the best fit for each particle type individually, but they describe the general trend sufficiently well (fig. 5.4).

If the ratio of the light components R is given, the absolute values for h_{fast} and h_{slow} can be derived from the normalization of the total integral of $L(t)$ to the total light output $L(E)$

$$\int_0^\infty L(t,E,Z,A)dt = h_{slow} + h_{fast} - h_{front}. \tag{5.5}$$

The latter is set equal to the expression given in ref. [93],

$$L(E) = S[E - a(Z,A)ln(\frac{E}{a(Z,A)} + 1)], \tag{5.6}$$

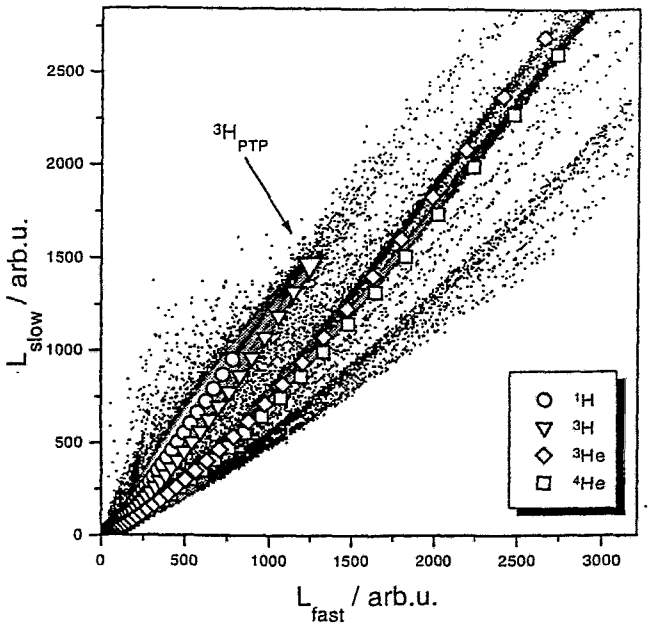

Figure 5.5: *The real particle identification matrix L_{slow} vs L_{fast} of a CsI(Tl) detector is compared with the simulated one. They are scaled to each other using punch through point for ^3H, marked as an enlarged symbol. Deviations of simulated lines from real ones don't exceed few percent even no fit is performed.*

where E is the energy deposited in the CsI(Tl) crystal, $a(Z, A)$ is the quenching constant, and S is the scintillation efficiency. By the condition $L_{t=0} = 0$ the value of h_{front} is connected with R as well as with the time constants and thus can be easily estimated.

Performing the simulation of the PIM for given types of particles, intervals of incident energy and time gates (Δt_{fast},Δt_{slow}), we simultaneously get the relative calibration curves $L_{fast}(E)$ and $L_{slow}(E)$ for every particle branch. The simulated PIM is shown in fig. 5.5, calculations for different time gates are given in Appendix, fig. B.1.

The normalization of the simulated PIM to the "ideal" PIM with reference to the positions of the PTPs delivers the particle-dependent absolute energy scale. The *shapes* of the particle branches in the simulated PIM can principally be modified to approach the experimentally observed ones by slight variations of the parameters of eqs. 5.2 and 5.3, accounting in this manner for the properties of the CsI(Tl) crystals used.

Since $\Delta t_{fast} < \Delta t_{slow}$, the contribution of noise in the measured values of L_{fast} is significantly less than in L_{slow}. On the other hand, L_{slow} is less sensitive to small energies. We used $L_{fast}(E)$ for the calibration of the spectra of LCPs within the entire dynamic range. The calibration curves for both light components with respect to the time gates used are shown in fig. 5.6.

The energy losses of the particles on the flight path from the target to the CsI(Tl) crystals in the penetrated detector materials (i.e. the PSAC foils, the windows and the gas volume of the BIC, the Mylar reflector foil) were calculated using the code STOPPOW [104]. The dead layer at the surface of the CsI(Tl) crystal [106] is very thin and was neglected. A useful empirical expression for the correction of the energy losses has been

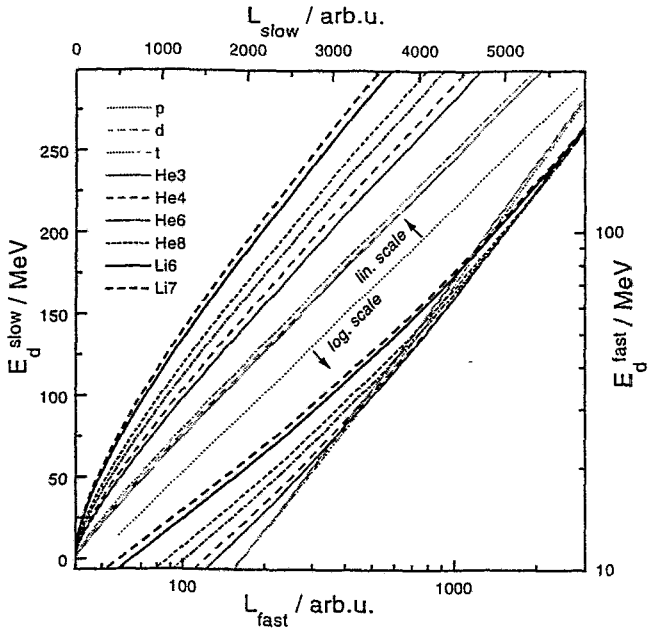

Figure 5.6: *Simulated calibration curves for the slow (upper left corner) and fast (lower right corner) PSA components recorded for time gates* $\Delta t_{fast} = 80$ *to 480 ns and* $\Delta t_{slow} = 920$ *to 3920 ns, respectively. For better visuality, the fast component is plotted in a logarithmic scale.*

deduced (fig. 5.7),

$$E_t = [(E_d + E_0)^\alpha + C^\alpha]^{1/\alpha} - E_0, \tag{5.7}$$

where E_t and E_d are the energies of the particles at the target and in the CsI(Tl) crystal, respectively, and E_0, C and α are fitting parameters (Appendix, table B.1). The approximated function $E_d(L_{fast})$ can be written in the form

$$f(x) = ax^b + \frac{c_1 x}{d_1 + x} + \frac{c_2 x}{d_2 + x}. \tag{5.8}$$

The fit coefficients a, b, c_1, d_1, c_2, d_2 calculated for the simulated dependence $L_{fast}(E)$ are given in the Appendix, table B.2.

5.4 Shape-scaling method

As already mentioned above, PTPs are not available in some cases. There are mainly two reasons for this. First, the energies of the particles emitted into the backward hemisphere (in the lab-system) are lower due to kinematics. Secondly, a significant error in the PTP determination occurs due to low counting rates in backward-oriented crystals. If the PIM is not distorted by other influences, it can be scaled to the "ideal" one by use of the *shapes* of the particle branches. The idea is demonstrated in the following.

Two lines of different curvature, e.g.

$$y = a_i x^{b_i}, \tag{5.9}$$

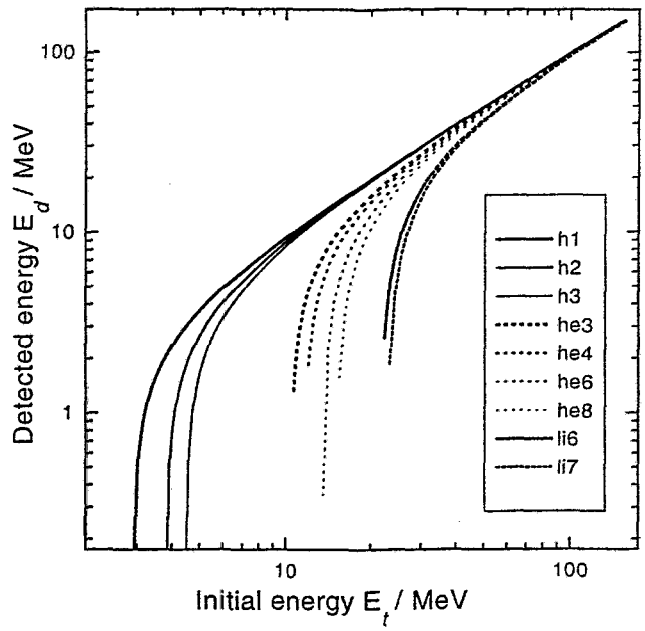

Figure 5.7: *Energy losses of the LCPs on their flight path from the target to the CsI(Tl) detector. They were calculated using the code STOPPOW [104].*

can unambiguously be scaled to pass through two arbitrarily chosen points in some area (x, y) by means of the transformation

$$k_y y = a_i (k_x x)^{b_i}, \tag{5.10}$$

where the coefficients k_x and k_y can be defined analytically.

Such a transformation cannot be applied directly to the experimental PIMs, because the particle branches are not significantly curved. Thus, small discrepancies in the shapes of the particle branches in the PIMs together with the effect of noise lead to intolerable uncertainties. Non-linearities of such kind introduce variations of the coefficients b_i of about 13% and 26% for protons and α-particles, respectively.

Therefore, we constructed a model of the "ideal" PIM using empirical functions for the description of the particle branches,

$$F_{ideal}(L_{fast_i}, L_{slow_i}, A_i, Z_i) = 0, \tag{5.11}$$

where the index i denotes the type of particle (Z, A). The coefficients k_{fast} and k_{slow} are found by minimization of a χ^2-like functional

$$\sum_i F_{ideal}(k_{fast} L_{fast_i}, k_{slow} L_{slow_i}, A_i, Z_i) = min. \tag{5.12}$$

Of course, a suitable choice of F_{ideal} is important. Functions of the form like eq. 5.9 in general fit the particle branches well. But they fail in the region of low energ;, that becomes critical for the PIMs of backward-positioned detectors. Therefore, we use functions of the form of eq.5.8 for L_{slow} and L_{fast}. Then the corresponding functional becomes

$$\chi^2 = \sum_j (k_y Y_j - F(k_x X_j))^2, \tag{5.13}$$

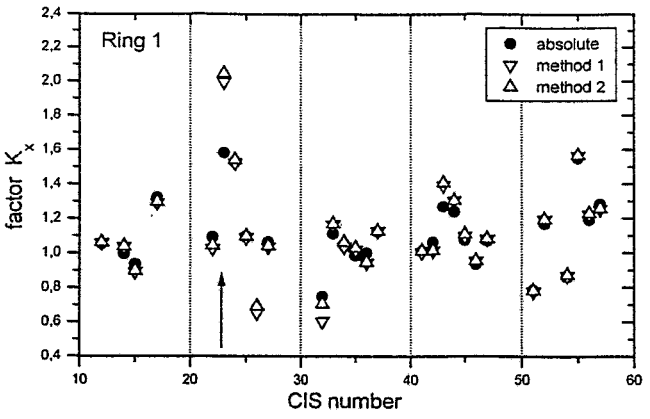

Figure 5.8: *Comparison between the both χ^2-calculation methods and using punch-trough points ("absolute"). They are identical for the most of detectors. The arrow shows an exception, where due to some quality reasons the discrepancy is significant.*

where X and Y are the two components of the PSA, j denotes a point in the experimental PIM, and F represents any function $X = F(Y, Z, A)$ of the type like eq. 5.11.

There is also another way to define the χ^2-like functional.

$$\chi^2 = \sum_j (Y_j - F(k_x X_j)/k_y)^2. \tag{5.14}$$

The points (X_j, Y_j) are arbitrarily but nearly equidistantly scanned along the entire particle branches of the PIM. The coefficients k_x and k_y are then obtained numerically by setting the derivatives $d\chi^2/dk_x$ and $d\chi^2/dk_y$ equal to zero.

The solutions of eqs. 5.13 and 5.14 are found to be identical for PIMs with well resolved particle branches. They also perfectly describe the PIMs with pronounced PTPs (fig. 5.8). Discrepancies with respect to less resolved PIMs or PIMs without pronounced PTPs are significantly larger for eq. 5.14 than for eq. 5.13, but a comparison of the coefficients obtained for PIMs with and without PTPs do not lead to a preference of one of these equations. This fact indicates some limits of such a procedure. Nevertheless, the precision of the shape-scaling method was estimated to be about 5% with respect to the energy scale. This is illustrated in fig. 5.9.

5.5 Check of the calibration

A special test measurement was carried out to check the reliability of the calibration procedure. In this measurement a BIC was used as the ΔE detector, and the CsI(Tl) scintillator measured the residual energy [76]. In spite of the special operation mode of the BIC, this test was more qualitative than quantitative because of the large uncertainties due to the small ΔE signals of α-particles, the limited dynamic range and the generally low registration efficiency of the BICs for LCPs.

Unfortunately, light particles beams are not available in the experimental area of FOBOS technical reasons. Therefore, a direct energy calibration was not performed. The TOF for scintillators were used only qualitatively in order to locate data from neighbouring

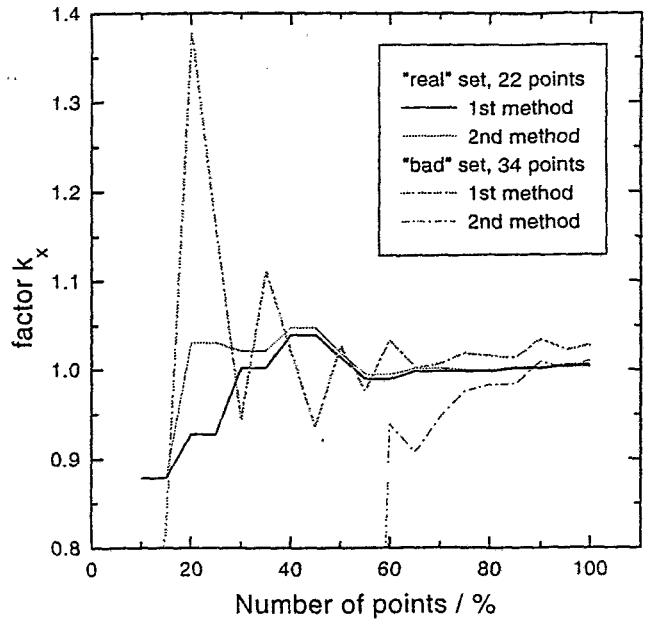

Figure 5.9: *Coefficients obtained for the shape-scaling of the "ideal" particle identification matrix to itself. They are based on the particle branches of protons and α-particles. The abscissa corresponds to that part of points which were used for scaling, counted from the side of lower energy. The "real" set was scanned as usual, and the "bad" set was scanned under the assumption of some oscillation of the points around the particle branch within $\pm 2\%$ of the actual value of the coordinates. The 1st and 2nd method of χ^2-calculation is in correspondence with their order of description in the text.*

bunches appropriately, because the necessary correction for the TOF drift (caused by the cyclotron HF phase drift) was performed later.

A quantitative check of the calibration method was performed by comparing the results for the 10 mm thick crystals with those of the 15 mm thick ones. Such comparison is reliable, if the transparency of the CsI(Tl) crystals is high enough. The PIM of the thick crystal was scaled to that of the thinner one by means of the scaling procedure which considered the *shapes* of the particle branches. The result is shown in fig. 5.10.

Finally, we estimated the precision of the calibration procedure described in this work as being better than 10%, i.e. of the order of the energy resolution of the CsI(Tl) detectors. This has been verified involving such additional references as the resulting shapes of the energy spectra of LCPs measured by different detectors but at the same polar angle, or the spectra of the γ-rays.

This method has been applied for the first time for the calibration of the CsI(Tl) detectors of the scintillator shell of the FOBOS array in the JAN96 experiments carried out to investigate the decay of hot heavy nuclei produced in the reactions ^{14}N (53 AMeV) + ^{232}Th and ^{197}Au [107]. Calibrated α-particle spectra measured in these experiments [108] are shown for illustration in fig. 5.11.

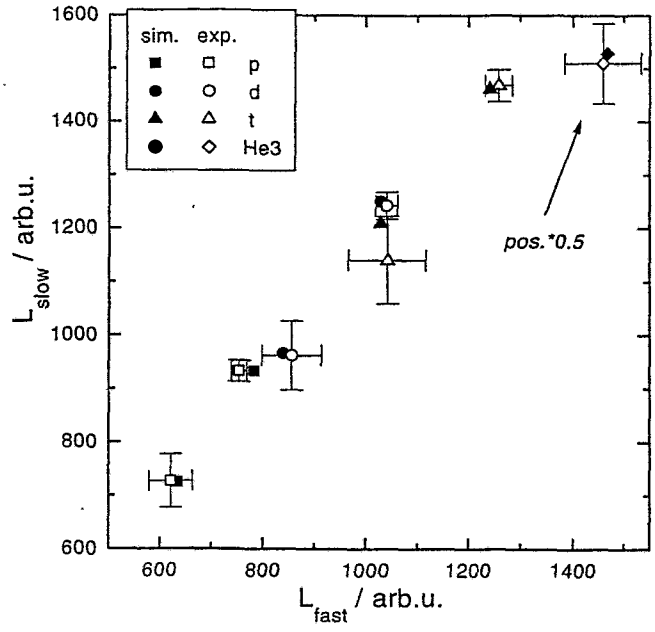

Figure 5.10: *Comparison of the simulated coordinates of the punch-through points (solid symbols) with the measured ones (open symbols). The points with larger error bars (except for ^3He) correspond to a 10 mm thick crystal and were obtained by applying the shape-scaling. The points for ^3He are, for convenience, multiplied by a factor of 0.5.*

5.6 Final remarks

The actual properties of the CsI(Tl) crystals used may slightly differ from those crystals investigated in ref. [75], and the parameters in eqs. 5.2–5.4 may not be ideally suited for our simulations. A general adjustment of these parameters was performed by fitting the simulated PIM to the measured ones. However, it turned out that this was not necessary on the level of accuracy required. Agreement of simulated and measured PIMs was achieved with $\tau_{slow} = 4\,\mu s$. Such a value for the slow decay constant has likewise been found for CsI(Tl) crystals [109] delivered by the same manufacturer.

In principle, the simulation of the PIM would require to carry out measurements of the scintillation light pulse-shapes for the CsI(Tl) crystals used, like it has been done in ref. [75] using high frequency signal sampling, or with thin slices of the same CsI(Tl) scintillator material like in ref. [105]. On the other hand, the general view of measured PIMs could be reproduced even by simulations based on relatively rough approximations for $R(E,q)$ and $\tau_{fast}(E,q)$, for example with the expressions

$$R(E,q) = 0.2227(E/q)^{1/3}, \tag{5.15}$$

$$\tau_{fast}(E,q) = 390 + 200(E/q)^{1/3}, \tag{5.16}$$

and the precision of the energy scale obtained for the LCP spectra is comparable with the energy resolution of the CsI(Tl) detectors. However, it is impossible then to fit the shape of particle branches.

It seems also possible to perform in the same manner a simulation and, thus, a calibration of descending particle branches, characterized by higher energies $E > E_{PTP}$. It

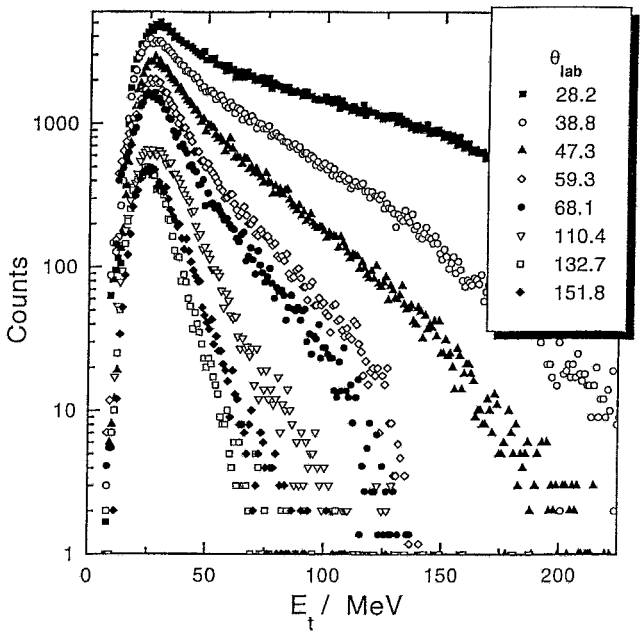

Figure 5.11: *α-particle spectra from the reaction ^{14}N (53 AMeV) + ^{232}Th accumulated into $\Delta\Omega$=0.16 sr for each laboratory angle ϑ_{lab} (40% of the entire data body).*

requires, however, some additional assumptions on the scintillation process.

The uncertainty of the detected E_d is naturally largest for lowest particle energies. On the other hand side, at the FOBOS detector, the energy loss of LCPs in piersed layers of other detector materials are in this case larger than the residual energy E_d. Thus, the necessary corrections for the energy loss introduce the dominating part into resulting $E_t(L_{fast})$ at small energies, and, therefore, the relative error of E_t is reduced.

The shaping time of 3 μs in the measurement of the total light output of CsI(Tl) in ref. [93] does not significantly affect the final result for energies larger than a few AMeV. This shaping time is, however, implicitly assumed in eq. 5.6, therefore the corresponding correction for the simulation at lower LCP energies is taken into account.

The influence of the rise-time of the scintillation light pulse can be neglected ($\tau_{front} = 0$, $h_{front} = 0$), if the time gate Δt_{fast} does not cover the initial part of the CsI(Tl) detector signal. As reported in ref. [75], the rise-time for electrons is about 40 ns, and even shorter for high-ionizing particles, but the timing properties of the photomultiplier used have to be taken into account.

Performing the above mentioned TOF drift correction, one can get a reliable energy calibration on the level of accuracy required even in spite of rather poor time resolution (fig. 5.12, left panel). The method is described in ref. [110]. One measures an averaged function TOF(L_{fast}) and uses the calculated TOF for a certain measured L_{fast} value. The time resolution becomes much better in the absence of scattering on supporting and coordinate grids and straggling in gas and foils (fig. 5.12, right panel); this was observed in MAR97 experiment in those modules were the gas detectors were removed in order to record LCP spectra without thresholds and distortions. On the other hand, some other difficulties arise from contamination of a scintillator PIM with FF. The PSA discrimination between He and FF is impossible - the FF spot overlaps with the low energy

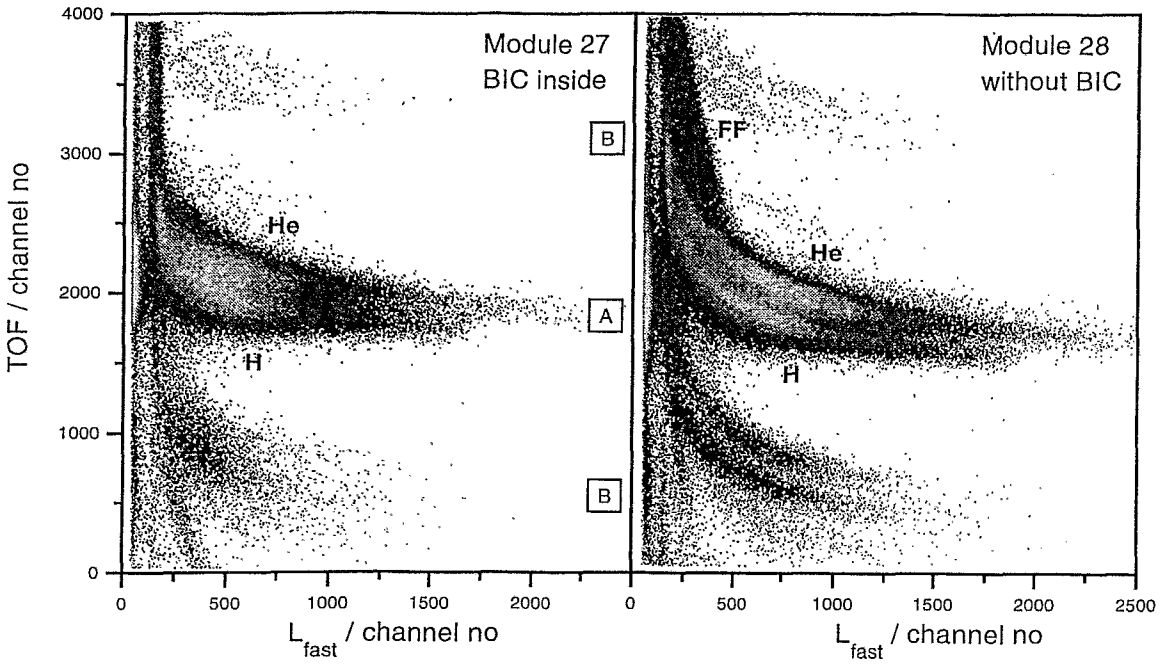

Figure 5.12: *Time of flight vs fast light component plots from MAR97 experiments. The bulk of counts from the right bunch (A) is surrounded by spots from neighboring bunches (B) standing* $\approx$ 54.9 *ns from each other. The difference in the time resolution for the regular case (left panel) and empty module (right panel) is obvious. The line corresponding to heavy particles (FF) arises in absence of foils and gas in a flight path.*

part of the He line. In this case only a careful TOF-E analysis provides the separation. Besides of the TOF based calibration, just a comparison between the spectra accumulated by modules with and without BIC can be used as an additional calibration check.

Taking into account all the above notes, one can assume this calibration method to be suited for the FOBOS scintillator shell. The following advantages of the described calibration procedure should be emphasized:

- Special calibration measurements are not necessary.
- It does not rely on measurements of the total light output.
- All 210 CsI(Tl) detectors can be calibrated in an unique manner by scaling the individual PIMs to an "ideal" one.
- It enables a high degree of automatisation for data processing, no setting of particle-gates manually is required
- Some visual inspection and check of data quality can be easily performed during the data processing.

Chapter 6

Experimental results

6.1 Main observables and parameters

Two main physical observables are used as parameters: mass-asymmetry and initial excitation energy. Despite some obvious correlations they can be treated independently.

The FOBOS detector is capable of registering fission-like events up to very asymmetric mass splits in a broad range of initial excitation energies. The limitations of the whole geometrical efficiency and the lack of neutron data prevent reconstruction of each event by means of energy and momenta balance. Therefore, attention has been paid to correlations between observables as an additional check for data consistency.

It will be shown that only a multi-dimensional analysis of the data involving some unusual coordinates can separate different reaction channels. However, conventional methods of the analysis were also tried and were compared with previously obtained results.

6.1.1 Excitation energy

The excitation energy is treated in the framework of the Massive-Transfer-Model [4]. For central collisions of very asymmetric projectile-target combinations, a linear correlation between the portion of the linear momentum transferred from the projectile to the target and the excitation energy E^* imparted to the system is well established [111]. The ratio between the linear momentum of the compound system P and that of a completely fused system P_{max} is used as a measure of the imparted (or initial) excitation energy E^*

$$E^* \approx E^{cm}_{beam} \frac{P}{P_{max}}, \tag{6.1}$$

where E^{cm}_{beam} is the projectile energy in the center-of-mass system. This energy for a 53 AMeV ^{14}N beam amounts to 50 AMeV for the Th target and 49.5 AMeV for the Au target. The 100%-LMT corresponds to a linear momentum of 4.392 GeV/c. The calculated limit of the induced excitation energy amounts to 699.8 MeV for complete fusion of the beam particle with ^{232}Th and 692.8 MeV for ^{197}Au, respectively. The beam velocity amounts to 10.11 cm/ns.

Most of the induced E^* is spent usually by the emission on neutrons and LCP during the de-excitation cascade. This causes an anticorrelation between the calculated composite system momentum P and the total heavy fragment masse $M = A_H + A_L$ (The indices H and L denote the heavier and the lighter fragments). Such an anticorrelation

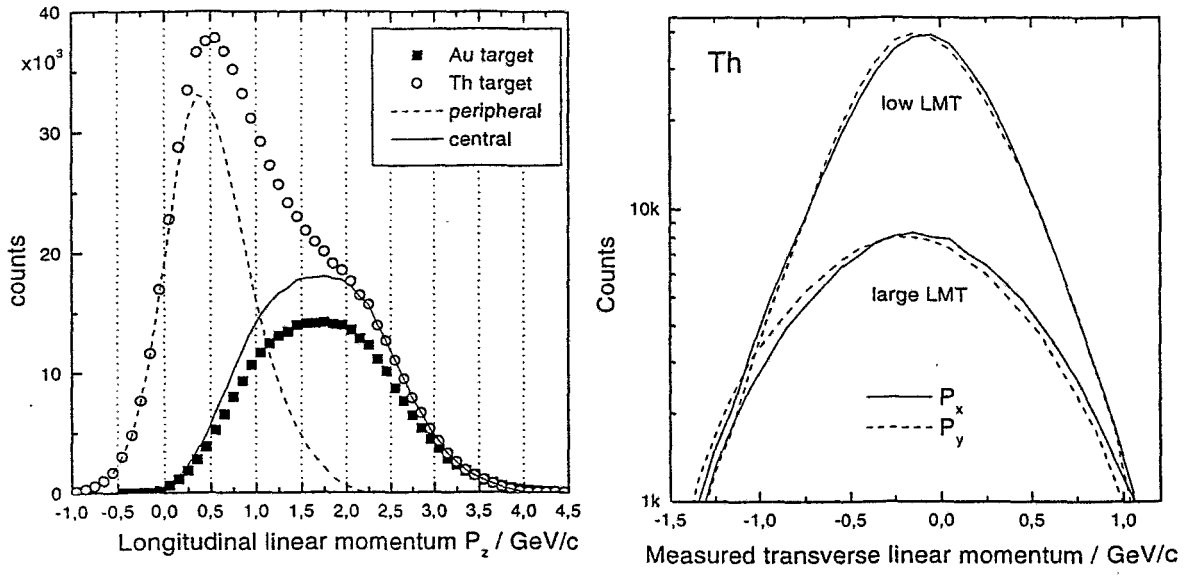

Figure 6.1: *Left panel: The experimental distribution of the composite system's linear momentum from reactions on Au and Th target nuclei. The decomposition into peripheral and central collisions is shown for Th-data (see text). Right panel: The distributions of transverse-to-beam components of the system's linear momentum for Th-data is also indicated. The asymmetry around zero is caused by the non-symmetric geometrical acceptance.*

is observed and the linear dependence is deduced [112]. An averaged amount of energy of about 14 MeV (binding and kinetic energy) is carried away per evaporated nucleon from a composite systems produced in central collisions.

The experimental distribution of the linear momentum component parallel to the beam axis P_z used for the excitation energy calculation is given in fig. 6.1 (left panel). Fission after peripheral collisions is strongly suppressed in Au, because fission barriers for nuclei around ^{197}Au are significantly larger than those for nuclei near ^{232}Th. Thus, the distribution for Th data reveals two components, the component corresponding to larger values is perfectly reproduced by the form of the distribution for Au. The additional component in the spectrum of the linear momentum for Th corresponds to peripheral collisions, this component is missing in the case of Au. Some negative values of P_z occur because an influence of LCP evaporation onto the momentum balance at a low LMT is significant, and a negative value corresponds to forward-emitted energetic LCPs and IMFs.

The direction of the restored linear momentum vector of the composite system does not coincide in general with the beam axis. The influence of the particle evaporation from both the composite system and from the fragments is illustrated by distributions of the linear momentum transverse to the beam in fig. 6.1 (right panel). The increase of the distribution width with increasing the LMT was shown earlier in fig. 4.12. This is also an effect of the particle evaporation, which turns out to be more intense at higher excitation energies. Emission of particles into the backward hemisphere leads, in the same sense, to values of the longitudinal velocity $V_z = P_z/M$ exceeding $V_{max} = P_{max}/M$ (this will be reflected in fig. 6.10).

6.1.2 Mass-asymmetry

Conventional mass-asymmetry

The simplest way to analyze the mass-asymmetry consists in considering different mass bins in the mass distribution of the fission-like fragments. This method, however, has a serious disadvantage if the composite system is not well defined. For instance, defining for the actual mass-distribution of fragments from the Au-target in fig. 6.2 large, intermediate and small asymmetries simply by means of the mass ratio, one observes that some masses belong to all asymmetries. This indicates the necessity to introduce an other mass-asymmetry criterion.

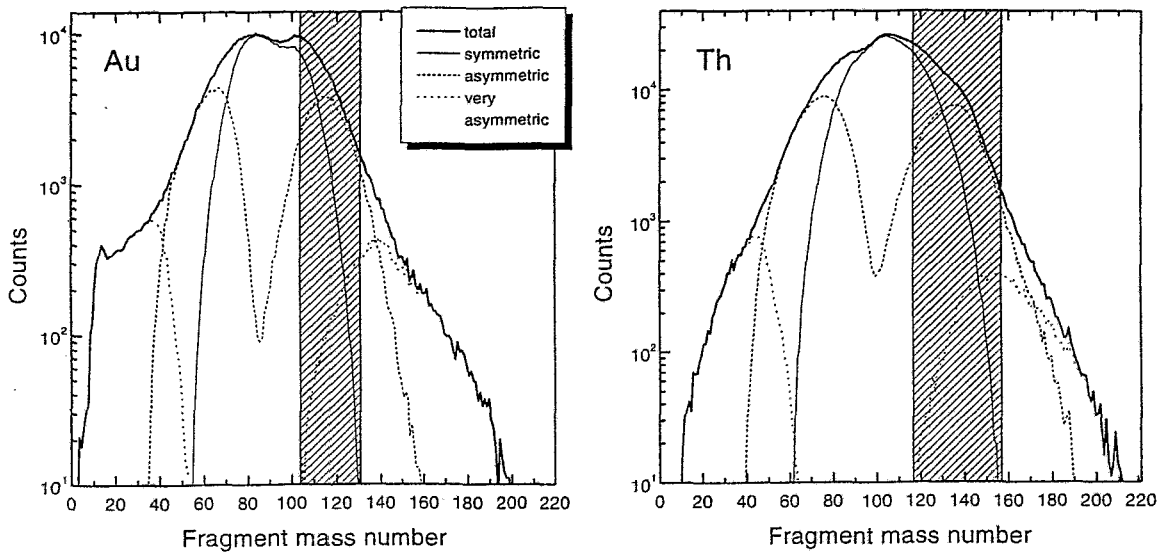

Figure 6.2: *Fission-like fragment mass distributions obtained from Au (left) and Th (right) targets. Three bins in mass-asymmetry are overlapping within the hatched area.*

Different definitions of the mass-asymmetry are used in this thesis. The definition of the mass-asymmetry parameter β as a simple ratio of the fragment mass numbers[1]

$$\beta = A_H/A_L \tag{6.2}$$

is obvious, but the definition

$$\chi = \frac{A_H - A_L}{A_H + A_L} \tag{6.3}$$

is used for data visualization. The parameter χ is convenient because it is normalized to unity, while the distribution of β is concentrated in a narrow region of low values (fig. 6.3, left panel). The relation between χ and β is obvious.

Experimental distributions of mass-asymmetries are shown in fig. 6.3 (right panel). Masses of fission fragments observed in the gas detectors extent down to LCPs. A reasonable statistical accuracy is obtained even for mass splits as large as 1:10. A dropping down of the mass-asymmetry distributions at $\chi > 0.86$ is observed. This reflects the

[1] In fact experimentally measured masses are used

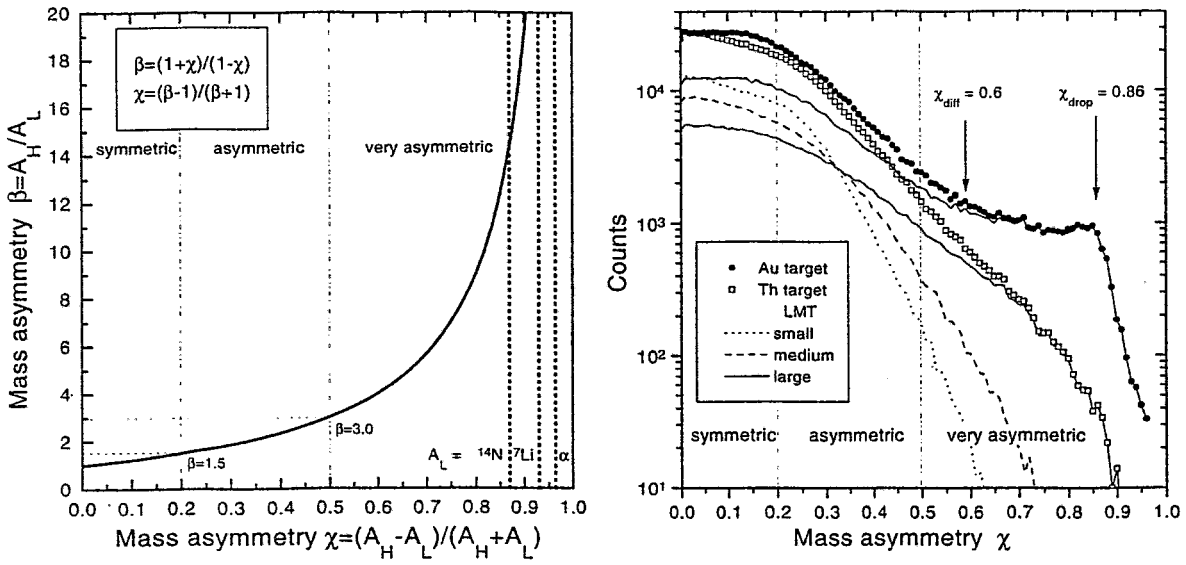

Figure 6.3: *Left panel: Two different representations of the mass-asymmetry; dotted lines mark χ values for given light particles (A_L) and A_H ≈200-230. Right panel: Experimental distributions of asymmetries for the reaction ^{14}N (53 AMeV) + ^{197}Au (circles) and ^{232}Th (squares) and the decomposition of the latter into spectra accumulated in different LMT regions (for Au only the high LMT contribution is shown).*

decrease of registration efficiency of light ions by the gas detectors as well as the diminishing of geometrical acceptance for highly asymmetric FF pairs. It seems appropriate to assign the terms symmetric, asymmetric and very mass-asymmetric to the bins indicated in fig. 6.3 (right panel).

A significant difference in the form of these spectra is observed for χ_{diff}>0.55, which can be explained qualitatively. The most probable composite nucleus originating in reactions of the JAN96[2] series is close to the target nucleus, as it has been predicted by simulations [5]. In contrast to Au, the Th nucleus is easily fissile. This means that after a very asymmetric first split the still highly fissile heavy remnant can undergo sequential fission, and one observes a ternary event. The registration probability of a ternary event is, of course, lower than that of a binary event. But, if the lightest particle is lost from recording the remaining two heavy fragments contribute to a rather symmetric channel; if one heavy fragments is lost from recording then such an event should be rejected by the data filter.

Some simple estimation seems to be helpful for understanding this phenomenon, if only ternary events are responsible for the difference in the spectra. As it is seen from the data, fission of a Au-like compound nuclei still occurs at relatively small excitation energies. Therefore, the sequential fission of the Th-like composite system can happen if the mass of the heavier fragment from the first split is comparable with Au or even a little smaller. If the first scission is fast and most of the nucleons as well as excitation energy remains in the system, then the critical value can be estimated by χ_{diff} ≈0.6. Indeed, the observed value of χ_{diff} is between 0.55 and 0.6. If one assumes evaporation of a large

[2]See Section 2.5 for the experiment designation.

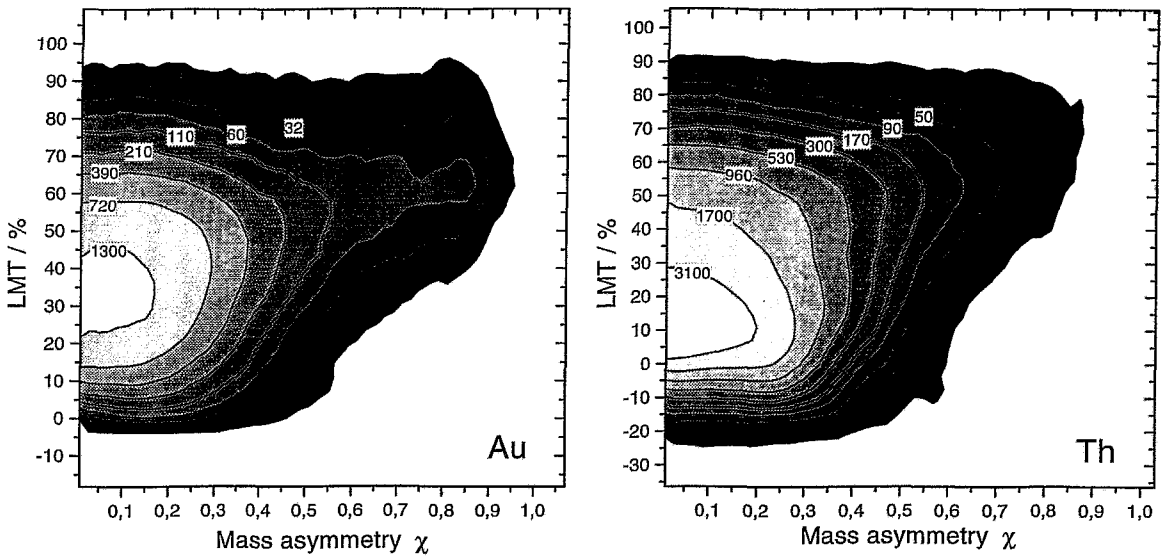

Figure 6.4: *Experimental distribution of measured LMT (related to the initial excitation energy) vs mass-asymmetry in the reaction with ^{14}N (53 AMeV) projectile on ^{197}Au (left) and ^{232}Th (right) targets. Numbers denote contour line levels, the outer line corresponds to a level of 5 counts. Matrices are slightly smoothed to suppress noise in the outer contours.*

number of nucleons from the Th-like composite system, the value of χ_{diff} should increase significantly. On the contrary, an intensive evaporation from the heavier fragment reduces χ_{diff}. One cannot derive quantitative results from this rough estimation. However, this picture is consistent with the implementation of very asymmetric fission as a fast process at relatively high excitation energy [113]. Indeed, most asymmetric mass splits in both the Th and Au data are observed at high LMT. However, as fig. 6.4 indicates, there is no correlation between mass-asymmetry and LMT, i.e. these quantities can be used as independent variables.

Primary and secondary mass-asymmetry

Due to the evaporation of particles from fission fragments the mass-asymmetry at scission should differ from the measured one. The mass-asymmetry parameters introduced in eqs. 6.2 and 6.3 are actually related to the instant of registration by the detectors, i.e. they refer to secondary masses and secondary asymmetry.

Since the mass of the scissioning nucleus is not well defined, one cannot measure primary masses of the fragments directly. Assuming momentum conservation one gets, however, their mass ratio. The transverse momenta of the fragments in the lab system are equal :

$$m_1 v_1 \sin\theta_1 = m_2 v_2 \sin\theta_2, \tag{6.4}$$

where velocities and angles are experimental observables. It is conjectured that light particles are evaporated isotropically and, hence, do not change velocities and angles of the fragments, on the average. Using the provisional mass ratio $R_v = m_1/m_2$, the primary

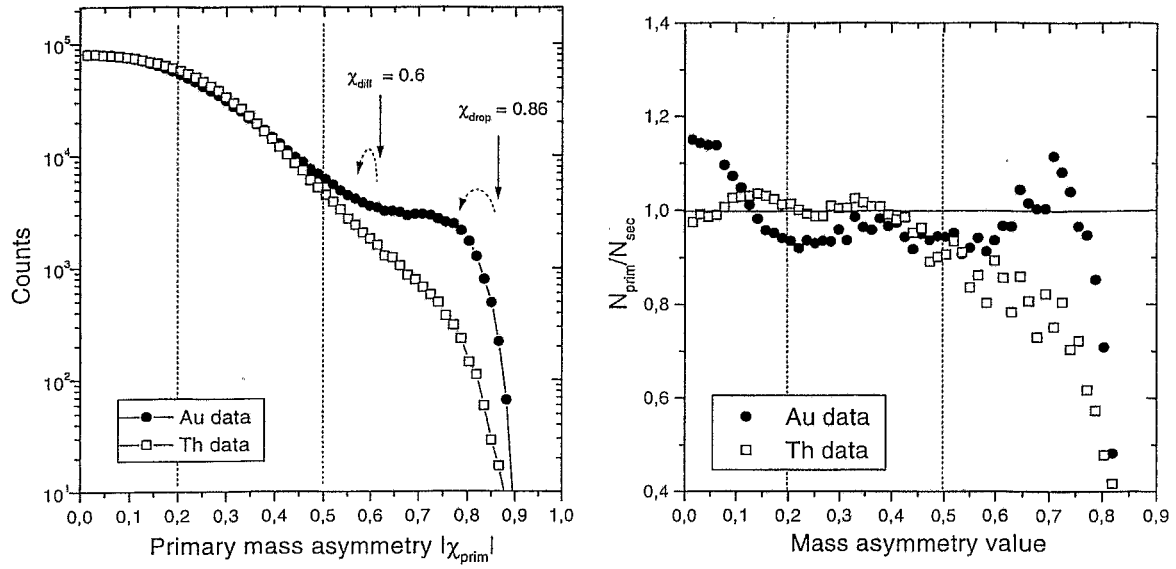

Figure 6.5: *Left panel: Experimental distributions of the primary mass-asymmetry for Th and Au data, a shift is found in comparison to the secondary asymmetry spectra (fig. 6.3). Right panel: The difference between spectra is illustrated by the formally introduced ratio (see text) of primary to secondary asymmetries.*

mass-asymmetry then can be defined as

$$\chi_{prim} = \frac{R_v - 1}{R_v + 1}. \tag{6.5}$$

Index "v" indicates that this ratio is based on the velocity analysis. This primary mass-asymmetry essentially differs from that of eq. 6.3, which is calculated from the secondary masses measured by the detectors. The symbol R_v used instead of β_{prim} stresses again that the primary masses are unknown. Note, that χ_{prim} could assume negative values.

The distributions of the primary mass-asymmetry are shown in fig. 6.5 (left panel). They generally look like secondary asymmetry distributions (fig. 6.3), however, the critical points are shifted towards smaller asymmetries. It is difficult to observe all such peculiarities because of the logarithmic scale. In order to make visible the difference the ratio of these spectra is formally introduced (fig. 6.5, right panel). By definition, total count numbers in the spectra of primary and secondary asymmetries are equal, however, events with a certain value of mass-asymmetry χ_{prim} may be found at a different value of χ. Therefore, the complicated behavior of this ratio reflects the fact that post-scission emission plays an essential role in formation of the secondary mass distribution. We will dwell on this point by introducing in Section 6.3 the mass-asymmetry matrix as a more appropriate method to explore the mass-asymmetry.

6.1.3 Total kinetic energy and masses

The total kinetic energy (TKE) *vs* fragment mass distributions (TKE-M) for the Au and Th data are given in fig. 6.6. They have the typical fission-like banana form. The distribution for Th is slightly broader than that for Au and displays a single hump while

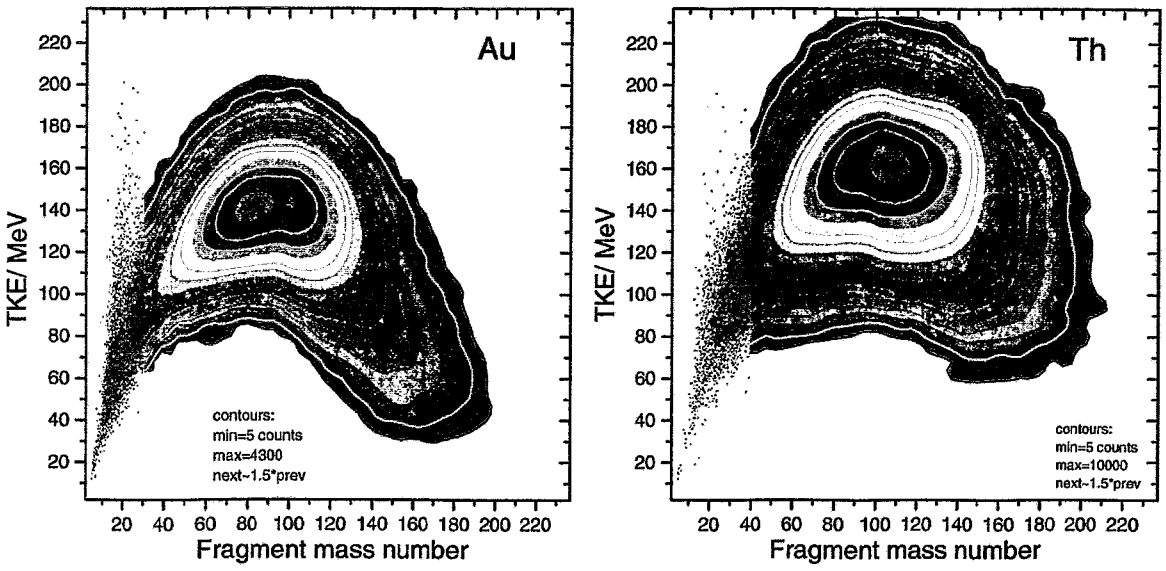

Figure 6.6: *Experimental distributions of total kinetic energy vs fragment mass (TKE-M). The contour plot in the low mass region is replaced by the scatter plot in order to see details.*

the top of the distribution for Au has a double-humped structure as it is also observed in the fragment mass distribution (fig. 6.2).

The broad top of the TKE-M distribution for Au survives even if only symmetric events are selected. Setting $|\chi_{prim}|<0.05$ (corresponding to 10% of the fragment mass difference) one observes a slant oval spot probably being the superposition of two broad overlapping peaks. A similar behavior is observed in the LMT-M and TKE-LMT plots. The distribution of the total fragment mass can be well approximated by two Gaussian with the mean total masses of 176 and 191 units, respectively. These components correspond to large and small LMT (or high and low excitation energy: HE and LE). The double-Gaussian fits with respect to the total mass as well as LMT are shown in fig. 6.7. The corresponding values of the mean excitation energy and the average TKE are summarized in tab. 6.1.

The same procedure performed for the Th-data delivers mean total masses of 210 and 201 units for the LE and HE peaks, respectively. The bump of peripheral collisions (fig. 6.7) at small LMT or lowest excitation energies corresponds to a mean total mass number of 221. The numerical data are also given in tab. 6.1. The uncertainty of

Table 6.1: Components in the TKE-M distributions for most symmetric splitting ($|\chi_{prim}|<0.05$).

Data	Th			Au		
Peak ID	Periph.	LE	HE	Periph.	LE	HE
$<M>$ / u	221	210	201	-	191	176
<TKE> / MeV	162	161	158	-	148	136
$<E^*>$ / MeV	60	160	300	-	160	300

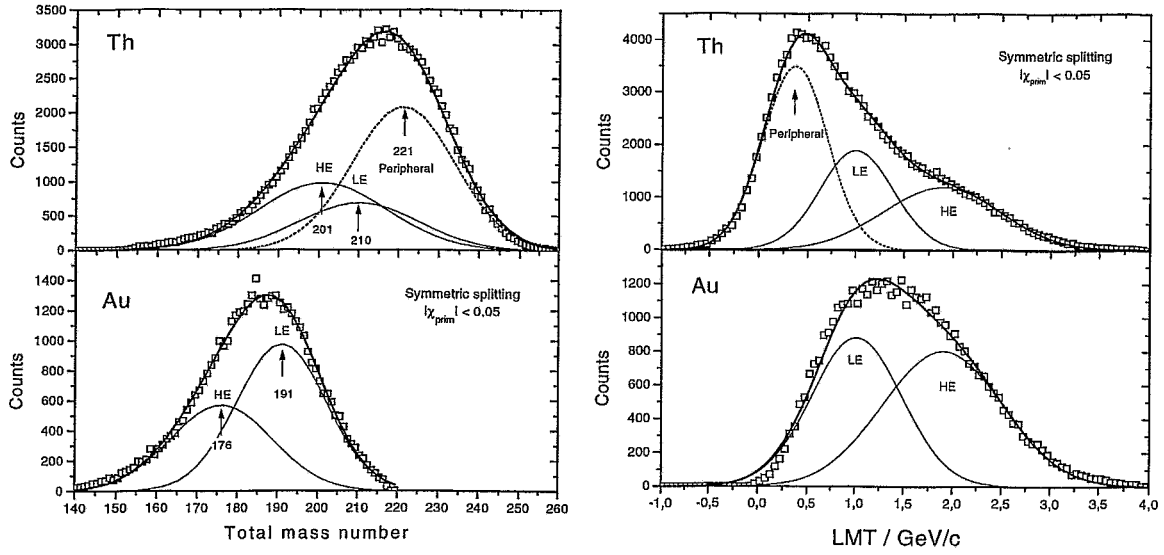

Figure 6.7: *Gaussian decomposition of the total mass distribution of the fission fragments by low energetic (LE), high energetic (HE) and peripheral (for Th-data) components for the most symmetric mass splits (left panel) and respective decomposition of LMT distributions (right panel).*

the extracted mass values amounts to about 2%. Except for that additional peripheral component, it seems that the TKE-M matrix for the Th-data has in general a similar composition like that for the Au data.

As it was expected from the mass-asymmetry analysis, an other difference between the Th and Au data is found at low fragment masses. Therefore, the mass region under consideration is shown as a scatterplot (fig. 6.6), because the structure would not be seen in the contour plots [3]. TKE values significantly larger than fission-like ones are observed in the Au-data and they are nearly absent in the case of Th. Such an effect was already observed in ref. [111] and treated as dynamical emission of IMFs.

In order to describe the entire TKE distribution, the extended TKE systematics recently introduced by Wagner [35] is used:

$$TKE = 0.29 \frac{Z^2}{A_1^{1/3} + A_2^{1/3} - A_{tot}^{1/3}} \times \frac{A_1 A_2}{A_{tot}^2}, \tag{6.6}$$

where $A_{tot} = A_1 + A_2$ and Z is the charge of the compound system.

The charge of the fissioning nucleus is estimated assuming the multiplicity of evaporated neutrons being approximately ten times larger than that of protons. Therefore, one can subtract one proton per ten neutrons, starting from the Th nucleus for peripheral collisions. The corresponding TKEs, plotted as lines in fig. 6.8, well describe the average banana form of the TKE-M matrix. In the case of Th these lines nicely follow the ridge of the distribution up to its maximum.

The situation for the Au data is quite different, there is no way to describe the TKE-M distribution in the same manner as in the case of Th target. The BUU [114] simulation

[3] This effect is much stronger in the data from the reactions ^{40}Ar (36 AMeV) + ^{248}Cm and ^{nat}Ag

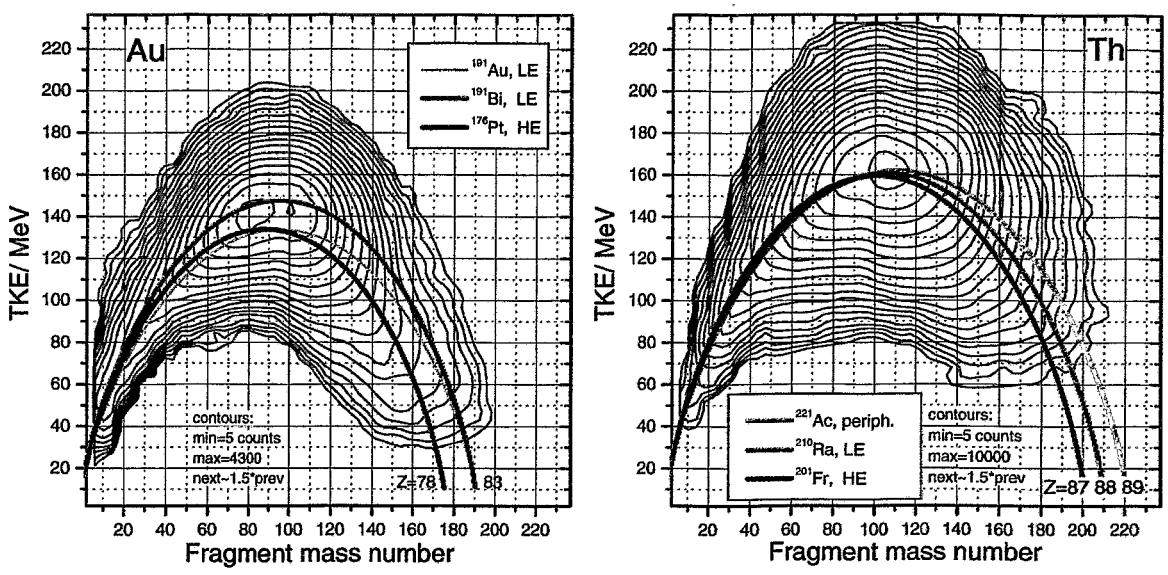

Figure 6.8: *TKE-M lines for certain elements calculated by eq. 6.6 superimposed on actual distributions.*

predicts for the fissioning system $<Z>$=79.5 [5]. However, the corresponding TKE-lines for $Z = 79$ and $Z = 78$ are not adequate to the matrix shape (see left panel in fig. 6.2). Using the corresponding value of the TKE from table 6.1 one finds that $Z = 83$ is the only appropriate charge. Consequently, TKE-lines for ^{191}Bi and ^{176}Pt seem to be responsible for the observed shape of the TKE-M distribution for the Au data.

Since the dominating amount of fission events is symmetric, one can use the extracted Z and A as limits to estimate the most probable composite systems. (Of course, some nucleons are still evaporated after scission.) It has been already observed with the mini-FOBOS that for heavier projectiles the reaction is clearly dominated by two channels with low and high linear momentum transfer [115]. This split is probably not so clearly pronounced in the present data because of the light projectile. However, the two peaks observed might probably also be considered in our case as representing two reaction channels.

Despite a reasonable representation of the LMT and total mass spectra by three Gaussians for the symmetric mass splitting in the Th-data, the attempt to apply the same procedure to the charge spectra of the composite system fails. Using the extended TKE formula 6.6 one can extract Z event-by-event, the spectra of Z obtained in this way are presented in fig. 6.9.

First of all, the spectrum of Z for near symmetric mass splits looks similar to that for the entire Th data. The spectrum for the entire Au data is slightly broader as that for symmetric splits and shifted to lower Z values. This difference between the Th and the Au data could be due to the dominating contribution of peripheral collisions in the case of Th. Fixing Z values at 83 (HE) and 78 (LE) one can well describe the Au data in the case of symmetric splitting (right panel). Fitting the peak position results in mean Z values of 83.3 (LE) and 80.7 (HE) (left panel) [4]. It is important, that the contributions in

[4]These values agree better with the widely used empirical rule which estimate the incomplete fusion result as target plus half of the projectile than with the already quoted BUU predictions.

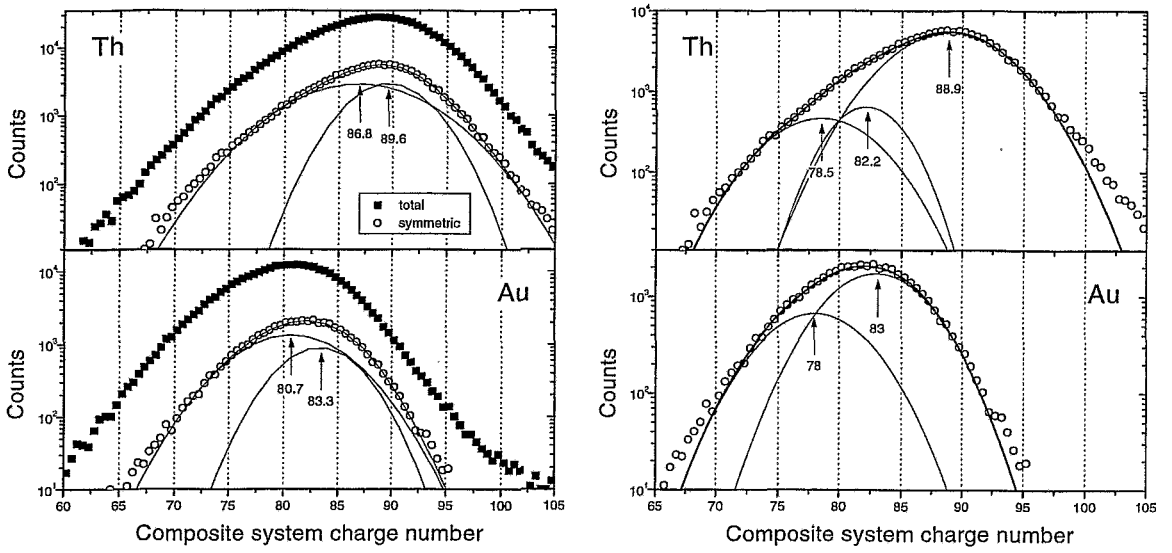

Figure 6.9: *Calculated distributions of the composite system's charge applying the TKE formula 6.6 for the whole data set (solid squares) or for the most symmetric mass splits (open circles). Fits with free parameters (left panel) and with fixed peak positions for Au and the three peak requirement for Th (right panel).*

either case have comparable magnitudes (as it was the case for the total mass and LMT), because the decomposition is not a real multidimensional fit. All above argues in favor of the reliability of these Z-spectra.

The Z-spectrum for the Th data, however, cannot be well approximated using mean Z values derived from mean TKEs. A three-Gaussian fit results in either suppressing one of the contributions (left panel) or yielding a contributions far off the expected ones (right panel). The peripheral component is peaked, as it is expected near 89, but its magnitude becomes too small in the first case and too large in the second case. Assuming that the measured and calculated TKE as well as the mass data are correct, one should also suppose the existence of at least two reaction channels leading to different TKE at equal charge of the composite system or vice versa. This statement in any case would not contradict the above described decomposition of the mass and LMT spectra (fig. 6.7).

One further interesting observation is presented in fig. 6.10. The distributions of the average TKE and the total mass for Th reveal clearly visible double-component structures (as in fig. 6.1). The component corresponding to central collisions looks like the distribution for Au. The distributions at the lowest and the highest relative values represent only a few counts which may contain accidental coincidences. They are excluded from the further discussion.

The rise of the average TKE in Au at low LMT up to a certain value and further decrease could be interpreted by the balance between the growing fused part of the projectile and an increasing removal of nucleons by evaporation. The average behaviour of the total mass replicates the form of the mean TKE up to an intermediate LMT of about 2 GeV/c (open symbols). The further growing of the total mass might be only explained by assuming the existence of a fast process, meaning that particles have no time to be evaporated. Such an argument would explain the contradiction found between TKE and

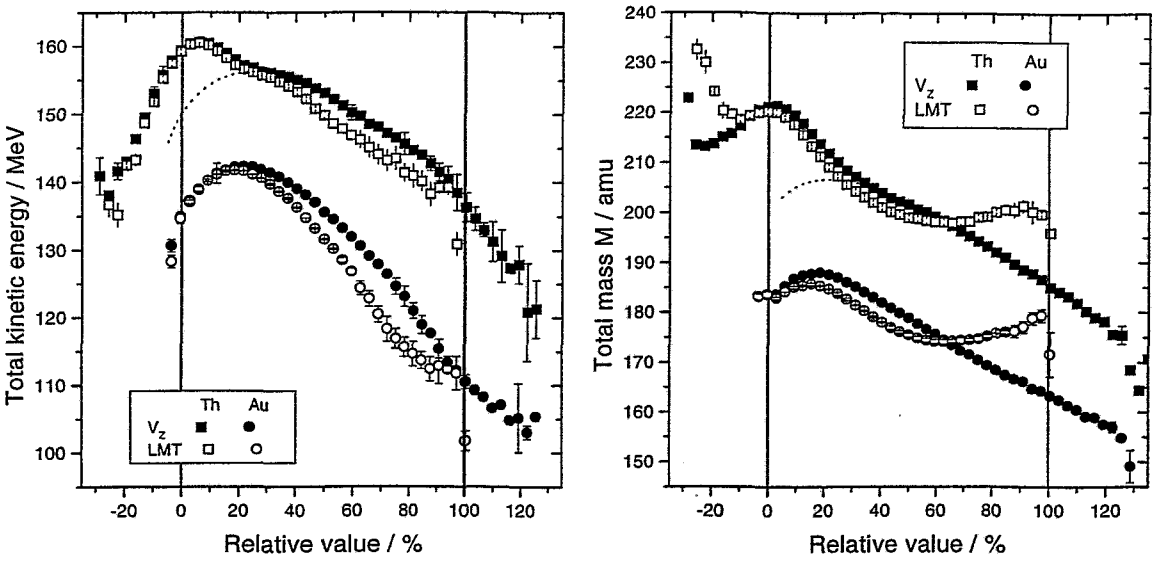

Figure 6.10: *Mean TKE (left) and fragment mass sum (right) as a function of the transferred linear momentum (solid symbols) and of the system's velocity (open symbols) relative to their values for complete fusion. The Au-like component in curves for Th is marked by eye-guiding dotted lines.*

total mass data if one presumes conventional fission only [5].

The TKE and total mass distributions as a function of the system's longitudinal velocity V_Z relative to that of complete fusion (see fig. 6.10) both for Th and Au also reveal a peak at low values, but then they decrease monotonously (solid symbols). Such a difference between these distributions and those *vs* LMT could indicate that eq. 6.1 is inadequate in describing the actual imparted excitation energy. The distributions *vs* the relative velocity spread far over 100%. This should point to pre-equilibrium emission into the backward hemisphere in the most central collisions. This fact will be illustrated by the LCP data in the next Section.

6.2 Analysis of the LCP data

One of the most important tasks to be solved with the scintillator shell of the FOBOS detector is the determination of pre- and post-scission multiplicities. Therefore, even in the first experiment with only a few scintillator modules mounted, we have tried to separate particles originating from different sources [116]. The primary LCP data analysis aimed at checking the data from both the gas detectors and the scintillator shell by means of physically significant correlations between heavy fragments and LCP.

[5]Note that the region of linear anticorrelation between total mass and LMT has been obtained in the experiment carried out at lower beam energy

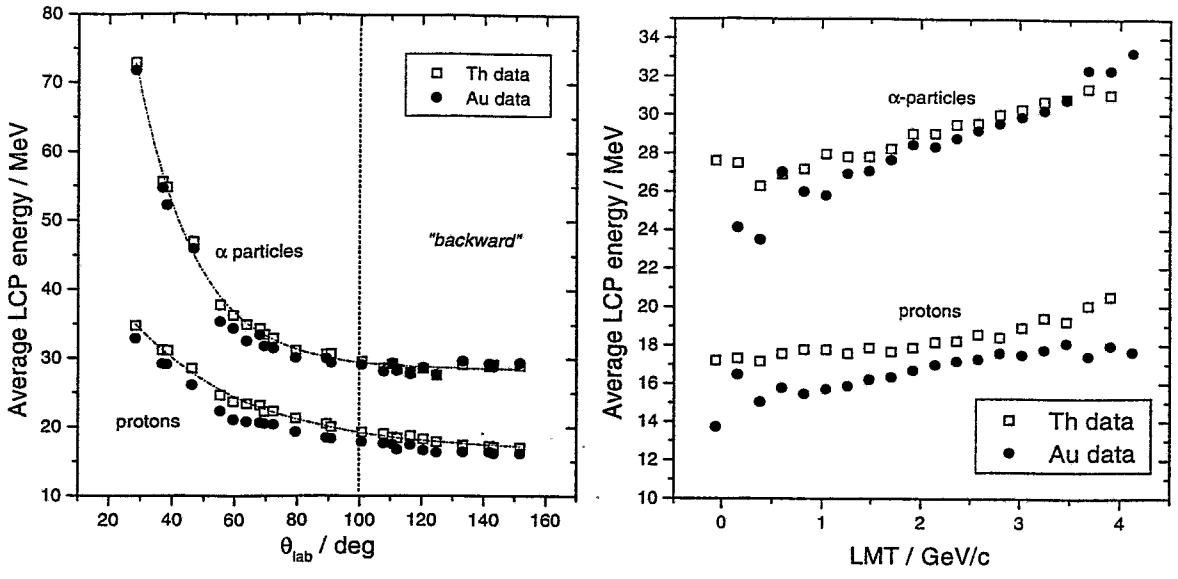

Figure 6.11: *Average energy of protons and α-particles as function of the angle of emission (left) and of LMT (right). The entire data of JAN96 experiments are used. Lines in the left frame represent fits for Th data by a function of type* $A\exp(-\theta^2/B)$.

6.2.1 Primary LCP data analysis

The gross properties of LCP emission are well know. Therefore, distributions of the average energy of a certain particle depending on the LMT and on the registration angle were created (fig. 6.11). As expected, average energies reveal a pronounced increase in forward direction because of projectile break-up and pre-equilibrium emission. The average energy of α-particles is constant at $\theta_{lab} > 100°$, whereas a slight decrease of the energy of protons towards the backward direction persists. The average energy of particles increases with increasing the LMT. This increase is usually related to the increasing excitation energy and, hence, to the nuclear temperature. Note, that energies of particles emitted from N+Th reaction are systematically larger than those from N+Au. This is due, on the average, to the larger charge of the emitter.

In addition to individual properties of LCPs a number of their collective properties could be analyzed. The set of LCPs observed in the CIS-shell in a certain event will is called, for the simplicity, the "CIS-event". Thus, the next important observation is presented in fig. 6.12 (left panel). A linear correlation of the total mass M and the total mass of LCPs is found, at least within the FWHM of the distribution of the total mass of the heavy fragments. This result proves the consistency of the data, because fragment masses and LCPs were measured by different detector shells.

The longitudinal V_Z and transverse V_X,V_Y velocity components of the center of mass of the CIS-event (i.e. total velocity) were determined event-by-event. The dependence of average total longitudinal velocity V_Z on LMT is shown in fig. 6.12 (right panel). Decreasing V_Z of the CIS-event (all curves) reflects the transition from peripheral to central collision. The same reason leads to slightly reduced V_Z values if only CIS-events with multiplicity $\nu_{LCP} > 2$ are chosen (triangles), because, on the average, higher multiplicity corresponds to more violent collisions. Therefore, events with $\nu_{LCP} > 2$ contain less

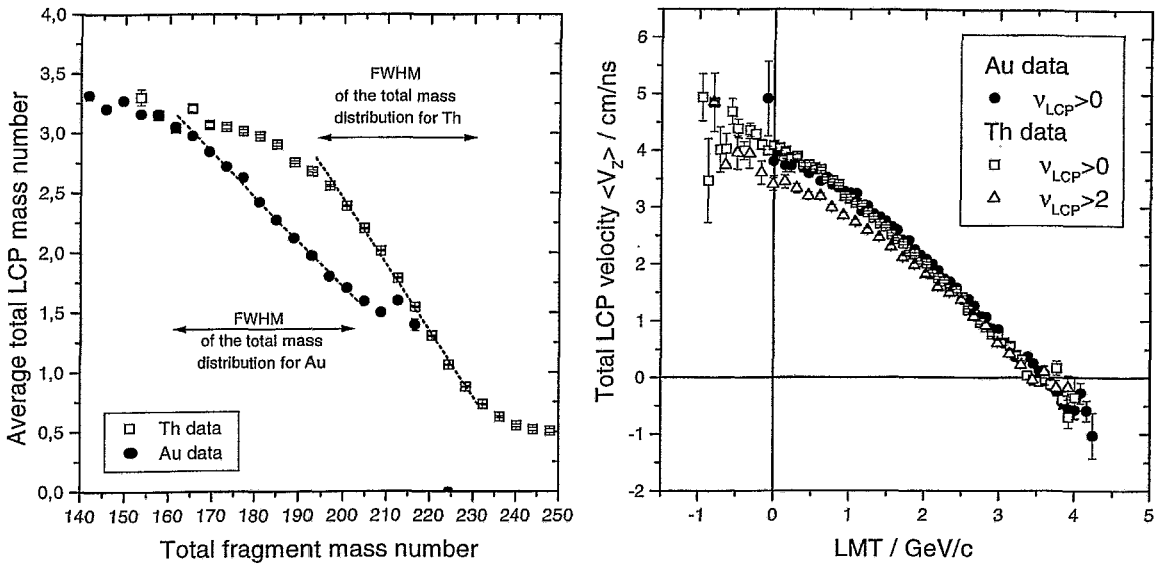

Figure 6.12: *Left panel: Correlation between the total mass of LCP and the total mass of the heavy fragments; widths of distributions of M are indicated. Right panel: Dependence of the average longitudinal velocity of a CIS-event on the LMT. See text for details.*

forwardly peaked pre-equilibrium particles, and this fact is observed as the reduction of V_Z.

The plots of the velocity components provide a good visual presentation of LCPs in the scintillator shell (fig. 6.13). The almost axially symmetrical appearence of the plot of transverse velocities as well as clearly observed structures (left panel) reflect the detector geometry. It has been seen, that the most probable observed number of LCPs in an event amounts to 0 or 1. Thus, easy recognizable "rays" in the velocity plots (both frames) correspond to the multiplicity $\nu_{LCP} = 1$, because counts are defined by discrete positions of CIS detectors and by the LCP energy. The five groups of rays in the V_x *vs* V_y plot correspond to five detector modules in the first modular ring. The notable asymmetry of the plot V_x *vs* V_z is due to the already mentioned sources of pre-equilibrium emission, which are known to be forwardly peaked. This plot also reveals a rather "isotropic" velocity distribution beyond $\theta_{lab} \approx 100°$.

The observed angular dependence of the pre-equilibrium emission agrees with results of simulations, given in Appendix D. These simulations predict that only at $\theta_{lab} > 100°$ one can study LCP evaporation from a composite system. Therefore, the limit of 100° is chosen to minimize the contribution of pre-equilibrium particles. Backward angles $\theta_{lab} > 160°$ are not accessible due to the FOBOS geometry. All available crystals under this condition cover the solid angle Ω_Σ=2.08 sr. This angular range will be further called the "backward hemisphere".

The LMT should depend directly on the impact parameter. The increase of LCP multiplicity with the LMT will be shown later. The classical picture of two colliding particles results in the following suggestion. As long as the target nucleus is not transparent for nucleons of a projectile the velocity distributions of the LCP event should change from the forwardly-elongated shape in peripheral collisions (low LMT) to rather isotropic shape in central collisions (high LMT). Moreover, multiple nucleon-nucleon scattering in a central

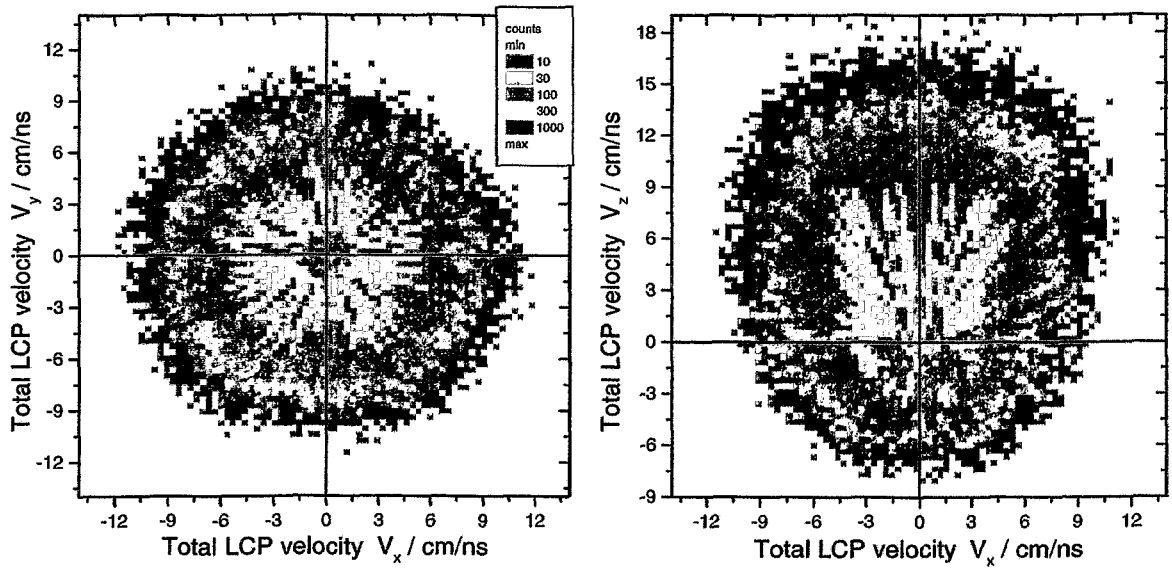

Figure 6.13: *Distributions of the velocity components of the LCP event ("total velocity") in the c.m. of the scissioning system orthogonal to the beam (left) and parallel to the beam (right). The entire data of JAN96 experiments are presented.*

collision could result in emission of fast particles into backward direction and the system should get additional momentum in the beam direction.

Indeed, the average longitudinal velocity of the LCP event in the center of mass of the scissioning system drops down even below zero reflecting the transition from peripheral to central collisions (fig. 6.12, right panel). The linear momentum smaller than zero acts as an additional momentum resulting in high longitudinal velocities of the composite system exceeding the velocity of a completely fused system. This also contributes to the peculiarity of the LMT distribution observed at high values of the latter as seen in fig. 6.10. In such a way, the contribution of pre-equilibrium particles into the backward hemisphere could turn out to be even larger than it was already expected.

6.2.2 ^{14}N 34 MeV/nucleon experiment

The spectra presented in fig. 6.14 are accumulated in one module of the backward hemisphere (Ring #6) and summed over 7 scintillators. Their PIMs of raw data were scaled to each other by means of a linear transformation following the idea proposed for the calibration procedure. The angle limits of integration are about $\pm 20°$ around the given values. The left and right plots are obtained from different detector modules.

The first spectrum (squares) contains α-particles coincident with the heavier fragment (HF) moving in the same direction as an α-particle. The second spectrum (circles) represents α-particles moving almost perpendicularly to the fission axis. Most particles of both spectra originate from the hot composite system, but the difference of these spectra (triangles) is consistent with the emission from a HF moving in the direction of the α-particle detector. In this case an "energy excess" occurs due to summing the velocities of the α-particle and of the emitter.

Estimates using such a subtraction procedure deliver yields of α-particles and, af-

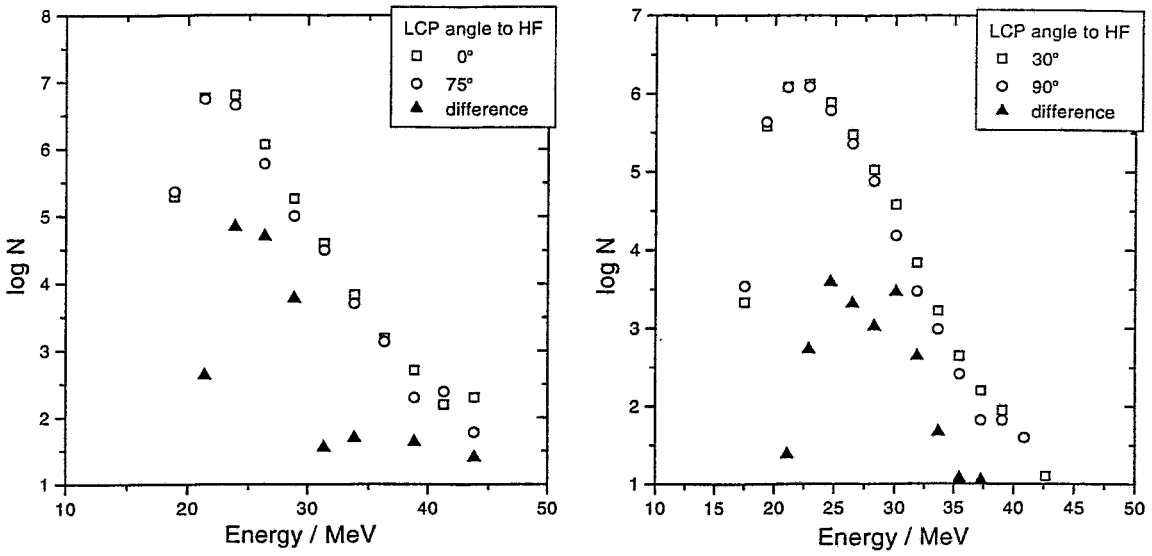

Figure 6.14: *Spectra of α-particles accumulated at different angles with respect to the heavy fission fragments (HF) from the reaction ^{14}N (34 AMeV) + ^{197}Au. The difference corresponds to an extra energy of particles emitted from the moving source. The energy calibration of these data is very rough due to technical reasons.*

Table 6.2: *Average α-particle multiplicities (yields per fission extrapolated to 4π). ν_{post} and ν_{pre} denote, respectively, pre-scission and post-scission multiplicities (i.e. LCP from the fragments).*

$< E^* >$	exp. data		from ref. [117]		calc. by CDSM
MeV	ν_{pre}	ν_{post}	ν_{pre}	ν_{post}	ν_{pre}
250	0.36(12)	0.09(4)	0.4	0.08	0.42

ter extrapolation to the whole sphere, one can compare them with data from literature (tab. 6.2). The good agreement with the data from ref. [117] testifies to the reliability of this simple method. The available calculations within the Combined Dynamical Statistical Model (CDSM) [118, 119] for the fission of the excited ^{205}Pb nucleus delivers the same pre-scission multiplicity at least for moderate angular momenta [120]. This agreement implicitly checks also the reliability of the performed extrapolation to the whole sphere.

6.2.3 Post-scission multiplicities at ^{14}N 53 MeV/nucleon

It has been proposed to separate pre- and post-scission particles as well as pre-equilibrium particles by the use of the multi-source fit method. This method required complicated software and numerical simulations, which were developed within the FOBOS collaboration by R.Yanez [5]. However, first attempts to apply the method to the present experimental data failed due to very high thresholds of the gas modules in a the flight path of LCPs. Distortions due to supporting grids and, first of all, due to smearing of the low-energy part of the spectra contributed additional difficulties. As long as the precise separation

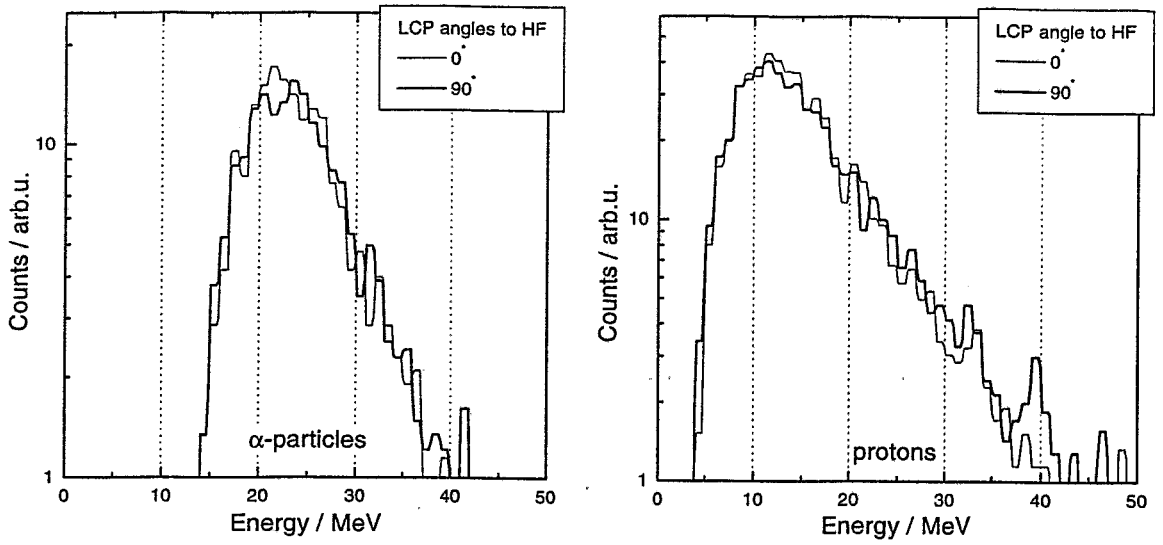

Figure 6.15: *Raw spectra of protons and α-particles accumulated in the backward hemisphere parallel or perpendicular to the direction of heavy fission fragments (HF) from the reaction* ^{14}N *(53 AMeV)* + ^{197}Au.

of emitting sources in the JAN96 experiment appeared to be impossible, the success of the simple approach described above nourished some hope, that one can apply the same method also to 53 AMeV data.

Spectra of LCPs are accumulated in coincidence with fission fragments in the backward hemisphere. In order to get the same solid angle for "parallel" and "perpendicular" directions to the fission axis, the "parallel" direction ($\psi = 0°$) to heavy fragments (HF) is chosen in the region $cos(\psi) \in [0.8; 1]$, and the "perpendicular" direction ($\psi = 90°$) means $cos(\psi) \in [-0.1; 0.1]$. The clearest result should be obtained for the symmetric case. Therefore, only events with the asymmetry $\beta < 1.5$ are considered. Unfortunately, no difference in these spectra are observed (fig. 6.15).

The lack of difference in proton spectra and, especially, in α-particle spectra may be due to the following reasons. First, a larger contribution of pre-equilibrium emission into the backward hemisphere compared to that for the 34 AMeV reaction. Second, different reaction mechanisms are involved. The 53 AMeV experiment could provide more reaction channels as that at 34 AMeV. Third, all particles are emitted from the composite system. The first idea seems to be reasonable, as it was already mentioned. The second reason will be illustrated in Section 6.3. The third reason can be checked by the method of the so-called "Galilean-invariant circles".

Galilean-invariant coordinates have been successfully applied to the source separation in LCP analyses [25, 121] and to IMF study as well [122, 121]. Similar to these papers Galilean-invariant coordinates were used in the analysis of LCP data from the JAN96 experiments (fig. 6.16). This method has the same physical ground as the "energy excess" method described above, and, hence, it has also some limitations because of thresholds.

In general, the two-dimensional picture, i.e. plots of longitudinal *vs* transverse velocities with respect to the scission axis in the rest frame of scissioning nucleus, should

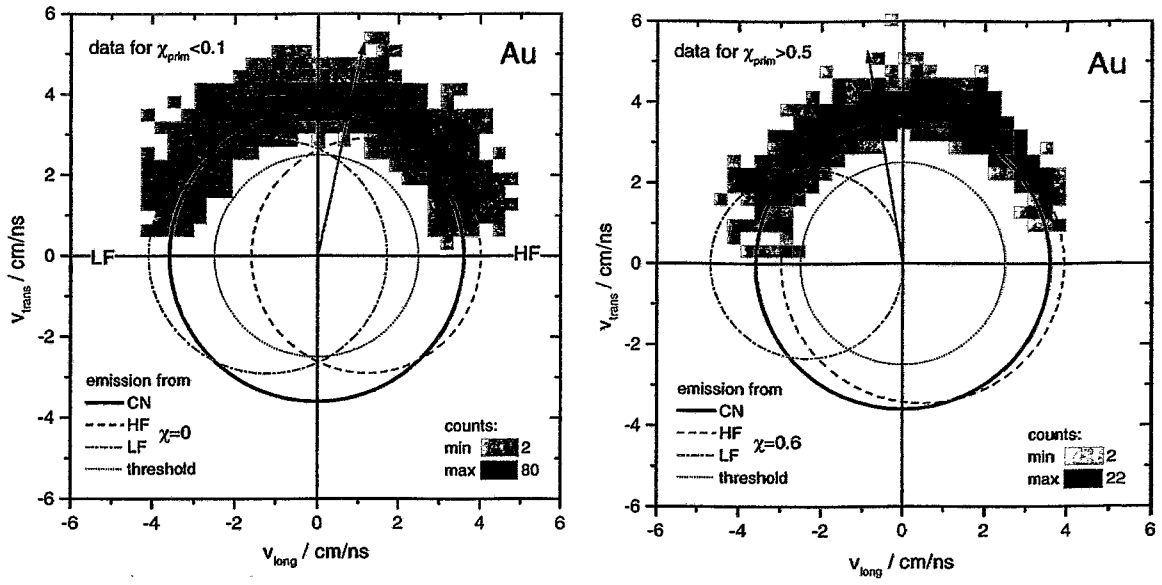

Figure 6.16: *Galilean-invariant velocity distributions for α-particles emitted in symmetric (left) and asymmetric (right) fission of Au. Lines are estimations: solid circles represent emission from the compound nucleus (CN), dashed and dot-dashed lines correspond to heavy (HF) and light (LF) fragments, respectively. The dotted line represents the detection thresholds imposed by the gas detectors. Arrows indicate the average direction of LCP emission.*

provide more detailed information than simple energy spectra[6]. Therefore, despite the threshold problem it was expected to observe some peculiarities in these plots related to the contribution of post-scission emission. In particular, these plots accumulated for different mass-asymmetry values should significantly differ from each other.

Transverse *vs* longitudinal velocity plots were studied under different coincidence conditions reflecting variations in mass-asymmetry, in initial excitation energy and in angular ranges of both LCP and FF detection. In contrast to expectations, besides of a tail found in the direction LF at $\chi\sim0.6$ in a high LMT bin (fig. 6.16, right panel), pronounced structures were neither observed in Th nor in Au data. This tail represents emission from the lighter fragment and accompanies the reduced dispersion in the direction HF, where Galilean-invariant circles from CN and HF almost coincide. In such a way, the character of the distribution differs from that for the symmetrical case (left panel).

The effect of the geometrical acceptance is also well seen in fig. 6.16. First, the acceptance in directions near the scission axis is significantly reduced. Second, the registration of LCPs only in the backward hemisphere affects the observed average direction of LCP emission. In the symmetrical case this direction should be perpendicular to the scission axis, but it is bent toward the heavier fragment. However, in the asymmetrical case it is bent towards the lighter fragment, reflecting the well known Coulomb focusing.

Despite the extraction of post-scission multiplicities appeared to be impossible, these observations argue in favor of the LCP data consistency. One should also note, that α-particles evaporated from a composite system seem to be not distorted by the threshold.

[6]Unfortunately, this reduces the number of counts per channel.

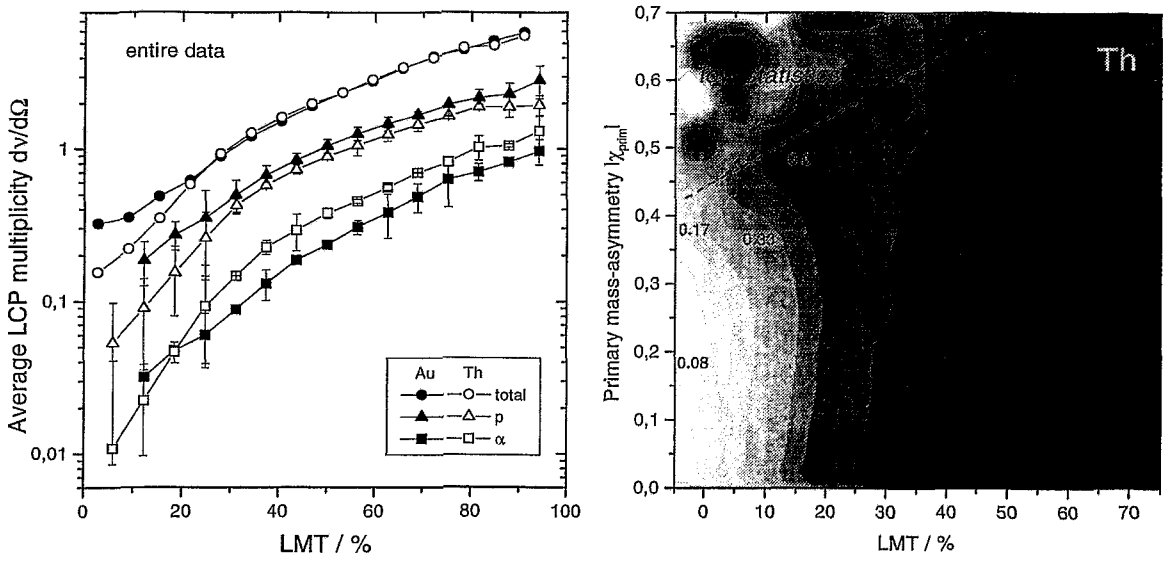

Figure 6.17: *Left panel: Multiplicities of LCPs, measured in the backward hemisphere in the JAN96 experiments. Right panel: The distribution plot of the average multiplicity depending on LMT and mass-asymmetry.*

6.2.4 Pre-scission multiplicities at ^{14}N 53 MeV/nucleon

The multiplicity of LCPs were obtained by means of extrapolation of the average values measured in the backward hemisphere to 4π sr (fig. 6.17). Most of these LCPs are presumed to be evaporated from an equilibrated composite system. It is then expected, that the multiplicity in the Au case should be higher than that in the Th case because Th data additionally contain results from peripheral collisions. This is, indeed, the case at low LMT. The difference in proton multiplicities is observed over the entire range of LMT. It is also correct, that multiplicities of α-particles are by an order of magnitude lower than multiplicities of protons. However, except for LMT<20%, multiplicities of α-particles from Th exceed those from Au. This could mean that there is an α-particle source behaving differently than the source of proton emission.

If the LCP multiplicity is related to the duration of the evaporation cascade, one might also consider a dependence of the LCP multiplicity on the mass-asymmetry. The right panel of fig. 6.17 represents the average LCP multiplicity for Th depending on LMT and on primary mass-asymmetry. It is obvious, that the multiplicity increases with increasing LMT in any mass-asymmetry bin. However, the trend at LMT<10% of the LCP multiplicity ν to increase slightly with increasing primary mass-asymmetry changes to the opposite at LMT>25%. Such a change together with the complicated profile of yields make questionable any one-dimensional analysis of the dependence $\nu(\chi)$, it indicates also that different processes may contribute to the entire data.

The major process at low LMT should be ordinary fission of Th-like nucleus at low excitation energy. Hence, particles observed in the backward hemisphere at low LMT should be mostly those evaporated from a compound system. Therefore, the increase in multiplicity with increasing mass-asymmetry at low LMT should indicate either a longer duration of ordinary asymmetrical fission as compared to a symmetrical one or higher

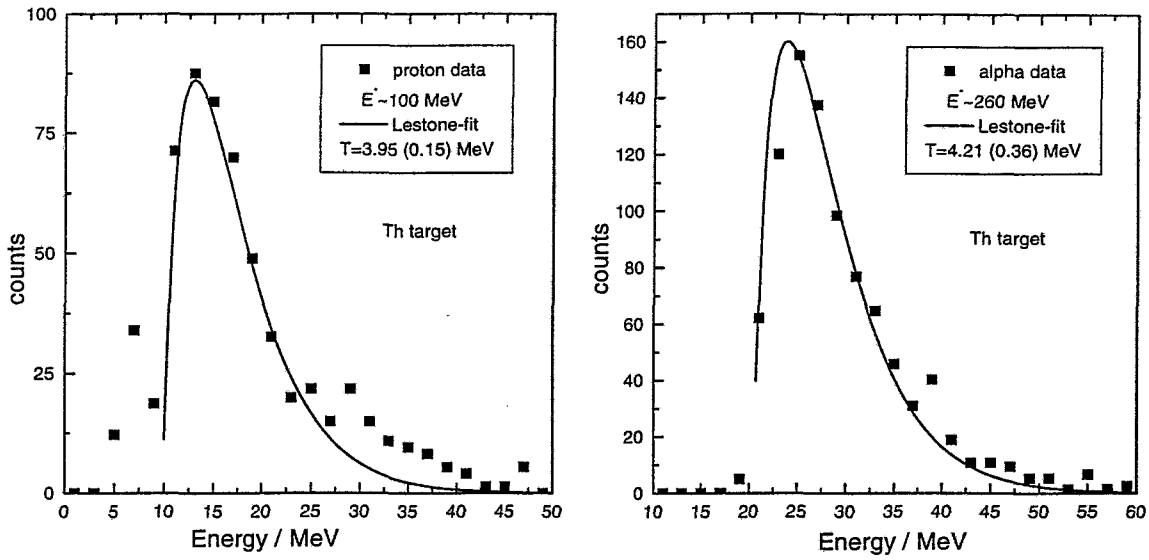

Figure 6.18: *Sample spectra of protons (left panel) and of helium (right panel) from the reaction ^{14}N (53 AMeV) + ^{232}Th for symmetric scission (symbols). Lines are the fits with the Lestone-type parametrization.*

excitation energy in asymmetric channel at the same LMT. The analysis of multiplicities at higher LMT definitely requires to separate the various reaction channels.

6.2.5 Slope parameter measurement

It is known, that the kinetic temperature is related to the nuclear temperature, but because of a number of reasons it should be treated very carefully [123]. A long evaporation chain results in an averaging over different reaction stages. One can also obtain non-physical temperatures by mixing different sources of particle emission. It should be noted, that the spectra measured in JAN96 experiments are not well suited for the study of the kinetic temperature. Such a measurement requires to fit the long tails of spectra at high energy. Spectra obtained at high LMT are likely to be contaminated with pre-equilibrium particles.

In order to avoid these difficulties a method sensitive to the position of the spectrum's maximum is used (Leston-type parametrization, Appendix C). The highest energy for the fit was limited in order to cut off the tail originating from a pre-equilibrium emission (see also Appendix D).

Spectra of protons and α-particles were accumulated in the backward hemisphere. The direction perpendicular to the scission axis was chosen in order to minimize the contribution of particles emitted from the fragments. The asymmetry window was set as $\chi < 0.2$. Two sample spectra are presented in fig. 6.18. Lines are the fits with the Lestone-type parametrization performed between the maximum position and the value of 25 MeV for protons and of 40 MeV for α-particles, respectively.

Resulting kinetic temperatures are plotted together in fig. 6.19. As it was expected, temperatures deduced from protons are lower than those from α-particle spectra. On the average, during a de-excitation chain protons have a chance to be evaporated later than

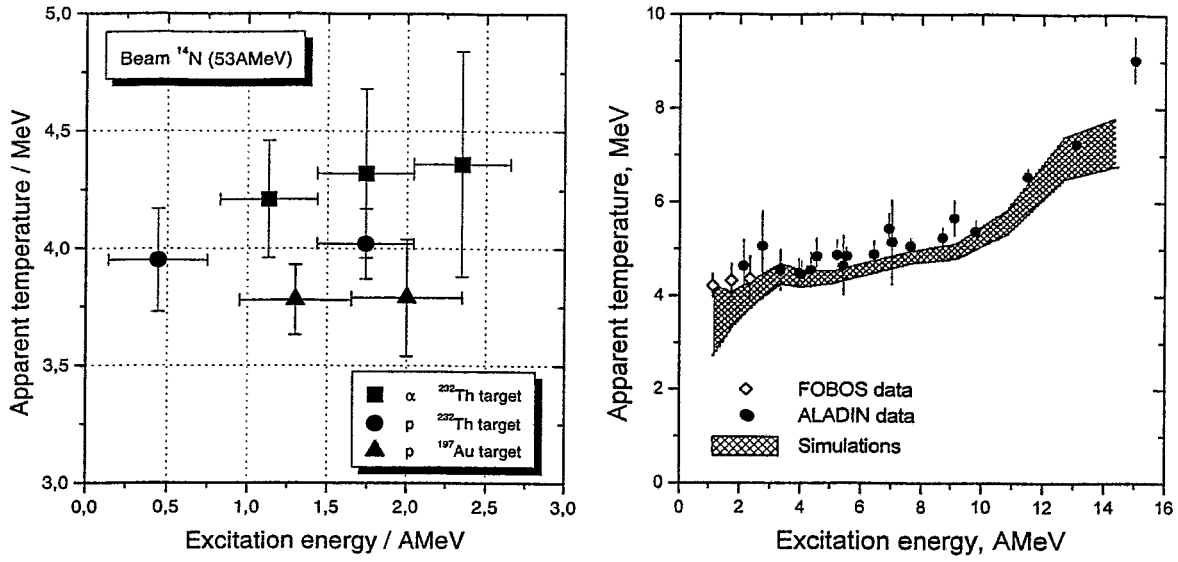

Figure 6.19: *Left panel: Kinetic temperature (slope parameters) obtained using a Lestone-type parametrization for the data measured with the projectile ^{14}N (53 AMeV) on ^{197}Au and on ^{232}Th targets. Horizontal bars indicate the integration interval. Temperature uncertainties are those from the fit. Right panel: Comparison of kinetic temperatures obtained from α-particles spectra with the ALADIN data. The picture is adopted from ref. [123].*

α-particles. Thus, the effective temperature for protons turns out to be lower because of cooling down with each act of LP emission.

Even if kinetic temperatures might not be too reliable because of method problems, two unexpected properties of their observed values should be noted. First, the expected nuclear temperature at the excitation energy of about 0.5 AMeV amounts to 2.5 MeV (Appendix D) and the kinetic temperature should not exceed the value of nuclear temperature. Second, no dependence on LMT, i.e. primary excitation energy, is found. Both of these observations indicate that the presumed channel of fission after incomplete fusion should be contaminated with other reaction processes even at low LMT. In turn, the reliability of LMT as a measure of excitation energy should be also questioned.

Although the determination of temperature and the interpretation of results are always model dependent, it is interesting to compare the derived kinetic temperatures with data from literature. The average apparent temperature observed by Wada et al. [124] in the reaction ^{63}Cu (35 AMeV) + ^{197}Au reveal the same saturation. Deduced values amounted to 4.5 MeV measured by a Li-He isotopic thermometer and to 4 MeV by a H-He thermometer. This agrees with temperatures of 4.2 MeV and 3.9 MeV for α-particles and protons, respectively, obtained from the FOBOS data.

The conclusion has been drawn in [124] that the derived temperatures show only a little variation with the excitation energy and that a limiting temperature may be reached at a relatively low excitation energy. It has also been stated that the apparent temperature of 4–5 MeV had been observed over a broad range of excited nuclei up to an initial excitation energy of about 10 AMeV in a number of recent experiments. Careful calculations made in ref. [123] reproduce measurements with different thermometers within a

standard evaporation formalism. An example of such calculations together with ALADIN data from ref. [125] is compared in fig. 6.19 (right panel) with the present FOBOS results.

Such a fairly good agreement of the 53 AMeV data measured by FOBOS with the ALADIN data from the reaction ^{197}Au (600 AMeV) + ^{197}Au leads to the conclusion that the contribution of already assumed *hot fragmentation* in JAN96 data is significant (see Section 2.4).

6.3 Exploring the mass-asymmetry

The primary and secondary asymmetries reveal, as it was shown in Sec. 6.1.2, some interesting features, which cannot be understood from their single spectra. From this point of view the idea to explore the correlation matrix of these asymmetries seems to be natural[7]. The application of such a correlation matrix turned out to be a powerful method for data interpretation. Therefore, a detailed description will be given in the following.

6.3.1 Definition of symbols

The basic reason for the difference between the primary and the secondary asymmetry is the distortion due to particle evaporation from the composite system as well as from the fragments, the latter is dependent on the sharing of excitation energy between the fragments. Although the mean velocity vectors do not change if the evaporation is isotropic, particle emission leads to a broadening of any distribution resulting from fluctuations of the excitation energy sharing.

The idea is illustrated in fig. 6.20 (left panel). The indices "1" and "2" denote the number of the fragment in a pair of FF. Up to now β and χ were specially defined to get always a positive value of the parameter χ and a value of β>1 (eq. 6.3). The generalization is needed, because the heavier primary fragment can become the lighter secondary one after post-scission emission. The definition of the asymmetry parameters is then given by

$$\beta_{sec} = A_1/A_2, \tag{6.7}$$

and

$$\chi_{sec} = \frac{A_1 - A_2}{A_1 + A_2}. \tag{6.8}$$

In such a way one gets secondary mass-asymmetries β_{sec} and χ_{sec} from the masses measured.

Although the masses $A_{i,prim}$ are not known, some parameters useful for the further discussion need to be defined, e.g. the mass removal from a fragment due to post-scission emission

$$\Delta_i = A_{i,prim} - A_{i,sec}, \tag{6.9}$$

and its relative amount is

$$\delta_i = \Delta_i/A_{i,prim}. \tag{6.10}$$

[7]Actually, this idea arose in search for a method to separate different sources of LCP and for a parametrization which reduces the number of uncertainties in the study of post-scission emission

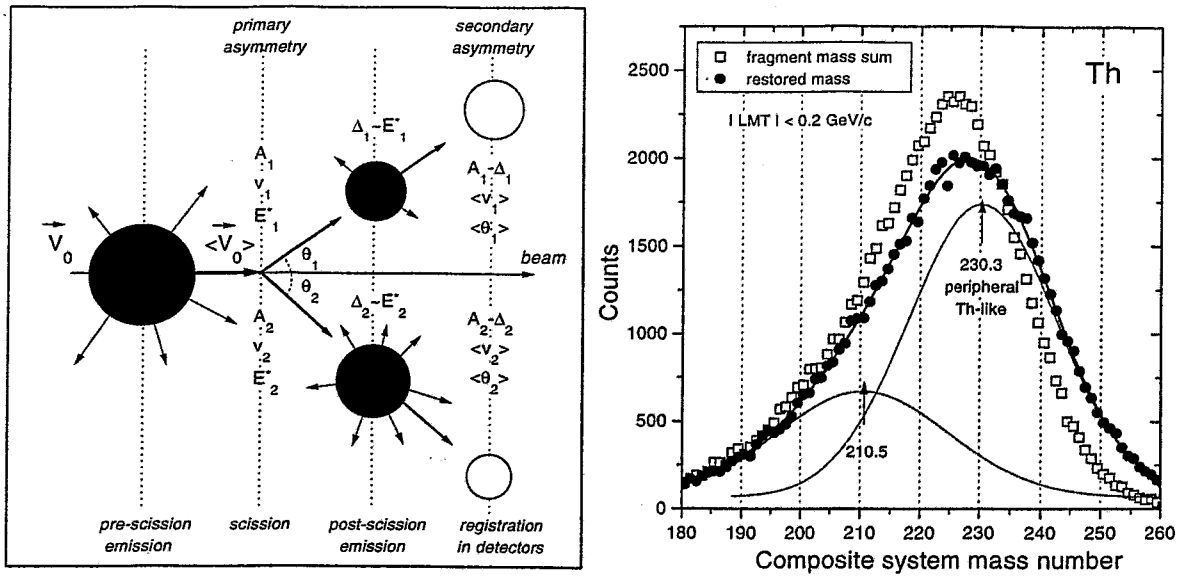

Figure 6.20: *Left panel: Illustration of the definition of primary and secondary asymmetry. Right panel: Spectra of the sum of fragment masses and the spectra corrected for the post-scission emission at low LMT for the ^{232}Th target. The peak corresponding to the fission of Th from the most peripheral collisions is clearly observed.*

For both primary and secondary asymmetries and masses the equation $A_1 = \beta A_2$ yields $M = A_2(1+\beta)$ where M denotes the total mass number of the fragments: $M = A_1 + A_2$. Substituting the dependence of β on χ, namely,

$$\beta = \frac{1+\chi}{1-\chi}, \tag{6.11}$$

and using eq. 6.9 one gets the mass of the system just before scission with the only non-measured quantity Δ_1 or Δ_2[8]:

$$M_{prim} = \frac{M_{sec}(1-\chi_{sec}) + 2\Delta_2}{1-\chi_{prim}}, \tag{6.12}$$

$$M_{prim} = \frac{M_{sec}(1+\chi_{sec}) + 2\Delta_1}{1+\chi_{prim}}. \tag{6.13}$$

The same can be written using the difference between Δ_i as

$$M_{prim}\chi_{prim} = M_{sec}\chi_{sec} + (\Delta_1 - \Delta_2). \tag{6.14}$$

A simple application of this procedure is the following. For the case of the low-energy fission of Th eq. 6.12 is considered for the lighter and heavier fragments. Setting Δ_L=0 one gets an estimate for the mass of the composite system. The spectra of the total fragment mass as well as of the mass of the composite system restored in such a way are accumulated within narrow bin around LMT=0. Since fission of nearly cold ^{232}Th

[8]Most of the light particles emitted from the fragments are neutrons, therefore, Δ_i is nearly equal to the corresponding neutron multiplicity.

is selected in such a manner, the hypothesis Δ_L=0 should not be far away from its real mean value, especially for an asymmetric split. The latter means, that the calculated M_{prim} should represent the lower limit for the system mass. As one can see from fig. 6.20 (right panel), the restored distribution is slightly shifted when accounting for post-scission evaporation. The restored distribution can be approximated with two Gaussians, meaning that it consists of the dominating contribution of fission of nearly cold Th-like nuclei and some contribution from other reaction channels.

Indeed, the peripheral peak at the mass number of 230±1 is observed together with a smaller one at about 211. According to ref. [126] the pre-scission neutron multiplicity for ^{232}Th amounts to 2–4. Hence, one gets 233 ± 3, which is a rather good estimation for the mass of the fissioning Th nucleus. However, some imperfection of this mass reconstruction is obvious — the yield of total masses above the initial total mass of 246 amu becomes larger with respect to the measured spectrum. Probably, the transverse velocity of the compound-like system should be taken into account in the calculation of χ_{prim} for a more advanced analysis. The impact of transverse velocity on χ_{prim} should be larger at low LMT. Also the contribution of processes other than *ordinary fission* should be studied.

In order to get a quantitative measure for the difference between primary and secondary asymmetries, the parameter $\bar{\zeta}$ can be introduced:

$$\bar{\zeta} = \beta_{sec}/\beta_{prim}. \tag{6.15}$$

The values Δ_i reflect the multiplicity of particles evaporated from the fragment "i", and therefore Δ_i can be used as a measure of the excitation energy deposited in the fragment "i". Then $\delta_i = \Delta_i/A_i$ is a measure of the excitation energy per nucleon in the fragment "i". Equilibrium sharing of the excitation energy between the fragments supposes $E_i^* \sim A_i$, then, on the average, equilibrium sharing of the excitation energy leads to the conservation of the asymmetry ($\chi_{prim} \approx \chi_{sec}$) because of $\delta_1 \approx \delta_2$. Therefore, the parameter $\bar{\zeta}$ defined by eq. 6.15 is close to unity only in the case of thermodynamical equilibrium.

Substituting eqs. 6.7 and 6.9 into eq. 6.15 one gets

$$\bar{\zeta} = \frac{1-\delta_1}{1-\delta_2}. \tag{6.16}$$

The latter expression can be written as

$$\bar{\zeta} \approx \frac{1-\nu_1\epsilon_1^*}{1-\nu_2\epsilon_2^*}, \tag{6.17}$$

where ϵ_i^* is the excitation energy per nucleon, and ν_i is the average multiplicity of particles per 1 MeV of the excitation energy.

In such a way, the formally introduced parameter $\bar{\zeta}$ may be called "the excitation energy sharing parameter" [9]. It is model-independent, dimensionless and can be extracted directly from experimental data. In this sense the parameter $\bar{\zeta}$ can be treated as an additional physical observable.

As it follows from eq. 6.16 the proposed ζ-parametrization is, of course, not perfect for a study of the excitation energy sharing. If, for instance, one changes both δ_1 and

[9]The excitation energy sharing parameter will be re-defined by eq. 6.20

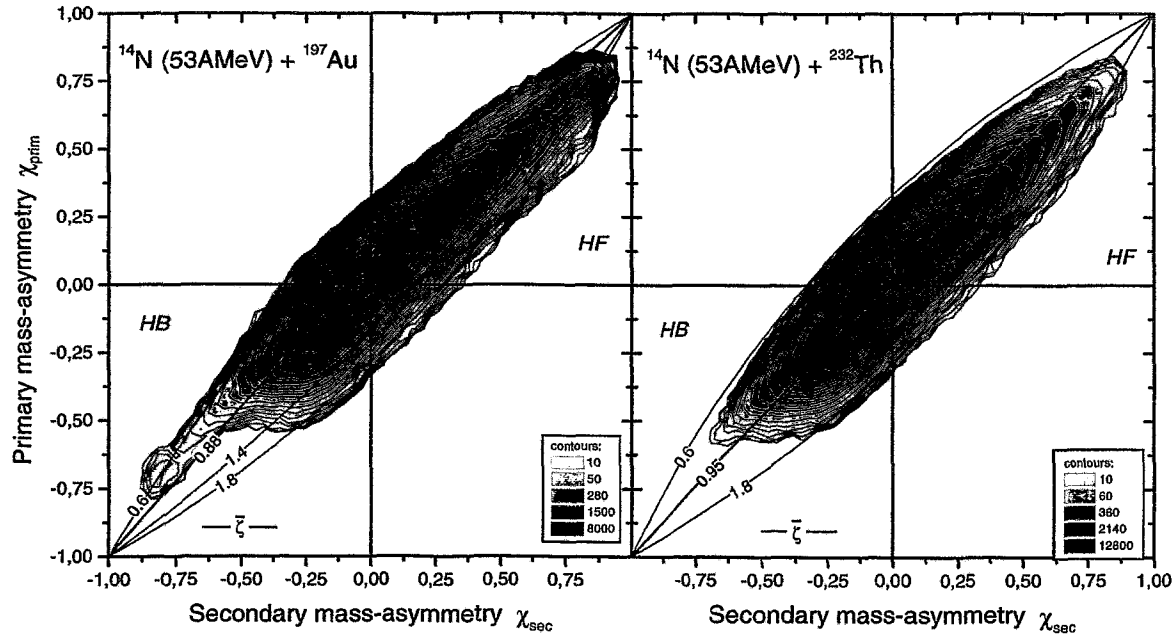

Figure 6.21: *Mass-asymmetry matrices for the reactions of the JAN96 experiment. Lines of an equal excitation energy sharing parameter $\bar{\zeta}$ are marked with its values. The quadrant marked as "HB" represents mostly data, where the heavier fragment was directed backwards; "HF" means that the heavier fragment was directed forwardly. See also fig. 6.22.*

δ_2 proportionally, the same degree of equilibration is maintained, however, the value of the parameter $\bar{\zeta}$ would change. Interchanging of fragment "1" and "2" also leads to a change of each value to $1/\bar{\zeta}$, which is inconvenient for an analysis of $\bar{\zeta}$-spectra. These inconveniences will be corrected later in order not to loose the physical meaning of parameters by transformations of coordinates.

In addition, the direct application of this parameter in an event-by-event analysis is also not correct, because the primary asymmetry delivers reliable information only on the average. Despite the mentioned difficulties, the $\bar{\zeta}$-parametrization delivers a powerful method of data interpretation which will be exploited in the following.

6.3.2 The mass-asymmetry matrix

Mass-asymmetry matrices for the data from both the JAN96 experiments are presented in fig. 6.21. Two statistically reliable structures are observed. Both matrices for Th and Au contain a bump near the equilibrium value of the excitation sharing parameter $\bar{\zeta}$. A second structure is represented by peaks at $\bar{\zeta} \approx 0.6$ and $\bar{\zeta} \approx 1.4$ for the most asymmetric mass splits in the matrix for Au . The weak tendency of the deviation of $\bar{\zeta}$ from equilibrium with increasing mass-asymmetry could be found also in the Th-matrix.

The interpretation of the mass-asymmetry matrix is facilitated by fig. 6.22 (left panel). The structure of the matrix is of central symmetry around the point $\chi_{prim} = \chi_{sec} = 0$ for such decays where no difference between the fragment "1" and "2" is presumed. This is actually not the case, because the numbering of the fragments in the raw data usually corresponds to their laboratory angle. Therefore, the fragment "1" is usually

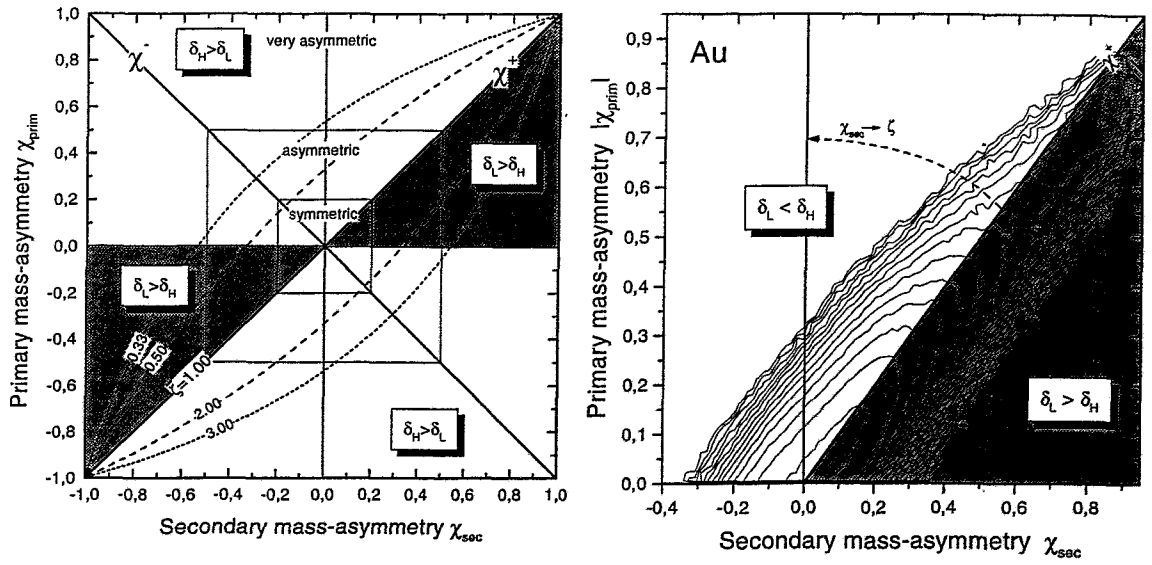

Figure 6.22: *Illustration of the information contained in the mass-asymmetry matrix (left panel) and its further transformation (right panel). The mass-asymmetry matrix is, by definition, symmetrical with respect to the center (left) and, therefore, the lower part is rotated by 180° (right).*

directed forwardly with respect to the beam axis in the center-of-mass system. This means that the mass-asymmetry matrix could be non-symmetrically populated because of the certain choice of the fragment numbering. In addition, mass-asymmetrical pairs of the fragments could significantly differ in the registration efficiency depending on the direction of the heavier fragment. Thus, the asymmetry matrix does not symmetrically extend into positive and negative directions of χ^+ ; this is most clearly seen in the Th data as a cut-off at $\chi_{prim} \approx 0.55$ (fig. 6.21, right panel).

The mass-asymmetry matrix is stretched along one of the diagonals and shows some symmetry with respect to the other one. Both diagonals have special meanings. Points located at the positive diagonal $\chi_{prim} = \chi_{sec} = \chi^+$ correspond to the equilibrium case. The ratio between mass removals from the fragments can be written as

$$\frac{\Delta_1}{\Delta_2} = \frac{1+\chi^+}{1-\chi^+}. \tag{6.18}$$

Besides of the increase of "non-equilibrium" along the negative diagonal $\chi^{prim} = -\chi^{sec} = \chi^-$, for given primary and secondary masses one can write the simple difference

$$\Delta_1 - \Delta_2 = \chi^-(M^{pre} + M^{post}) \tag{6.19}$$

Removing one α-particle from one of the fragments should result in the appearance of some structure in the mass-asymmetry matrix at $\chi^- \approx 0.01$ parallel to the χ^+ diagonal. This line is characterized by the value of $\bar{\zeta} = 0.95$, and it runs exactly through the peak in the Th-matrix.

The region $\chi_{prim} > 0$ above the χ^+ axis contains those events, where the evaporation from the heavier fragment is more intensive, relative to the fragment mass, than from the

lighter one ($\delta_H > \delta_L$). The situation is reversed ($\delta_L > \delta_H$) below the χ^+ axis (see fig. 6.22). This area can also host a situation, when the lighter fragment receives more excitation energy than the heavier one on an absolute scale.

Summarizing, one can conclude that the asymmetry matrix should be really transformed into a matrix of a type like χ^+ *vs* χ^-. The primary mass-asymmetry is more interesting for the further analysis, because it is directly related to the instant of scission. From the point of view of formal logic, there is no difference between $+\chi_{prim}$ and $-\chi_{prim}$. Therefore the lower part of the mass-asymmetry matrix is rotated by 180° around zero (fig. 6.22, right panel). Hence, values of χ_{prim} will be always positive — such a transformation will be further indicated by $|\chi_{prim}|$. In such a way, relation $\delta_L > \delta_H$ means $\bar{\zeta} > 1$ and vice versa.

An inconvenience of $\bar{\zeta}$-spectra analysis noted in the previous section can be corrected introducing the derivative parameter

$$\zeta = (\bar{\zeta} - 1)/(\bar{\zeta} + 1), \tag{6.20}$$

as it was done for the mass-asymmetry parameter χ. Equilibrium is then represented by $\zeta = 0$. The definition of eq. 6.20 will be further assumed when using the term "excitation energy sharing parameter".

This simple transformation of $\bar{\zeta}$ into ζ provides also some simple physical meaning of the excitation sharing parameter. Indeed, the relationship between the excitation energy E^*, the mass A and the temperature T ("the caloric curve") was found to obey the Fermi gas law. The formula

$$E^* = aT^2 \tag{6.21}$$

should be reliable up to $\epsilon^* = E^*/A \approx 6 - 7\ AMeV$ with the constant level density parameter a, typically in the range from $A/13$ to $A/8$ MeV^{-1} [127]. Let $\lambda = a/A$, then it follows from eq. 6.17 that

$$\bar{\zeta} \approx \frac{1 - \nu_1\lambda_1 T_1^2}{1 - \nu_2\lambda_2 T_2^2}. \tag{6.22}$$

Because of $\lambda_i \sim 10^{-1}$ as well as $\nu_i \sim 10^{-1}$ by order of magnitude, one gets from eq. 6.20

$$\zeta \approx \frac{1}{2}(\nu_2\lambda_2 T_2^2 - \nu_1\lambda_1 T_1^2). \tag{6.23}$$

Setting for the most symmetric splits $\nu_1 \approx \nu_2$ and $\lambda_1 \approx \lambda_2$, one gets a rough expression, which qualitatively reflects the meaning of the parameter ζ

$$\zeta \sim T_2^2 - T_1^2. \tag{6.24}$$

Hence, the further transformation of the mass-asymmetry matrix shown in fig. 6.22 should be the matrix of $|\chi_{prim}|$ *vs* ζ. Positive values of ζ represent higher temperature of the lighter fragment, and negative values of ζ indicate higher temperature of the heavier fragment. Such a matrix will be called further "ζ-χ matrix"[10].

6.3.3 The TKE factor R_χ

Notable success in the FOBOS data processing at lower beam energies is achieved using the LMT for the excitation energy calculation. However, difficulties of the conventional data analysis concluded in Section 6.1.3 require to introduce some additional parameters.

[10] An example of the "ζ-χ matrix will be given in fig. 6.29.

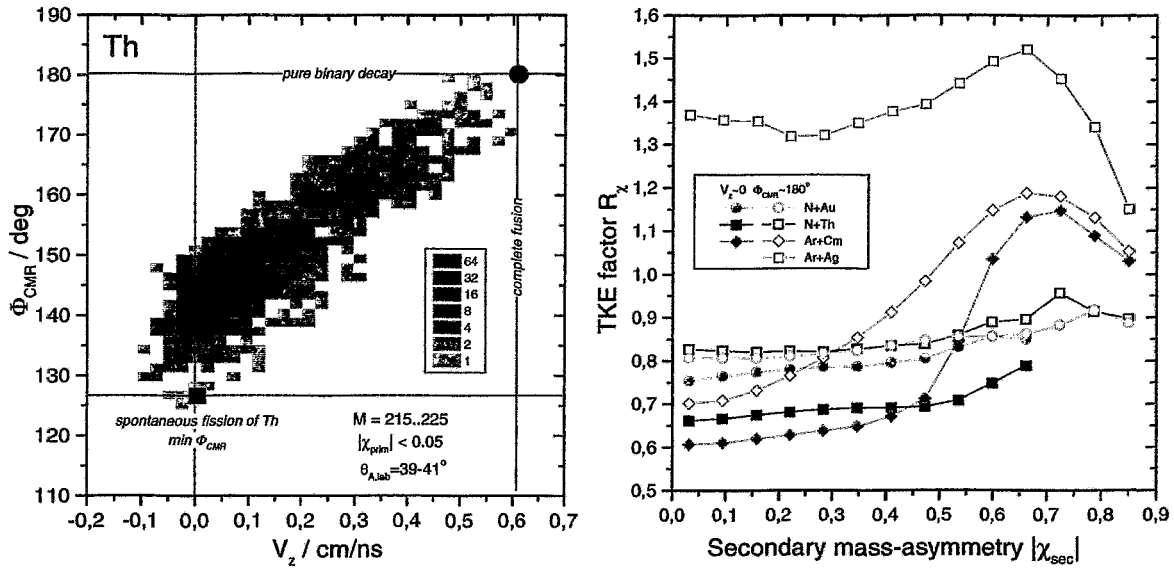

Figure 6.23: *Left panel: Folding angle in the CMR vs c.m. velocity component parallel to the beam for Th data accumulated under the indicated conditions. Right panel: Dependence of the average TKE factor R_χ on the mass-asymmetry accumulated for the very low c.m. velocities V_z (solid symbols) and for the highest CMR folding angle (open symbols). Errors of averaging are smaller than a symbol size.*

The first problem concerns the possibility to separate a certain reaction channel by means of a cut in ordinary parameters. Setting the total mass to be around the "peripheral peak" as $M \in [215, 225]$ u in the most mass-symmetric bin of $|\chi_{prim}| < 0.05$, one considers the matrix (fig. 6.23, left panel) of longitudinal velocity V_z *vs* Φ_{CMR}. The folding angle Φ_{CMR} is calculated in the center of mass of the reaction (CMR). This folding angle is 180° only if the projectile has completely fused with the target, otherwise it is always smaller than 180°. The folding angle is dependent on the observation angle, and hence, as an example, the distribution for the very narrow angular range of $\theta_{A,lab} = 40 \pm 1°$ is represented in the left frame of fig. 6.23. As it is expected the peak is located at small velocity and small folding angle values. However, in spite of rigid constrains, points populate the broad band between the point of compound-like system (circle) and cold fission with the lowest possible folding angle Φ_{CMR} (square). This means that the studied mass-symmetric peak at M=221 u could originate from completely different reaction mechanisms, and an analysis such as presented in Section 6.1.3 is too simplified. Therefore, Φ_{CMR} is also used as an auxiliary parameter.

The next problem concerns the interaction mechanism and the calculation of the excitation energy. In the limiting case of no interaction between a target and a projectile, the LMT and V_z calculated from the sum of the participants' linear momenta would be 100% for the given reaction, the same it true for the total mass. In this case a high LMT does not imply excitation of the system. Therefore, special attention should be paid to the relative fragment-velocities which could keep memory about the initial projectile velocity. However, the relative velocity of fission fragments depends on the mass-asymmetry.

As long as the fission systematic of TKE is well known, one could use TKE. For comparison of TKE for asymmetric and symmetric fragment pairs, one should correct the

measured TKE by a mass-asymmetry dependent factor. The most simple way, probably, consists in using the already mentioned extended TKE-formula eq. 6.6. Setting $Z = A_{tot}/2$ one gets

$$E_W = 0.073 \frac{A_1 A_2}{A_1^{1/3} + A_2^{1/3} - A_{tot}^{1/3}}. \tag{6.25}$$

The following simple ratio is found to be useful for the analysis:

$$R_\chi = TKE/E_W, \tag{6.26}$$

which will be called further the "TKE factor R_χ". The charge of the heavy system is definitely lower than $A_{tot}/2$, therefore R_χ should be below unity. Nevertheless, this rough approximation is sufficient for the qualitative comparison between symmetric and asymmetric decays of similar systems.

Note, that R_χ is not dependent directly on the total mass A_{tot}. Therefore, it is reasonable to use this parameter for exploring the time scale of a reaction. Indeed, it is known that during the evaporation cascade neutrons are emitted much more frequently than charged particles. Thus the ratio Z/A, and, hence, TKE as well as R_χ increase. Therefore, a cooled down system should differ from the system which has lost nucleons by any kind of direct emission. Thus, this "TKE factor" consists of two independent parts

$$R_\chi = R_\chi(v_{PLF}) + R_\chi(Z/A), \tag{6.27}$$

where v_{PLF} marks the part depending on the residual projectile velocity and Z/A points to the dependence on the isotopic composition.

To give an example, mean values of R_χ were accumulated in dependence on the mass-asymmetry for the entire data (fig. 6.23, right panel). These values are found to be nearly constant in the wide range of χ_{sec} for Th and Au data. A small increase in the slope is observed at mass-asymmetries larger than 0.5. Bumps of R_χ are observed at large mass-asymmetries in Ag and Cm data, where the formation of PLF-TLF pairs is assumed. Qualitatively, values of R_χ for most symmetric splits appeared to be ordered according to their usual isotopic composition in each of both the "compound-like" group ($\Phi_{CMR} \approx 180°$) and the "peripheral-like" group ($V_z \approx 0$). Values of R_χ for "compound-like" systems are systematically higher than for "peripheral-like" ones. For mass-symmetric splits it could generally mean different values of the ratio Z/A, e.g. cooling down occurs. Concerning mass-asymmetric splits, the systematically observed increase in R_χ should be a hint that semi-peripheral interactions could contribute to any of the studied reactions. Thus, angular dependencies should be considered in spite of complications because of acceptance effects.

6.3.4 Experiment with ^{40}Ar (36 AMeV) beam

Data from the MARCH97[11] experiments provide a good check for the ζ-parametrization and deliver a useful information, which is applied for exploring JAN96 data. For instance, asymmetry and ζ distributions for the Ag data can be used as a qualitative time "calibration" reference for a short time scale [12], so far as only a small contribution of fission for Ag is presumed.

[11] See Section 2.5 for the experiment designation.

[12] The low-energy (ordinary) fission of Th-like nuclei is used in the same manner as an ethalone for a slow process.

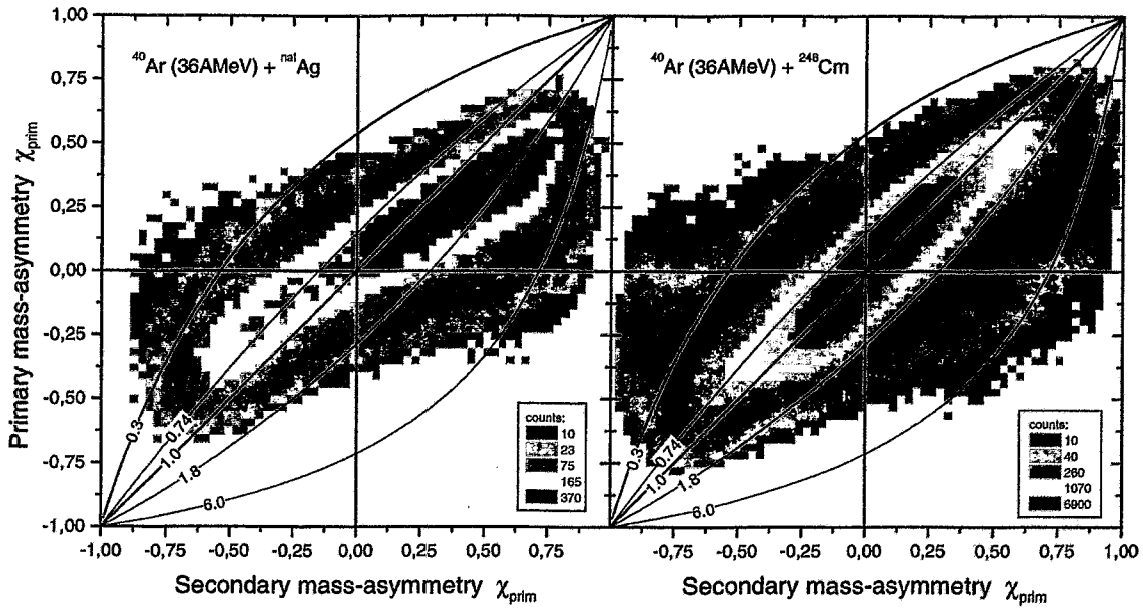

Figure 6.24: *Entire mass-asymmetry matrixes for the experiment MARCH97. Lines represent different $\bar{\zeta}$-values. The full-range matrix is shown in order to check the acceptance effect – these matricies were expected to be more symmetric than those for Au and Th.*

Two statistically reliable structures are observed in mass-asymmetry matrices for the entire data (fig. 6.24). The matrix for Cm contains a bump near equilibrium of the excitation energy sharing. It is associated with the fission of Cm-like nuclei after peripheral collisions. This region is less populated in Ag data. Its matrix is peaked at $\bar{\zeta} = 1.8$. Most of the Ag data and this peak itself are located in the area where the temperature of the lighter fragment should be higher than the temperature of the heavier fragment. Such sharing of the excitation energy has been concluded to be essential for the PLF-TLF formation in refs. [128, 129]. The contribution of the PLF-TLF formation process is present also in the Cm-matrix at $\bar{\zeta} \approx 1.8$, although it is almost covered by the ridge of events with $\bar{\zeta} = 1.0$. The asymmetry of this structure in both of matrices reflects the fact, that data of dynamical decay, where forward and backward directions are essentially different, are modified by the detector acceptance differently. The asymmetry matrix for Cm is dominated by equilibrated decays, which symmetrically populate the positive diagonal of the matrix. The broader distribution for Cm is conditioned mainly by the significantly larger number of events accumulated. Generally, as it was expected, the matrices for Ag and Cm are more symmetric than those for Au and Th because of a more symmetrical entrance channel and, therefore, more symmetrical distribution of fragment masses.

Data from the reaction ^{40}Ar (36 AMeV) + ^{nat}Ag are difficult to analyse because of the large mass and linear momentum carried away by fast LCP and projectile residuals. However, only this reaction (among available data from JAN96 and MARCH97 experiments) can deliver heavy fragments which can be clearly assigned to a well defined reaction channel. Hence, reasonable assumptions concerning the relative duration of the reaction could be put forward. Cm data are even more complicated because of additional reaction mechanisms.

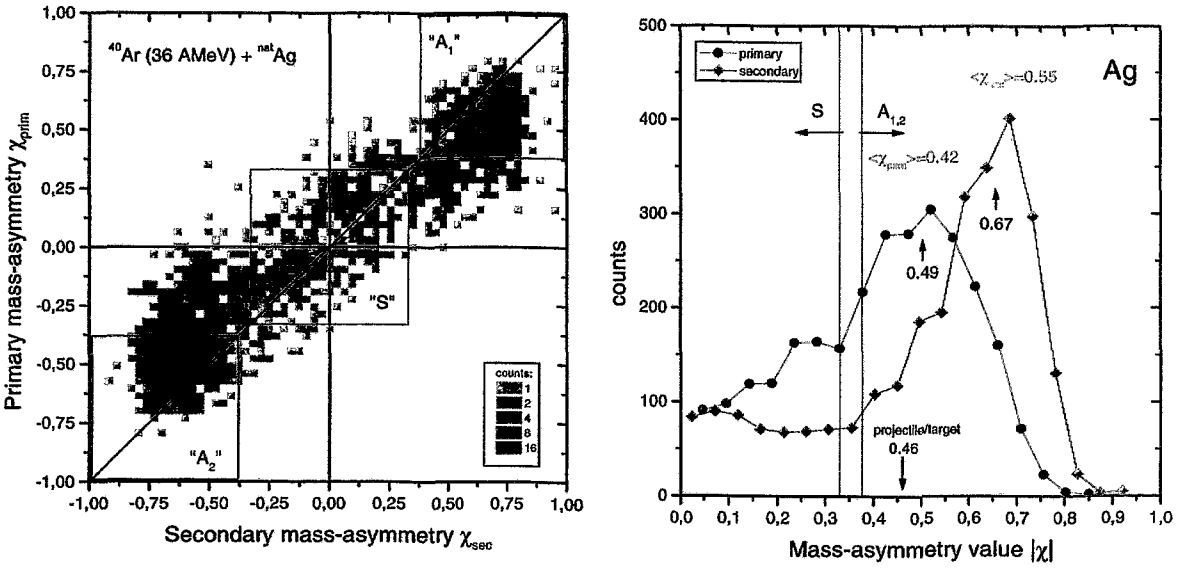

Figure 6.25: *Left panel: Mass-asymmetry matrix for Ag data for "almost binary" events. Boxes indicate the choice of symmetric "S" and asymmetric "$A_{1,2}$" splits. Right panel: Spectra of primary and secondary mass-asymmetries for "almost binary" events.*

In order to separate clearly the decay of the composite system into PLF and TLF, the following conditions were set. 1) The total mass was constrained between 108 and 148 amu, e.g. between masses of the target nucleus and the initial total mass of the system. 2) The missing linear momentum was limited by means of cut of the folding angle Φ_{CMR} >110°. Such constrains select "almost binary" events; however, this leads to the drastical reduction of the data (few percent of the entire data bulk). 3) Most of events defined by these conditions are distributed between LMT values of 3 and 6 GeV/c (fig. 6.26). Events with LMT out of this region were also rejected from the analysis. 4) In the same manner the longitudinal velocity V_z was constrained between 0.9 and 1.9 cm/ns.

The mass-asymmetry matrix filtered in such a way reveals two components – two oppositely located asymmetric peaks and the broad symmetric component (fig. 6.25). The mean peak values of the asymmetric component are found at $|\chi_{prim}| = 0.49$ and $|\chi_{sec}| = 0.67$. This difference indicates a substantial evaporation of nucleons from the PLF. The mean peak position of the primary asymmetry is located near the initial target/projectile asymmetry value of 0.46. This implicitly proves the calculation of χ_{prim}. The asymmetric component should represent peripheral collisions where the interaction time reflects only a short touching of the nuclei. This component reveals a sharp peak in the distribution of the scission angle at $\theta_A = 50°$ (angle between scission axis and beam direction). One should expect high relative velocities of fragments, because the beam velocity in very peripheral collisions is not damped and the reaction proceeds on a short time scale.

On the contrary, a certain time is needed to create a mass-symmetric distribution from a mass-asymmetric entrance channel. This, probably, occurs in central collisions. In such a case the excited composite system intensively evaporates nucleons, and if this proceeds long enough, the number of lost nucleons should be considerable. On the other hand side, one should expect less pre-equilibrium particles emitted with beam-like velocities compared to the asymmetric case. This difference in pre-equilibrium particles could be

Table 6.3: *Comparison of symmetric ("S") and asymmetric splits ("$A_{1,2}$") for the "almost binary" events for Ag data (average values). Typical uncertainties are of about 2% for symmetric and 1% for asymmetric splits, respectively.*

parameter	M / amu	$\|\zeta\|$	V_z / cm/ns	TKE / MeV	R_χ
symmetric	115	0.12	1.45	107	1.23
asymmetric	119	0.21	1.18	105	1.73

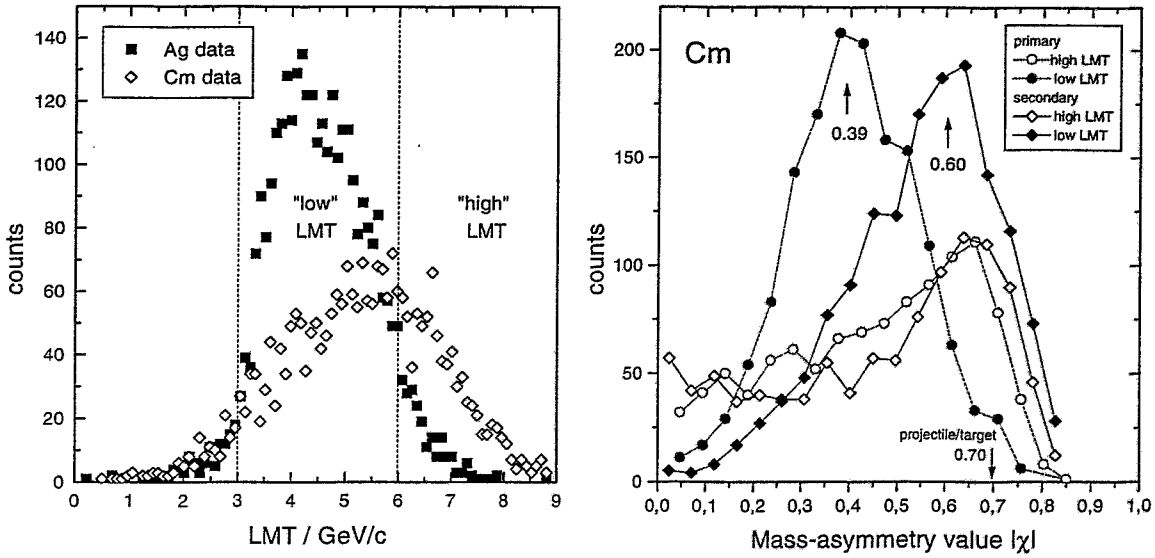

Figure 6.26: *Left panel: The division of LMT spectrum for Cm into "low" and "high" parts for the "almost binary" events. The spectrum of LMT for Ag is shown for comparison. Right panel: Spectra of primary and secondary mass-asymmetries for Cm for these LMT bins.*

observed in the higher velocity V_z in the symmetric case. These pre-equilibrium particles reduce the excitation energy of the system in the asymmetric case thus reducing also the expected difference in the evaporated mass. Excitation energy sharing is expected to be equilibrated in a slow process. Therefore, the parameter ζ should somehow distinguish between the symmetric and asymmetric splits for Ag.

Indeed, an excess of the total mass for asymmetric splits is found (tab. 6.3). As it was supposed, significant difference in the excitation energy sharing and V_z velocity occur. The TKE turned out to be nearly equal. This happens because of the mass- and, therefore, the charge-symmetry lead to the reduction of the TKE, whereas a rest of the projectile velocity contributes to the TKE. On the contrary to TKE, R_χ reveals this additional velocity in asymmetric splits.

In order to check such a well pronounced manifestation of PLF-TLF formation in a mass-asymmetry analysis, Cm data were analyzed in the same manner as Ag. Constrains were set to the total mass as $A_{tot}/\mathrm{u} \in [248, 288]$ and to the folding angle as $\Phi_{CMR} \in [145°, 180°]$. The peak is observed in the distribution of scission angle at $\theta_A = 45°$. The mass-asymmetry spectra in the same LMT box as for Ag data reveal also that the PLFs

are hot enough to evaporate a significant number of nucleons, i.e. $T_{PLF} > T_{TLF}$ (fig. 6.26). Note, that the mean peak value of the primary asymmetry is found well below the initial asymmetry of 0.70 (compare with Ag). This could indicate either a knock-out of target matter or its flow to the PLF during the interaction, or, probably, both processes are present[13]. These events should be classified as semi-peripheral because no symmetric component is observed, but a large number of target nucleons definitely participate in the interaction.

The most peripheral as well as the most central collisions for Cm are observed in the LMT bin 6÷9 GeV/c. The mass-asymmetry matrices for this bin are very similar to that for Ag, the peak of scission angle appears at $\theta_A \approx 50°$. The essential difference consists in the not heated PLF. No significant shift is observed between primary and secondary mass-asymmetry spectra. Moreover, their mean values of the asymmetric peak are close to the initial projectile/target asymmetry. Therefore, this asymmetric component originates from very peripheral collisions. The low yield of the symmetric component does not allow to compare mean values as for Ag in tab. 6.3, however, a few percent larger velocity for the symmetric case should be noted. The parameter R_χ took values 0.57 for the symmetric case and 0.70 for the asymmetric, respectively, e.g. a larger relative velocity is detected again in asymmetric fragment pair, as it was expected.

Summarizing, the preliminary analysis of the MARCH97 data has established three parameters to be reaction-time sensitive, namely: the total mass M, the excitation energy sharing parameter ζ and the TKE factor R_χ.

6.3.5 Anomaly of the cooling curve

It seems to be well established now, that a fissioning nucleus cools down by LP emission on the descent from saddle to scission. This is the reason for the lower mass width obtained at high excitation energies in comparison to that expected at lower excitation energies. This is an essence of the "cooling curve" phenomenon (cf. fig. 2.1 in Section 2.4). The conclusion has been drawn earlier, that the steep increase in the mass width ascribed to $E^* > 300$ MeV corresponds to a switching-on of some fast process. In order to distinguish against *ordinary fission* this process has been called "binary fragmentation" (BF). However, this process still lacks exploration.

High excitation energy has been deduced from high LMT. However, as it was already noted, an observed large LMT in *fission-like* processes does not generally mean high excitation energy. For peripheral reactions it means, that the PLF is registered and passed through kinematical filters as a fission-like product. By means of the analysis of excitation energy sharing one could try to find the BF process.

Spectra of primary and secondary asymmetries for "almost binary" events in Au data reveal the same kind of peaks of the excited PLF (fig. 6.27, left panel), as it was observed in Cm and Ag data (fig. 6.25, 6.26). However, these peaks are missing in Th data. They belong into the class of "ternary" events and, therefore, they are treated separately[14]. In contrast to Ag data, the difficulty to observe very peripheral collisions for Au and Th consist in the reduced registration efficiency of very light projectile remnants in the gas detectors. They rather reach scintillators and are treated as LCP or IMF. A PLF from

[13] Details of this interesting problems require a further analysis.

[14] This was discussed in terms of high fissility of Th in Section 6.1.2, p. 56.

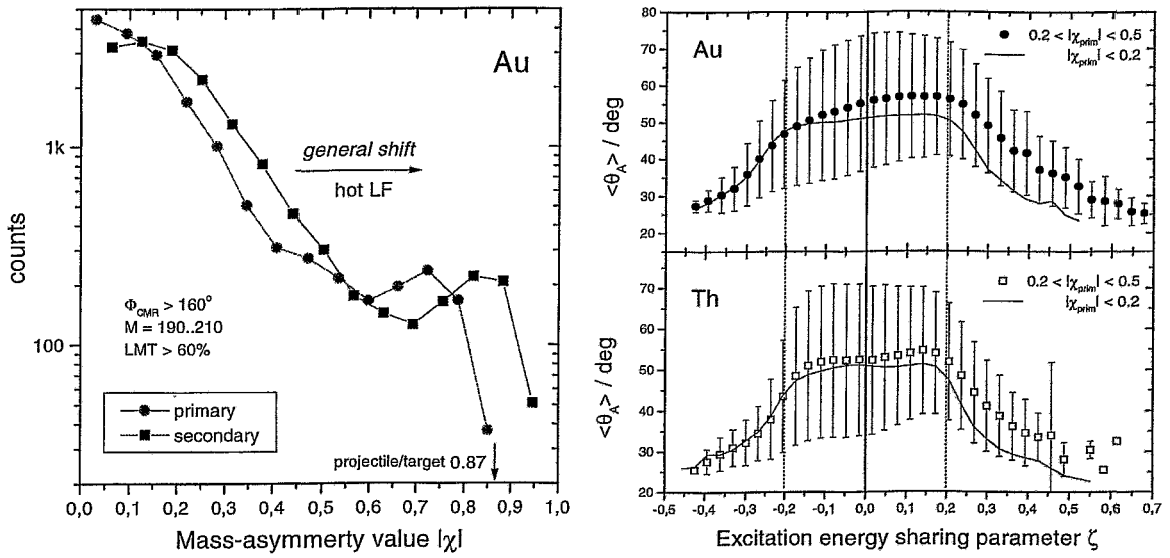

Figure 6.27: *Left panel: Spectra of mass-asymmetries accumulated for "almost binary" events in Au data. Right panel: Average scission angle for asymmetric (symbols) and symmetric (lines) splits. Variance is represented by error bars.*

a very peripheral collision escapes in the beam exit cone and could be registered only in ARGUS.

A significant difference between mass-asymmetry spectra of "almost binary" events for Au and Th on the one hand side, and for Cm and Ag, on the other hand side, is found in the mass-symmetric part of them. The part of asymmetry spectra at $|\chi| < 0.5$ is very similar for Th and for Au, therefore, only the one for Au is shown in fig. 6.27 (left panel). The whole spectrum of χ_{sec} is shifted toward asymmetric values with respect to the spectrum of χ_{prim} [15]. Such a large effect should indicate the fast process populating the entire range of mass-asymmetries.

In spite of acceptance problems angular distributions are very useful in the analysis of duration of the process. The dominating channel in the studied reactions of the JAN96 series is supposed to be *ordinary fission*. As a very slow process it should be characterized by an isotropic angular distribution and equilibrated excitation energy sharing.

The broad angular distribution of the PLF emission selected as $|\chi_{prim}| > 0.6$ for "almost binary" events in Th and Au data seems to be seriously affected by the acceptance (not shown in figures). Nevertheless, note for comparison purposes that the average scission angle amounts to 75°. The average scission angle for the entire data was considered in dependence on the excitation sharing parameter ζ (fig. 6.27, right panel). An average value $<\theta_A>$ and its variance were calculated for an angular distribution of θ_A produced for each presented value of ζ separately. Such a representation facilitates comparison between different ζ with respect to either an isotropic or focused angular distribution. Indeed, being processed in such a way, an ideal isotropic angular distribution delivers $< \theta_A >= 60°$ and variance $\approx 20°$. Deviations from this values should mean focusing.

[15] In order to judge wether the LF in a symmetric slit has the higher temperature one should explore the $\zeta - \chi$ matrix!

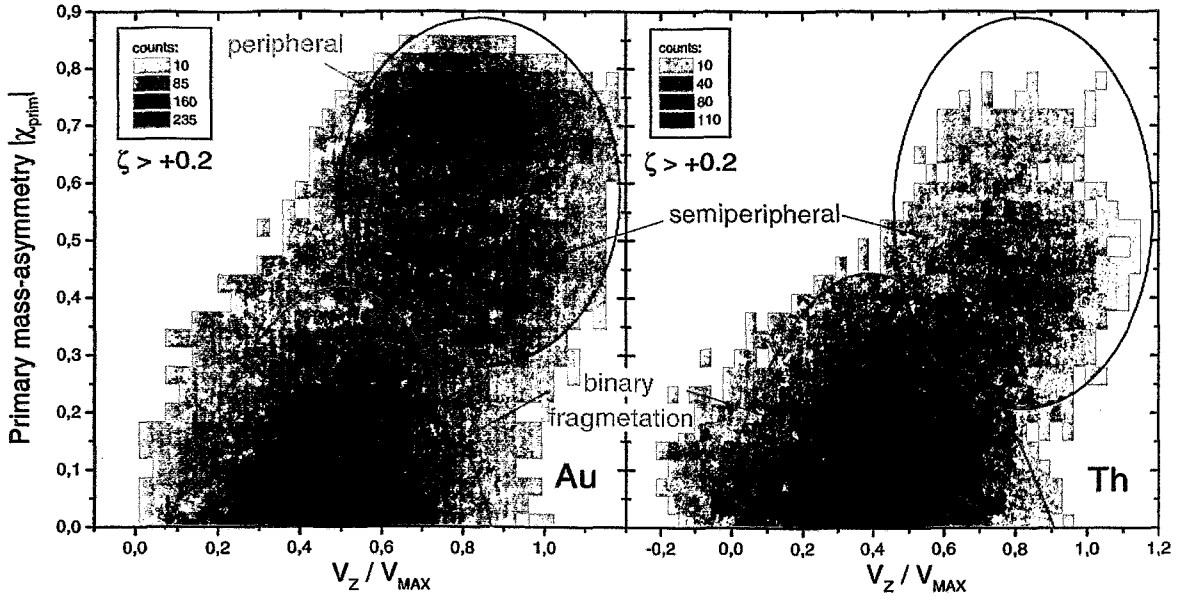

Figure 6.28: *Contributions of binary fragmentation and PLF emission. Respective areas are encircled. Spectra are accumulated under the constrain of* $\zeta > +0.2$.

Acceptance effects, of course, introduce complications.

Angular distributions for equilibrated decays in both "symmetric" and "asymmetric" bins for $|\zeta| < 0.2$ seem, in first approximation, isotropic. With increase in $|\zeta|$ the distribution becomes narrower and the average value drifts into the forward direction, i.e. focusing occurs. This tendency directly indicates that, on the average, the time scale for large $|\zeta|$ is shorter than that for equilibrated decays ($|\zeta| < 0.2$). As long as the behaviour of $<\theta_A>$ for $\zeta < -0.2$ and $\zeta > +0.2$ is similar (fig. 6.27, right panel), time scales corresponding to negative and positive ζ should be also similar.

The formation of a PLF-TLF system of a certain asymmetry from a given projectile/target configuration is defined, obviously, by the impact parameter. A general trend of decreasing the scission angle during the relaxation of the mass-asymmetry is found. This angle ranges from 75° for the "almost binary" decays (not shown, see also above) to much lower values for symmetric splits (fig. 6.27, right panel). This trend could be explained by means of variation of the impact parameter. However, the angular distributions at $\zeta < -0.2$ in "symmetric" and "asymmetric" bins does not differ. It means, that by applying the criteria mass-asymmetry and velocity no PLF is found. Rather a hot system decays very quickly into two heavy fission-like fragments, i.e. *binary fragmentation* (BF) occurs. It would be consistent to ascribe BF to semiperipheral or central collisions. If the PLF completely loses its "individuality", but the reaction is still governed by dynamical effects, e.g. the system is still not relaxed thermodynamically, sharing of the excitation energy between the fragments should reveal significant fluctuations. It means, that BF should populate the entire range of ζ-values. Indeed, the angular distributions for symmetric decays are quite similar for positive and negative values of ζ, whereas PLF formation should be found at positive ζ and this manifests itself in an obvious asymmetry of the angular dependence with respect to $\zeta = 0$ in the mass-asymmetric bin (fig. 6.27, right panel).

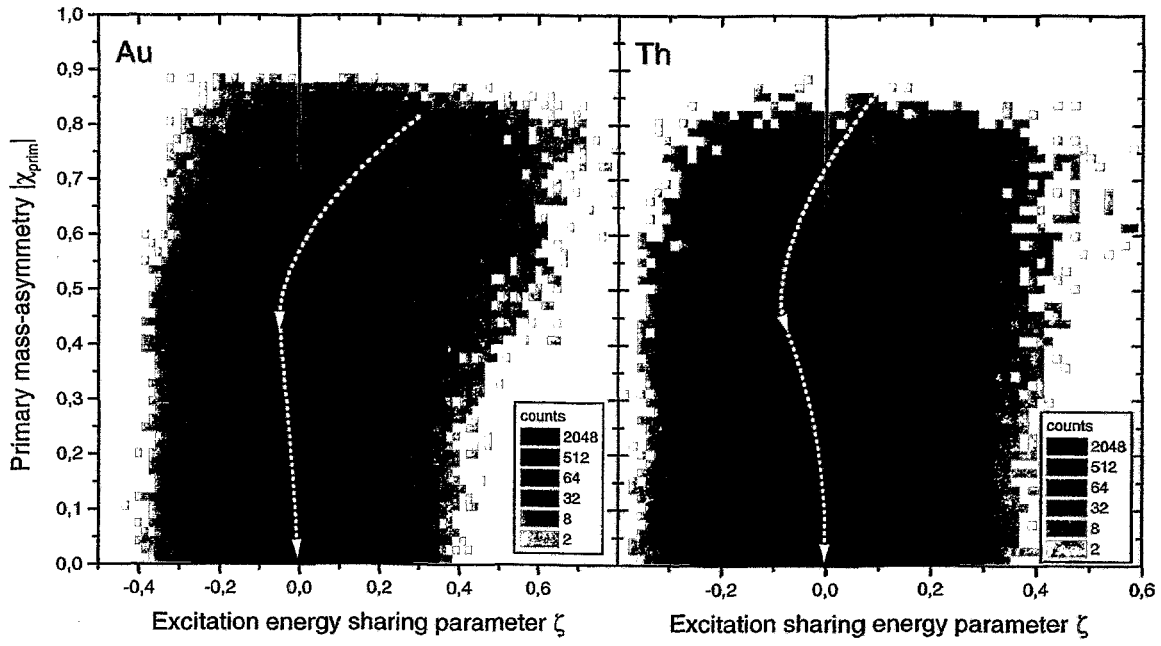

Figure 6.29: *The "trajectory" of the primary mass-asymmetry relaxation by means of the yields in the ζ-χ matrix (entire data).*

Hence, one should observe the whole set of fast processes for $\zeta > +0.2$. A good representation of these processes is found in the plot of χ_{prim} *vs* velocity of the c.m. of the composite system V_z (fig. 6.28). The spot of the "PLF-TLF mechanism" is encircled. As it was already noted, the most peripheral peak is absent in Th data. In other details both plots are similar. Although some number of PLF could be found in the "symmetric" bin, the bulk of events from BF is responsible for the mass-symmetric part of fast decays. The maximum of the BF yield is found at $V_z/V \approx 0.5$, what is consistent with its expected position at $E^* > 300$ MeV. This observation explains qualitatively the anomaly in the cooling curve and also gives a hint for further data processing.

6.3.6 Inventory of the $\zeta - \chi$ matrix

The analysis of the fission time scale requires, obviously, to select the channel of *ordinary fission*. As it follows from the previous section, this problem is difficult as long as many reaction channels are open.

The most reliable parameter which is really able to reflect the time scale of slow *ordinary fission* seems to be the total mass A_{tot}. The average total mass corresponding to a slower process should be lower because of a longer evaporation chain. Therefore the best separation of time scales by means of mass could be expected at high excitation energy, because evaporation would be intensive. On the other hand side, a high LMT region contains all of the above mentioned fast processes. Therefore, a general picture of interplay between these channels must be discussed.

PLF emission and the BF process significantly differ in excitation energy sharing and in mass-asymmetry. This is evidenced by the average of ζ which varies with $|\chi_{prim}|$. It is illustrated in fig. 6.29. The ridge of this distribution indicates the largest probability of a

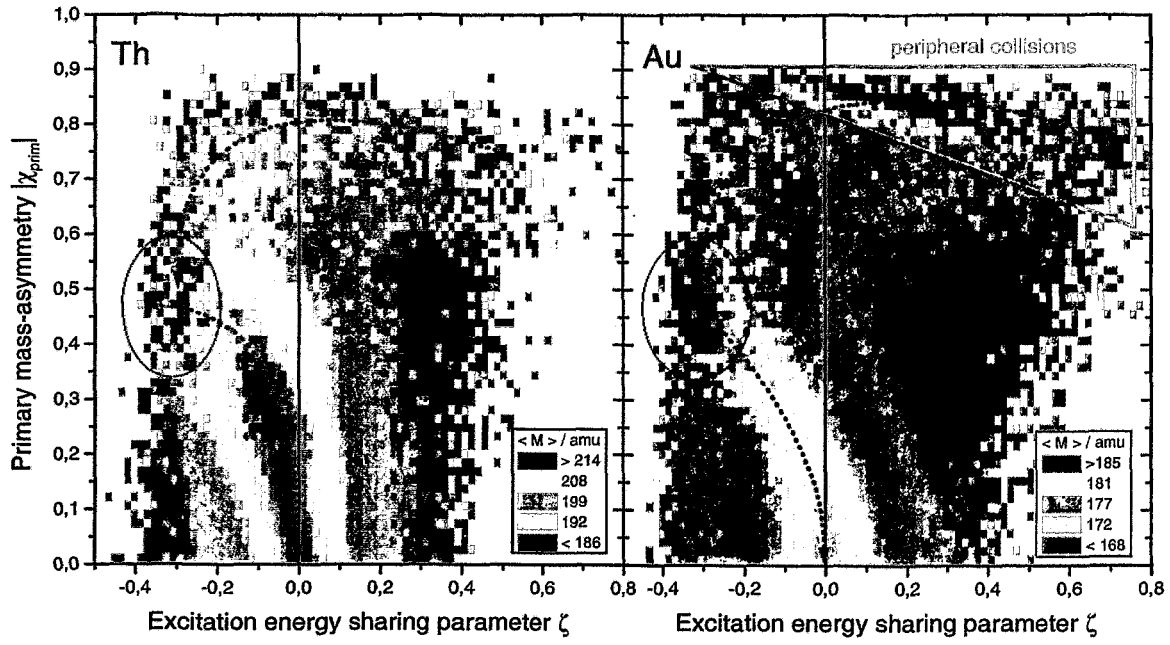

Figure 6.30: *The distribution of the average total mass in ζ-χ coordinates for entire Th data (left panel) and Au data (right panel). Ridges of the largest mass are schematically indicated by arrows. The triangle in Au data marks the area of peripheral collisions which is not pronounced in Th, the other maximum of mass is encircled.*

decay resulting in a certain excitation energy sharing ζ and a connected mass-asymmetry. Emission of a PLF, as the fastest and the most asymmetric process is represented by positive values of ζ, i.e. the temperature of the light fragment is higher, than the temperature of the heavier fragment (cf. eq. 6.24). The BF process is slower, it is more mass-symmetric, and because of some yet unknown reasons the most probable temperatures of the lighter fragments are low. Probably, the BF process could be imagined in some sense as a bullet piercing a very viscous body and the bullet remains intact. *Ordinary fission* definitely dominates among most symmetric decays and, thus, excitation energy sharing approaches equilibrium. The indicated line in fig. 6.29 could be considered as "trajectory" in the mass-asymmetry *vs* excitation energy sharing plane and thus describes that relaxation of the entrance channel.

An even more indicative picture of the mass-asymmetry relaxation is the distribution of the average total mass in the same coordinates (fig. 6.30). The most probable channel in Th data becomes fission of a Th-like nucleus after very peripheral collisions, as it can be concluded from LMT and respective total mass distributions. Therefore, the contribution of equilibrated decays is enhanced. This explains the major difference between the distributions for Th and Au in fig. 6.30. The line of the largest mass follows the trend found in the yields (fig. 6.29), but it is more impressive.

The largest average mass corresponds, obviously, to the fastest process. Comparing, in the same coordinates, the distribution of the TKE factor $<R_\chi>$ and of the scission angle $<\theta_A>$ (fig. 6.31), on the one hand side, with the distribution of the total mass $<A_{tot}>$ (fig. 6.30), on the other hand side, one recognizes the processes responsible for the population of different areas.

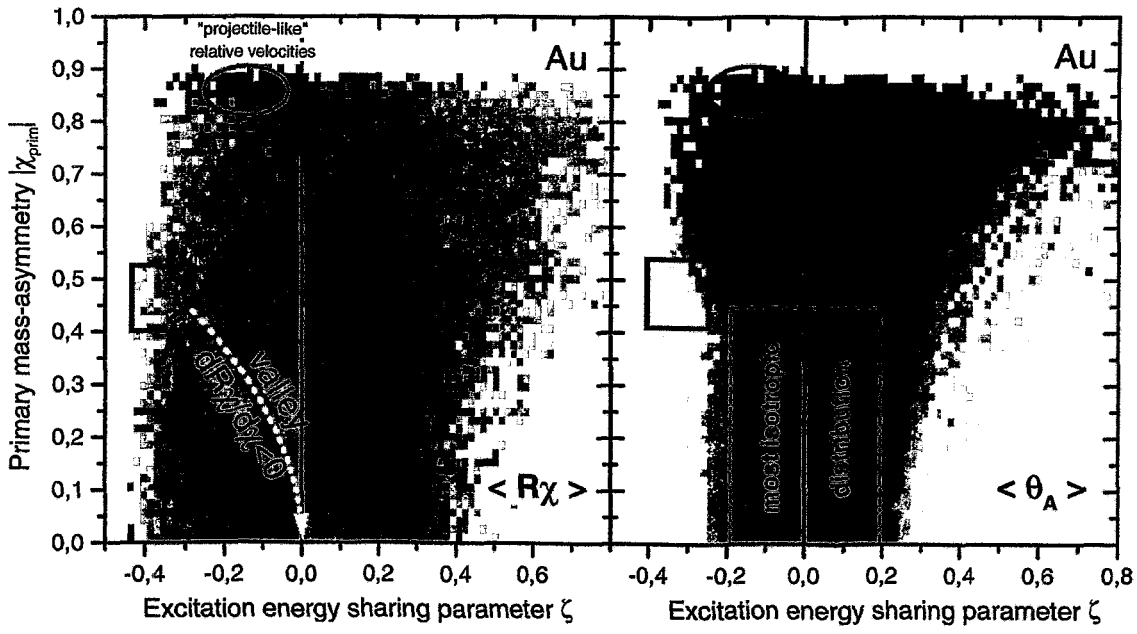

Figure 6.31: *The average TKE factor R_χ (left panel) and the average scission angle θ_A (right panel) for the entire Au data in ζ-χ coordinates. The circle marks the entry of most peripheral collisions, the square indicates the entry of most central ones.*

Probably, any process can be found with a certain probability in a given region in the ζ-χ matrix. However, two extreme values of the impact parameter can be found (fig. 6.31). They corresponds to the two entries of a fastest decay by means of a largest total mass. The entry of the most peripheral collision is indicated by significantly increasing R_χ, e.g. projectile-like velocity of a PLF. The entry of the most central collision is found at the moderate mass-asymmetry value of ≈ 0.5 in the minimum of the R_χ valley. One could follow two trajectories of evolution of the decaying system starting from these entries (fig. 6.32).

Decreasing the impact parameter from its limiting value to some moderate one results in growing of excitation energy and angular momentum of the TLF (trajectory "R_χ ridge"). The value of R_χ remains relatively large as long as the projectile is not completely stopped (see eq. 6.27). The TLF could undergo a fission-like decay, when certain values of angular momentum and of excitation energy are reached along the "trajectory". Such events would be recorded as "ternary"; but if one of the fragments is not registered this event in the "binary" data results in a low total mass. These fragments are located in the ζ-χ matrix apart of the equilibrium zone at moderate asymmetry (circle "ternary events"). This could indicate, as long as these events were not rejected by kinematical filters, that such a "ternary" event originates as a double neck rupture in the PLF-TLF system, or as collinear tripartition. The latter agrees with conclusions which have been made earlier in the analysis of ternary events from the same reactions [113]. This mechanism explains also a high yield of ternary events as well as the conclusion that the time interval between the first and second scission in tripartition is rather short [130].

The other trajectory starts from central collisions (trajectory "R_χ valley", same fig. 6.32), where the BF process is probable. Until the critically high angular momentum is not

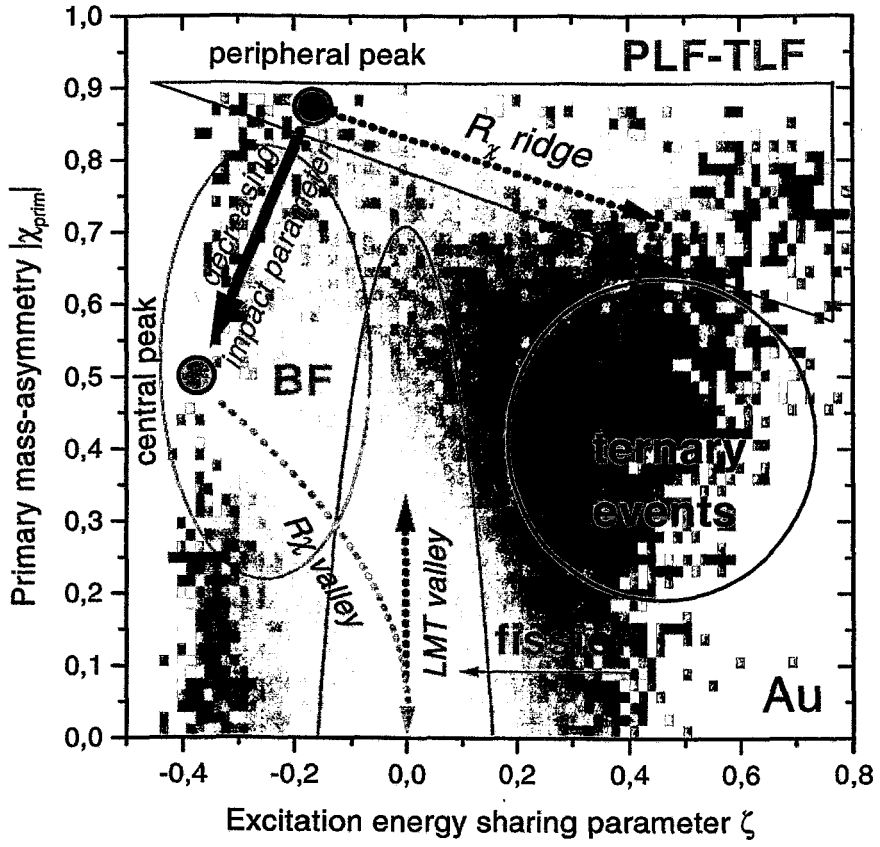

Figure 6.32: *Illustration for the different processes contributing the observed data. The total mass distribution for Au is used as the background; dark colors correspond to low masses. Details are explained in text.*

reached, the system can succeed to cool down by the particle emission. This is the reason, why the ridge of the total mass (fig. 6.30) corresponds exactly to the bottom of the R_χ valley (fig. 6.31). Indeed, the multiplicity of neutrons is much higher than that of LCP, therefore, the long evaporation chain leads always to increasing Z/A. It is the only reason for increasing R_χ, as long as the velocity of a projectile should be completely damped in central collisions. The relaxation of the asymmetry along the valley of R_χ takes a certain time, therefore, R_χ slightly increases (the arrow in fig. 6.31, left panel). The binary decay remains fast in the valley until the asymmetry is relaxed and the equilibrium is reached. Further evolution is related to slow *ordinary fission* along the axis of $\zeta = 0$ (trajectory "LMT valley" in fig. 6.32). Therefore, probably, the asymmetric *fission* life-time is longer resulting in $dR_\chi/d\chi > 0$, and the absolute value of this derivative is larger compared to that along the valley.

Such a representation of "trajectories" seems to be useful for interpreting the data. Some trends can be noted also in distributions of averaged Φ_{CMR}, V_z and LMT in the ζ-χ plane, although they do not supply such a clear visual information and, therefore, are not shown. It would be reasonable to suppose, that *ordinary fission* is very probable at some low LMT if a significant portion of the available excitation energy is removed by pre-equilibrium emission. Indeed, a local valley is found in the entire <LMT> and

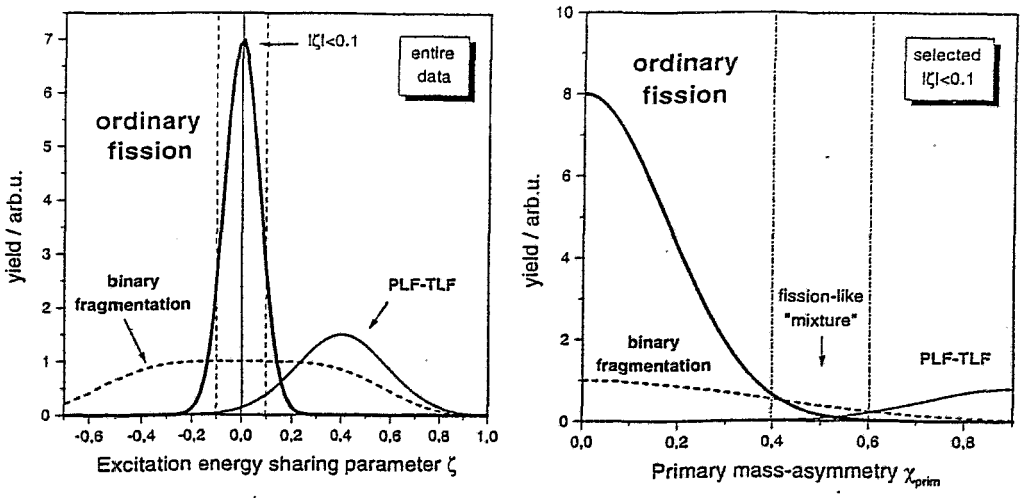

Figure 6.33: *Schematic illustration of superposition of PLF emission and binary fragmentation with the major contribution of ordinary fission. Left panel: Composition of the unconditioned ζ-spectrum. Right panel: Constraint of $|\zeta| < 0.1$ effectively separates the ordinary fission channel in the mass-asymmetry spectrum.*

the average folding angle $<\Phi_{CMR}>$ distributions around $\zeta = 0$ at $|\chi_{prim}| < 0.5$. Largest <LMT> are observed in the "PLF-TLF" area (fig. 6.32), where lower $<\Phi_{CMR}>$ indicates significant pre-equilibrium emission. Larger $<\Phi_{CMR}>$ values correspond to the BF area where pre-equilibrium emission should be rather isotropic.

6.3.7 Does asymmetric fission proceed faster?

The preliminary analysis revealed, that contributions of different processes populate the entire regions of LMT and V_z. The best discrimination between these processes could be found at moderate values of LMT. On the other hand side, the best "time resolution" by means of $< A_{tot} >$ could be achieved at high initial excitation energies of the fissioning nucleus (see also p. 87).

These reasons conditioned the window between 50% and 80% of the relative LMT, which was used for the analysis. In order to select *ordinary fission* the excitation energy sharing parameter was constrained to $|\zeta| < 0.1$ (fig. 6.33, left panel). The precise quantitative determination of contributions of each process is a matter of a very advanced analysis. The qualitative relation between different reaction channels fitting the given conditions is presented in (fig. 6.33, right panel). *Ordinary fission* should cause the major effect at $|\chi_{prim}| < 0.4$, the background of BF should be negligible for the analysis of the average total mass [16]. The area of dominating PLF emission is located at $|\chi_{prim}| > 0.6$ (PLF-TLF domain). The intermediate range of $|\chi_{prim}|$ represents comparable contributions of all "fission-like" processes .

Under the above mentioned conditions on ζ and LMT distributions in fig. 6.34 were produced. A close inspection reveals the following behaviour of the average parameters with increasing mass-asymmetry in the domain of *ordinary fission*.

[16]The contribution of BF, however, should be taken into account in the analysis of the width of the distribution of the fragment mass

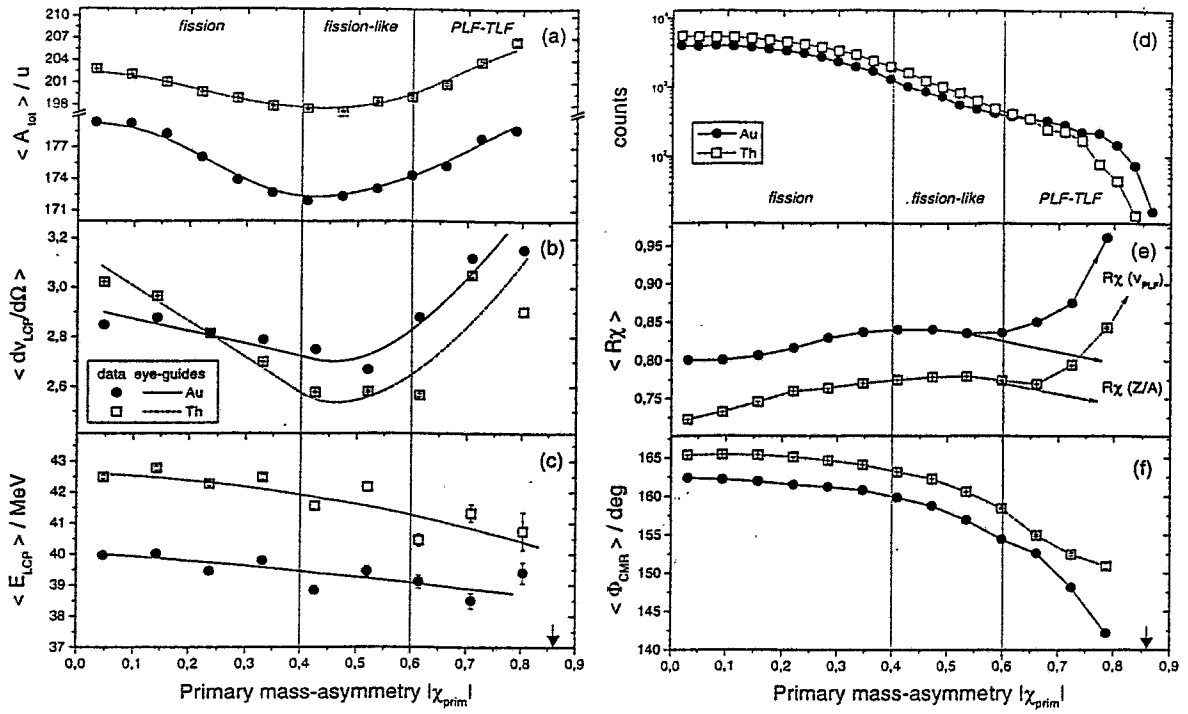

Figure 6.34: *Average values of parameters accumulated for* $\zeta < |0.1|$ *and LMT=50–80%. Error bars represent errors of averaging, lines are eye-guides. Arrows mark the position of the projectile/target initial mass-asymmetry.*

1. The decrease of the LCP multiplicity (b) indicates that the initial excitation energy of the system was higher, on the average, for symmetric fission. This is consistent with the small slope in the average LCP energy (c). The higher initial excitation energy observed in the mass-symmetric case should be defined by the smaller impact parameter.

2. The slight decrease of the average Φ_{CMR} (f) indicates a small difference in pre-equilibrium emission in the forward direction. This fact also proves smaller impact parameters to govern the symmetric case. In semi-central or central collisions selected by means of high LMT, a higher average angular momentum should be ascribed to a larger impact parameter. The latter means that a larger angular momentum corresponds, on the average, to the asymmetric case.

3. The observations 1 and 2 relate increasing angular momentum and decreasing excitation energy in the selected data to increasing mass-asymmetry.

4. The de-excitation by evaporation of particles significantly reduces the mass of a hot system prior to scission. Simultaneously, angular momentum is known to increase the fission probability and, hence, to reduce the fission life-time. Thus, increasing angular momentum should be observed as increasing total mass due to shortening the evaporation chain.

5. If there is no direct dependence of the fission life-time on mass-asymmetry ($\tau_{asym} = \tau_{sym}$) one should observe a constant total mass as a function of $|\chi_{prim}|$. However, because of the conclusion 3 and 4, a larger total mass should be observed in the asymmetric case.

6. If the life-time of asymmetric fission is smaller than that for symmetric fission ($\tau_{asym} < \tau_{sym}$), a larger total mass should be observed in the asymmetric case. Again, as in 5, conclusion 3 and 4 lead to the same consequence, namely, larger total masses with increasing mass-asymmetry.

7. As it follows from 5 and 6 the assumption $\tau_{asym} \leq \tau_{sym}$ always leads to an *increase* of the total mass with mass asymmetry. This obviously contradicts the *observed decrease* of $<A_{tot}>$ (a). Therefore, only longer life-times for asymmetric fission can be deduced.

8. A longer evaporation chain in the asymmetric case leads to an increase of Z/A with mass-asymmetry, and this is observed as an increase in R_χ (e).

9. Considering the statistical nature of fission, the average duration of the process is inversely proportional to the process probability. The decreasing decay probability is observed as a reduction of the yield of asymmetric fission (d).

The PLF-TLF domain $|\chi_{prim}| > 0.6$ is characterized by an increase of the total mass because PLF formation is very fast [a]. The tendency of $R_\chi(Z/A)$ to decrease [e] occurs because of returning back to the initial isotopic composition (represented by arrows). However, it cannot compete with the contribution of $R_\chi(v_{PLF})$, which is steeply growing accounting for the projectile-like velocity of a PLF. The emission of LP with projectile-like velocity also becomes possible due to a large impact parameter and this is indicated by the dropping down of Φ_{CMR} [f].

The discussed picture of physical processes is definitely simplified. Probably, a lot of particular effects come also into play. However, the observed experimental data reveal the general trend of the longer duration of asymmetric *ordinary fission* compared to symmetric *ordinary fission*. The BF process together with PLF emission reveals the opposite trend, because relaxation of the mass-asymmetry in the entrance channel requires a certain time. Therefore, considering all these processes together one is lead to the reasonable conclusion, that an asymmetric "fission-like" decay is faster than a symmetric "fission-like" decay.

A similar conclusion on the interplay of fast fission-like processes with ordinary fission and large fluctuations of sharing of the excitation energy between the fragment has been made in the chemical study of $A - Z$ distributions from the reaction ^{51}V (25 AMeV) + ^{197}Au in ref. [131]. The importance of the study of excitation energy sharing is stressed in refs. [128, 129].

Chapter 7

Summary

The thesis aimed at the qualitative comparison of time scales of symmetric and asymmetric fission. Main goals of the present work are given in Section 2.5. During fulfilling this research program the following tasks were executed.

- The desired FOBOS scintillator shell was completed and turned into operation.
- Its capability to register light charged particles (LCP) was demonstrated. Methods for the LCP raw data processing were developed.
- Data were taken in a series of full-scale experiments.
- The validity of the data from the FOBOS scintillator shell was exhaustively tested. Their reliability and self-consistency are demonstrated.
- Numerical simulations were performed using the Dubna Cascade Model (CASCAD code) and the Combined Dynamical Statistical Model (SAND code). These simulation aimed mostly at obtaining auxiliary information for data interpretation.
- A new method for the energy calibration of CsI(Tl) crystals is proposed. The method is based on the physical properties of CsI(Tl) crystals. The most attractive features of the method are: minimized manpower expenses, an independence of the calibration data on corresponding calibration beams, a high degree of automation and a visual quality inspection.
- A new method of the experimental data analysis is proposed. The method is based on the independent measurement for the velocity and for the energy of heavy fragments by the FOBOS detector. This allows to reconstruct the mass-asymmetry of the decaying system at the instant of scission. This information is transformed into the parameter ζ reflecting the partitioning of excitation energy which is a means to separate different processes contributing to the measured bulk of data. Results obtained in this unconventional way open new prospects for a more advanced data analysis.
- The main result of this thesis consists in the separation of reaction channels into *ordinary fission* known from low energies and a number of fast processes by means of a specially designed parametrization. These processes cannot be distinguished from *ordinary fission* using conventional methods of the analysis. The physical "picture" of fission and related time scales deduced from the experimental data is in following.

1. Ordinary fission.According to the classical picture the *ordinary fission* process is related to a compound nucleus which is defined to be an equilibrated system with a relaxed compact shape. The probability of *ordinary fission* into a given configuration depends on the height of the corresponding fission barrier. From the calculations of potential energy surfaces follows that the fission barrier increases with increasing mass-asymmetry. Due to the statistical nature of the process the fission time scale is inversely proportional to the fission probability. The decrease of the fission probability is observed directly as a decrease of the yield of asymmetric fission compared to the symmetric one. The corresponding increase of the fission time is concluded from the length of the evaporation chain observed as a decrease of the total mass of the fragments with increasing the mass-asymmetry.

2. Fission-like fast processes. The initial configuration of the touching target and projectile nuclei with a given relative velocity requires a certain time for relaxation into a compound nucleus. Two stages of the relaxation should be mentioned.

   The fastest fission-like process observed is a decay of the non-equilibrated system formed in semiperipheral collisions where a projectile-like fragment (PLF) and a target-like fragment (TLF) can be identified. The duration of this process should be of the order of the contact time. The very short reaction time manifests itself in a similarity of the velocity of a PLF with the initial projectile velocity and in a preferably higher temperature of the PLF compared to the TLF.

   Evidence is found for a slower *fission-like* process which is characterized by a rather symmetric configuration at the scission point. A manifestation of this process has been observed earlier and it has been called "hot binary fragmentation". It should be associated with the most central collisions. In this case no definite PLF could be found by means of velocity and mass-asymmetry distributions. The essentially short duration of this process is observed by non-equilibrium sharing of excitation energy between the fragments. In contrast to the PLF-TLF formation the higher temperature must be ascribed, on the average, to the heavier fragment.

   Both of these fast processes are accompanied with intensive emission of light particles (LP). Each particle carries away mass, a portion of energy and angular momentum. As a result the system configuration evolves into a relaxed state. The further evolution of the system leads to *ordinary fission* or to formation of an evaporation residue. In some sense, ordinary fission is realized in this case *instead* of the faster processes mentioned.

3. Ternary events.Provided the excitation energy in the heavier remnant after PLF emission is large enough, this remnant can undergo a further binary decay. Thus, all the "binary" events observed at low a LMT could be treated as "ternary" events, since in the most peripheral collisions a rest of the projectile is lost from the registration if it is emitted into in the beam exit cone, and only the binary decay of a TLF is observed.

   Semiperipheral collisions result in a higher LMT. The decay of a TLF after emission of an excited heavy PLF can then be recorded as "ternary" decay. Such a mechanism seems to be responsible to the mass-symmetric tripartition. Those of "ternary" events, where one fragment is not recorded are characterized by a lower total mass but a large velocity of their center of mass.

The significant difference between central and semiperipheral collisions consists in the different value of the angular momentum. The decay probability is enhanced at higher angular momenta. Therefore, the decaying system originating from a central collision can succeed to cool down by LP emission and then undergo *ordinary fission*. Such events are observed at high LMT.

Such a picture of "fission" governed by thermodynamical and statistical laws is consistent with the observed experimental data. Therefore, contribution of *fission-like* processes other than *ordinary fission* must be distinguished. This was made possible by introducing the excitation energy sharing *vs* mass-asymmetry matrix (ζ-χ), which allows a deeper insight into the dynamics of heavy-ion induced reactions.

Appendix A

Geometry of the scintillator shell

Table A.1: *CsI(Tl) scintillator detectors coordinates. Each line represents a ring of CIS with an equal polar angle θ given in the last column in ascending order. The number of a CIS consists of a module number (first two digits) and a crystal number in a module (last digit). The crystal number 1 corresponds to the center of a module (bold faced lines). Dimensions of crystals are given in the form thickness×diameter, Ω_Σ is the calculated summed solid angle of all crystals in a ring. (to be continued on the next page)*

CsI #	ϕ	CsI #	ϕ	CsI #	ϕ	CsI #	ϕ	CsI #	ϕ	θ
Ring 1, big modules, Ω_Σ=1.068 sr, crystals 15 mm ×200 mm										
014	78.21	024	150.21	034	222.21	044	294.21	054	6.21	28.21
015	101.79	025	173.79	035	245.79	045	317.79	055	29.79	28.21
011	**90.00**	**021**	**162.00**	**031**	**234.00**	**041**	**306.00**	**051**	**18.00**	**37.38**
012	72.03	022	144.03	032	216.03	042	288.03	052	0.03	38.77
013	107.97	023	179.97	033	251.97	043	323.97	053	35.97	38.77
016	82.45	026	154.45	036	226.45	046	298.45	056	10.45	47.31
017	97.55	027	169.55	037	241.55	047	313.55	057	25.55	47.31
Ring 2, small modules, Ω_Σ=0.665 sr, crystals 10 mm ×150 mm										
062	126.00	072	198.00	082	270.00	092	342.00	102	54.00	54.58
064	117.07	074	189.07	084	261.07	094	333.07	104	45.07	59.29
065	134.93	075	206.93	085	278.93	095	350.93	105	62.93	59.29
061	**126.00**	**071**	**198.00**	**081**	**270.00**	**091**	**342.00**	**101**	**54.00**	**63.44**
066	117.73	076	189.73	086	261.73	096	333.73	106	45.73	68.11
067	134.27	077	206.27	087	278.27	097	350.27	107	62.27	68.11
063	126.00	073	198.00	083	270.00	093	342.00	103	54.00	72.30
Ring 3, big modules, Ω_Σ=1.068 sr, crystals 10 mm ×200 mm										
114	84.09	124	156.09	134	228.09	144	300.09	154	12.09	69.61
115	95.91	125	167.91	135	239.91	145	311.91	155	23.91	69.61
111	**90.00**	**121**	**162.00**	**131**	**234.00**	**141**	**306.00**	**151**	**18.00**	**79.19**
112	78.67	122	150.67	132	222.67	142	294.67	152	6.67	79.40
113	101.33	123	173.33	133	245.33	143	317.33	153	29.33	79.40
116	84.46	126	156.46	136	228.46	146	300.46	156	12.46	88.87
117	95.54	127	167.54	137	239.54	147	311.54	157	23.54	88.87

Table A.1: *CsI(Tl) scintillator detectors coordinates. Continuation.*

CsI #	ϕ	CsI #	ϕ	CsI #	ϕ	CsI #	ϕ	CsI #	ϕ	θ
Ring 4, big modules, Ω_Σ=1.068 sr, crystals 10 mm ×200 mm										
166	131.54	176	203.54	186	275.54	196	347.54	206	59.54	91.13
167	120.46	177	192.46	187	264.46	197	336.46	207	48.46	91.13
162	137.33	172	209.33	182	281.33	192	353.33	202	65.33	100.60
163	114.67	173	186.67	183	258.67	193	330.67	203	42.67	100.60
161	**126.00**	**171**	**198.00**	**181**	**270.00**	**191**	**342.00**	**201**	**54.00**	**100.81**
164	131.91	174	203.91	184	275.91	194	347.91	204	59.91	110.39
165	120.09	175	192.09	185	264.09	195	336.09	205	48.09	110.39
Ring 5, small modules, Ω_Σ=0.665 sr, crystals 10 mm ×150 mm										
213	90.00	223	162.00	233	234.00	243	306.00	253	18.00	107.70
216	98.27	226	170.27	236	242.27	246	314.27	256	26.27	111.89
217	81.73	227	153.73	237	225.73	247	297.73	257	9.73	111.89
211	**90.00**	**221**	**162.00**	**231**	**234.00**	**241**	**306.00**	**251**	**18.00**	**116.56**
214	98.93	224	170.93	234	242.93	244	314.93	254	26.93	120.71
215	81.07	225	153.07	235	225.07	245	297.07	255	9.07	120.71
212	90.00	222	162.00	232	234.00	242	306.00	252	18.00	125.42
Ring 6, big modules, Ω_Σ=1.068 sr, crystals 10 mm ×200 mm										
266	133.55	276	205.55	286	277.55	296	349.55	306	61.55	132.69
267	118.45	277	190.45	287	262.45	297	334.45	307	46.45	132.69
262	143.97	272	215.97	282	287.97	292	359.97	302	71.97	141.23
263	108.03	273	180.03	283	252.03	293	324.03	303	36.03	141.23
261	**126.00**	**271**	**198.00**	**281**	**270.00**	**291**	**342.00**	**301**	**54.00**	**142.62**
264	137.79	274	209.79	284	281.79	294	353.79	304	65.79	151.79
265	114.21	275	186.21	285	258.21	295	330.21	305	42.21	151.79

Table A.2: *Positioning principle of opposite crystals*

Numbers of opposite detector modules														
1	2	3	4	5	6	7	8	9	10	11	12	13	14	15
28	29	30	26	27	24	25	21	22	23	18	19	20	16	17
Numbers of opposite crystals in opposite modules														
"big" module							"small" module							
1	2	3	4	5	6	7	1	2	3	4	5	6	7	
1	3	2	5	4	7	6	1	2	3	5	4	7	6	

Table A.3: *Summary of actual CIS-detectors for the JAN96 experiment*

Parameter	Ring 1	Ring 2	Ring 3	Ring 4	Ring 5	Ring 6
average angle θ_{ave}, deg	37.67	63.24	78.17	100.72	116.72	142.06
solid angle Ω_{ring}, sr	0.914	0.494	0.795	0.795	0.550	1.008

Appendix B

Energy calibration data

The tables contain data calculated for the FOBOS configuration of the JAN96 experiment. Fit parameters in the tables are taken from a computer output as they are. The tables below refer to the following functions:

$$E_t = [(E_d + E_0)^\alpha + C^\alpha]^{1/\alpha} - E_0 \tag{B.1}$$

$$f(x) = ax^b + c_1 x/(d_1 + x) + c_2 x/(d_2 + x). \tag{B.2}$$

Table B.1: *Fit coefficients for energy loss calculations by the formula B.1. The cases of normal (central crystals) and slanting (outer crystals) particle penetration are considered. The gas pressure in the BICs is assumed to be 150 Torr.*

	E_0	C	α	E_0	C	α
Ion	Outer crystals			Central crystals		
thin BIC anode foils 1.5 μm						
p	0.2116	3.09303	1.76903	0.20732	3.05259	1.76129
d	0.41395	4.1717	1.76823	0.37747	4.09453	1.75745
t	0.50276	4.8909	1.75458	0.48363	4.823	1.74946
^{3}He	0.7263	11.0726	1.78049	0.68896	10.92656	1.7786
^{4}He	1.0799	12.63206	1.7855	1.13937	12.52952	1.78758
^{6}He	1.86201	15.24702	1.79386	1.78317	15.0344	1.79158
^{8}He	2.40937	17.27603	1.79254	2.87015	17.36607	1.80559
^{6}Li	3.74296	24.91118	1.81884	2.83395	24.0716	1.80405
^{7}Li	5.11629	27.21605	1.83742	5.01941	26.86323	1.83534
thick BIC anode foil 10 μm (module #2 in JAN96)						
p	0.21471	3.26256	1.77385	0.2132	3.22395	1.76862
d	0.40393	4.38943	1.76963	0.36276	4.316	1.76244
t	0.52643	5.18408	1.76281	0.36276	5.03409	1.76244
^{3}He	0.68814	11.63232	1.78336	0.66644	11.49118	1.78131
^{4}He	1.04193	13.28682	1.78965	1.02381	13.12669	1.78749
^{6}He	1.76053	16.01103	1.79644	1.90218	15.92057	1.79984
^{8}He	2.43152	18.23875	1.79924	2.35916	17.99338	1.79647
^{6}Li	3.63208	26.14455	1.82255	3.47088	25.75842	1.81847
^{7}Li	4.3708	28.07572	1.82262	4.78389	28.1192	1.83656

Table B.2: *The "ideal" PIM model. Fit coefficients for the energy calculation for τ_{slow}=4 μs in the form of eq. B.2, where $x=L_{fast}$ and $y=E_d$ are assumed. Fit coefficients for the particle branches and inter-branch separators in the "ideal" PIM presented in the same form, but $y=L_{slow}$. The lines for He and Li are reliable, of course, only above a certain resolution threshold. p' denotes the descending proton line $E > E_{PTP}$.*

ion	a	b	c_1	d_1	c_2	d_2
A. Energy calibration coefficients for the ideal PIM						
p	0.08324	1.03117	-43.207	1374.367	0.57229	5.70191
d	0.12551	0.99247	-88.980	1529.238	0.64706	4.36303
t	0.14229	0.97979	-127.685	1927.394	0.79062	4.5601
^{3}He	0.22908	0.92521	-315.802	3735.899	1.26262	3.06503
^{4}He	0.25122	0.91507	-361.367	4170.621	1.44649	3.02738
^{6}He	0.29176	0.89858	-419.180	4678.786	1.71184	2.84082
^{8}He	0.3211	0.88944	-479.487	5238.052	1.99135	2.83548
^{6}Li	0.37831	0.87784	-668.406	6909.963	2.73615	3.00315
^{7}Li	0.38961	0.87082	-609.090	6673.603	3.11469	3.00423
B. Particle lines in ideal PIM						
p'	0.3714	1.18186	8142.797	2998.919	-20501.84	9120.779
p	0.48839	1.13094	621.825	347.711	-458.941	222.685
d	0.43988	1.11798	1429.507	1657.210	-474.625	462.552
t	0.23512	1.158	7045.592	2100.823	-4188.443	1290.425
^{3}He	0.05881	1.27889	16187.578	8330.697	-6331.916	3692.019
^{4}He	0.06449	1.28435	13524.682	12334.791	-3902.989	4264.449
^{6}He	0.09296	1.2638	3707.568	10314.465	-981.481	3022.859
^{8}He	0.08081	1.25836	16504.738	29201.165	-3164.483	6685.976
^{6}Li	0.10516	1.22514	17577.774	38372.710	-5838.571	14524.649
^{7}Li	0.09991	1.20345	18646.626	33347.346	-3200.693	7051.915
C. Separator lines in ideal PIM						
	Upper limits for particles					
p	1.32348	1.0	-410.274	42.176	383.346	44.634
d	0.82215	1.06394	-402.433	254.212	400.577	390.581
t	0.79713	1.06905	-522.816	383.793	400.577	492.679
^{3}He	0.17238	1.22917	0.0	0.0	0.0	0.0
^{4}He	0.12884	1.25792	0.0	0.0	0.0	0.0
^{6}He	0.04144	1.36615	4026.834	2780.09	-2884.015	2206.393
^{8}He	0.05351	1.32963	-529.229	4135.02	1810.962	7213.716
^{7}Li	0.10842	1.235	0.0	0.0	0.0	0.0
	Lower limits for particles					
t	0.74891	1.073	-267.371	404.395	810.406	16750.461
^{8}He	0.04994	1.33468	-1116.377	3600.116	1243.261	2685.226
^{7}Li	0.05103	1.29659	-512.455	1602.960	1691.891	4376.089
	General validation limits					
upper	12.3378	0.72351	73.495	2696.908	-442.722	117.152
lower	0.08232	1.22618	0.0	0.0	0.0	0.0

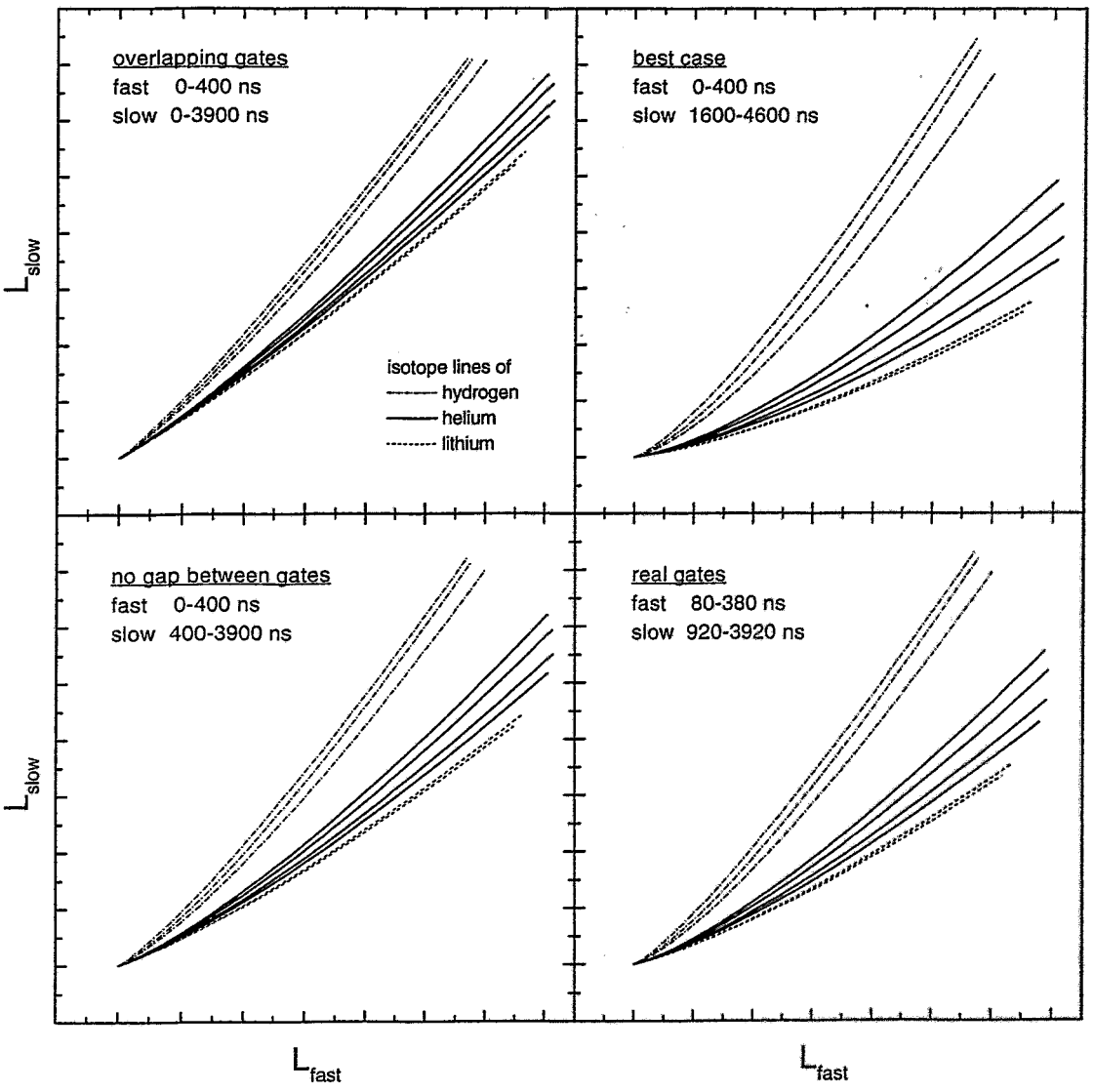

Figure B.1: *Simulation of the particle-identification matrixes under different timing conditions using the data from ref. [75] as described in section 5.3. The simulated particle set is limited to $Z < 4$. The phoswich principle is obviously the worst one, it leads however to the better resolution between heavier particles. The best case is not realized because of trigger logic requirements, real timing conditions etc. The gap between gates slightly increases the resolution.*

Appendix C

Kinetic temperature

This most widely used method to determine the temperature T_{kin} of nuclei from LCP data is based on measurements of kinetic energy spectra of emitted particles (slope parameter). A nucleus in thermal equilibrium evaporates particles with an energy distribution defined by the Maxwell-Boltzmann formula:

$$N(E_k) = C(E_k - B_c)exp(-\frac{E_k - B_c}{T_{kin}}), \tag{C.1}$$

where E_k is the kinetic energy of the emitted particle, B_c is the Coulomb barrier, and T_{kin} the temperature of the source after emission. A chain of evaporated particles "delivers" an average temperature of the entire cascade. The problem of fitting consists in adequately accounting for the maximum of the distribution, especially in the case of limited statistical accuracy of the measured spectra or multi-source fits.

Actually, different modification of the general exponential law are used to fit evaporative particle spectra in order to extract the slope parameter *related* to the nuclear temperature. For instance, Peter et al. [132] used the following form to extract the slope parameter S:

$$N(E_k) = C\frac{E_k - B_c}{S^2}\exp(-\frac{E_k - B_c}{S}). \tag{C.2}$$

In order to fit kinetic energy distributions of light charged particles emitted from a compound nucleus and fission fragments, Lestone proposed [133] the following parametrization of a Maxwellian form (in rest frame of emitters):

$$N(E_k) = 0, \quad E_k \leq B', \tag{C.3}$$

$$N(E_k) \propto C'\left(E_k - B'\right)^D \exp\left(-\frac{E_k}{T}\right), \quad B' < E_k < B + T, \tag{C.4}$$

$$N(E_k) \propto (E_k - B)\exp\left(-\frac{E_k}{T}\right), \quad E_k \geq B + T, \tag{C.5}$$

where $C' = T/\left(DT\right)^D$ and $B' = (1 - D)T + B$. The parameter T is the mean temperature of the source which controls the slope of the energy distribution at higher energies, B is the mean height of the emission barrier, and D is related to the curvature and penetrability of the barrier and controls the slope of the distribution at lower energies. The maximum of the distribution occurs at $E_k = B + T$.

Appendix D

Numerical simulations

D.1 Cooling down by light particle emission

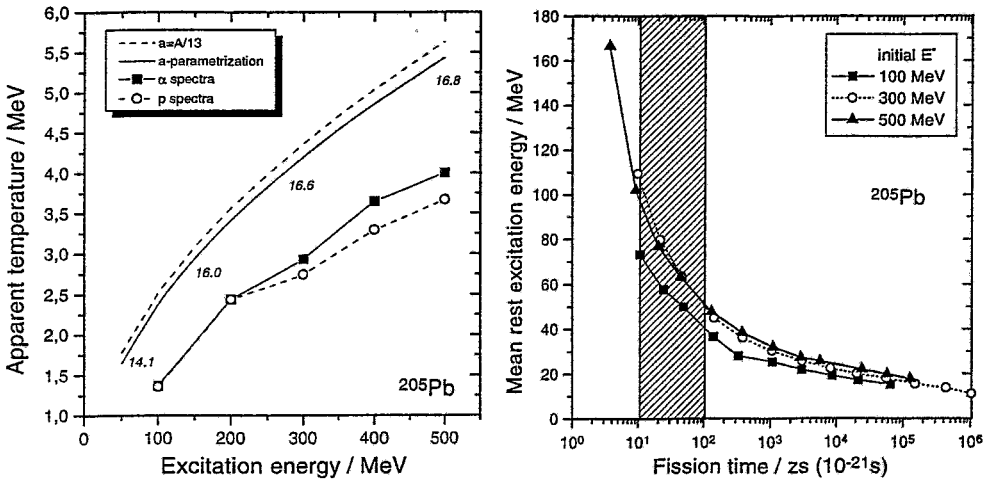

Figure D.1: *Left panel: Apparent temperatures are obtained by fitting CDSM-generated kinetic energy spectra (lines+symbols) for ^{205}Pb. Caloric curves assume a level density parameter $a = A/13$ (dashed line) and using the systematic from ref. [135] (solid line, numbers denote a in some points). Right panel: Cooling curves are simulated for three values of the initial excitation energy. The hatched area corresponds to most probable fisison times.*

The simulations by the Combined Dynamical Statistical Model (CDSM) [118] were performed for the fission of a ^{205}Pb nucleus by using the program code SAND, developed within the FOBOS collaboration [134, 120]. The code calculates event-by-event for an equilibrated compound nucleus with given values of excitation energy E^* and angular momentum J the sequence of emitted light particles (γ, n, p, d and α) with their energies, the residual excitation energy and the duration of a cascade leading either to ordinary fission or to formation of an evaporation residue.

Energy spectra of light particles were accumulated for trajectories leading to fission and the slope parameter T was derived assuming the Lestone type parametrization. The apparent temperatures turned out to be lower than they were calculated using level density

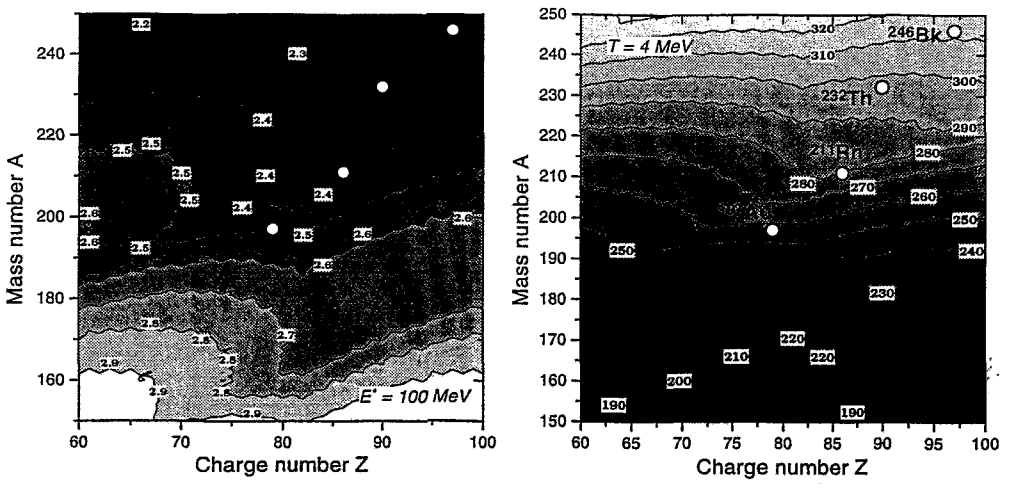

Figure D.2: *Left panel: The surface of the nuclear temperature is calculated for a fixed excitation energy of 100 MeV. Numbers mark lines of equal temperatures. Right panel: The excitation energy surface is calculated for a fixed temperature of 4 MeV. Numbers denote lines of equal excitation energies.*

parameter systematics. Neutrons emitted prior to charged particles remove a significant portion of the excitation energy, thus the emitter cools down. As it follows from simulations, α-particles should be evaporated, on the average, earlier than protons. Therefore, protons demonstrate lower apparent temperatures than α-particles do. Indeed, this is pronounced in the experimental data.

As it would be expected, the mean excitation energy remaining in the system at the instant of scission asymptotically decreases as the duration of an evaporation cascade increases (fig. D.1, right panel). The most probable scission happens within the period of 10–100 zs. The residual excitation energy seems to be not sensitive to initial values exceeding ~100 MeV. The latter is reflected in the saturation of the cooling curve derived from mass dispersions (see Chapter 2). The influence of the angular momentum on the temperature, emission chances and multiplicity distributions is found to be very weak.

The slope parameter reaches its experimental value of ≈4 MeV only at high excitation energy of about 500 MeV. This definitely means, that the cooling-down effect cannot reproduce the experimentally observed behavior of the apparent temperatures alone. It seems to be reasonable that averaging over the ensemble of different emitting nuclei contributes to the complication of the behavior of the apparent temperature.

D.2 Available temperatures

The calculation of effective nuclear temperatures was performed using the empirical approach [135] based on the experimental data systematics from ref. [136]. The absolute upper limit of the temperature was estimated assuming complete fusion with full dissipation of the beam energy. The corresponding compound nuclei are $^{211}_{86}Rn$ (T=6.3 MeV) and $^{246}_{97}Bk$ (T=5.9 MeV). Therefore the value of the apparent temperature of ~4 MeV at high LMT looks reasonable.

However, the apparent temperature obtained from the proton spectra at $E^* \approx 100$ MeV

seems to be overestimated. Mixing of sources with different temperatures could result in a small increase of apparent temperature. The other reason could be related to the inadequate description of spectra by the Leston-parametrization due to the rather broad Coulomb barrier distribution caused by the deformation and the rotation of a nucleus, especially if a slope is measured near to the peak of a spectrum. However, the contribution of both these effects do not exceed ~ 1 MeV[137].

Figure D.2 (left panel) presents the surface of nuclear temperatures calculated for the fixed excitation energy of 100 MeV. The corresponding temperatures should be around 2.4 MeV. At $E^* \approx 100$ MeV the cooling effect should not be strong. On the other hand side, as it is seen from the excitation energy distribution (right panel) calculated for the fixed temperature of a nucleus, the values of the initial temperature of about 4 MeV correspond to 260–300 MeV of the excitation energy. Note, that the maximum of the LMT distribution for central collisions corresponds to $E^* \approx 300$ MeV and the value of 100 MeV in Th data is covered by the strong peak of peripheral collisions. Therefore, the most probable reason for the overestimation of the apparent temperature is that the LMT values is not an adequate measure of the initial excitation energy. The latter means, that the contribution of processes other than fission after incomplete fusion and/or pre-equilibrium emission should be also taken into consideration.

D.3 Pre-equilibrium emission

Usually pre-equilibrium emission is treated as forwardly peaked. However, as one can conclude from simulations by R.Yanez [5] (BUU + evaporation code), pre-equilibrium emission might compete with evaporation from a compound nucleus even in the backward hemisphere. The test particle technique of the BUU model is not able to generate particles heavier than a nucleon which are apart of TLF and PLF. However, it would be interesting to estimate the contribution of pre-equilibrium emitted α-particles as well as to compare predictions of the BUU with other models.

The so called "Dubna Cascade Model" [138] was used to explore the contribution of more complex pre-equilibrium emitted fragments. The collision between nucleons in DCM is treated in a similar way as in the BUU model, but DCM does not resort to the test-particle technique and the dynamics of each NN collision can be followed. The coalescence formalism is used to produce complex particles. In spite of probable difficulties of the coalescence model, e.g. possible underprediction of the pre-equilibrium particle multiplicities [139], one can make some estimations.

Calculated inclusive spectra of protons and α-particles for the reaction ^{14}N (53AMeV)+ ^{197}Au, accumulated at different polar angles are presented in fig. D.3. The direct comparison with experimental data is scarcely possible because the DCM version used does not differentiate between exit channels. This results in incomparable yields of LCP originating, in particular, from the projectile break-up. However, the spectra responsible for the evaporation from the TLF rather well agree with the experiment. Two experimentally observed trends are reproduced as well – the spectrum slope decreases with increasing θ and almost saturates at $\theta > 100°$, a slight enhancement of proton yields at the most backward angles is also reproduced.

The problem of describing pre-equilibrium emission is that pre-equilibrium particles have no definite source. The analysis of emission time distributions shows that they are

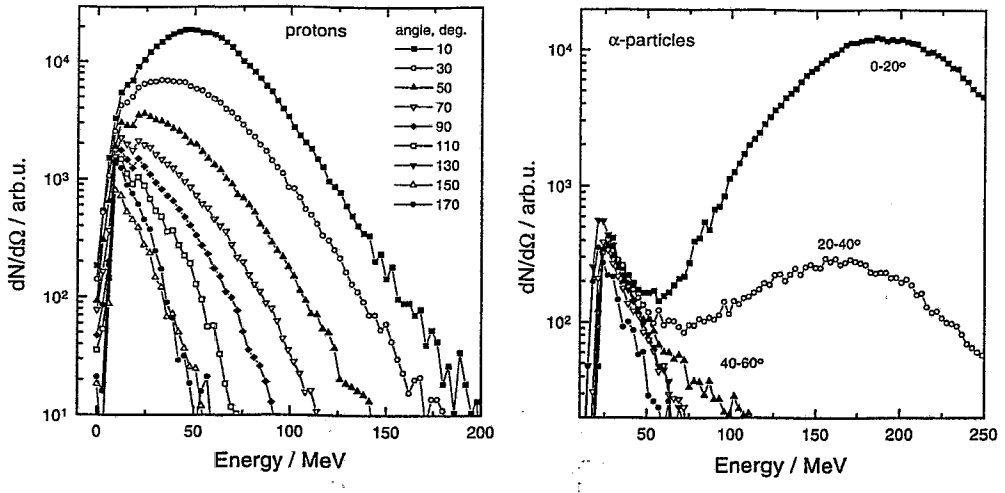

Figure D.3: *Inclusive spectra of protons (left panel) and α-particles (right panel) calculated with the Dubna Cascade Model. Spectra are accumulated within 20°-bins.*

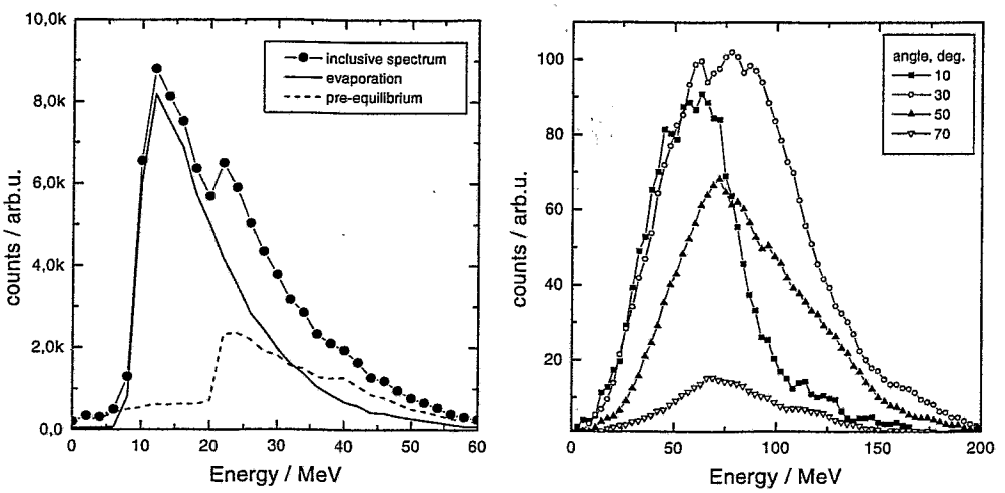

Figure D.4: *Left panel: The contribution of pre-equilibrium emitted protons is compared with the evaporation from the target-like fragment. Right panel: Spectra of pre-equilibrium emitted α-particles are accumulated within 20°-bins.*

most probably emitted within 60 fm/c after the beginning of the interaction. The rough estimation of the contact time using interaction radii from the systematics from ref. [140] delivers 70 fm/c. Therefore pre-equilibrium particles seem to come from the contact zone between colliding nuclei.

Proton spectra accumulated into the backward hemisphere are shown in fig. D.4, left panel. The pre-equilibrium component appeared to be comparable with the evaporative one. The simulated yield of pre-equilibrium α-particles into the backward hemisphere turned out to be low, their spectra for some forward angles are shown on the right panel. The maxima of these spectra lie at 50–80 MeV and, therefore, reminding the probable underprediction of the yields of complex particles, one should be careful also in interpreting α-particle spectra.

Acknowledgments

The author cordially thanks the FOBOS collaboration for providing the conditions to perform this work both in the FLNR JINR/Dubna and in the FZ-Rossendorf/Dresden.

Especially, I want to thank Prof. H.Freiesleben for having accepted the author as a fellow, for his tolerance during the long time the production of the results presented took, and for the constructive criticism during the preparation of the manuscript.

This work would has been impossible without help of a number of people who either worked together with me or just gave me some hints in "corridor-discussions". Therefore, I would implicitly thank all the people not namely listed here, who supported me in any way, for the close collaboration aimed at preparing the experiments, processing the data and interpretation of results. Among these, I am personally grateful to

- Dr.W.Wagner for his daily care about the current state of the work and, especially, for his friendly help in setting up of the scintillator shell and in describing experimental data. Numerous coffee-breaks dedicated to discussions are very appreciated;
- Dr. H.-G.Ortlepp for his large contribution in preforming experiments, for useful suggestions and for his critical estimate of the author;
- Prof. M.G.Itkis, Dr. H.Prade and Dr. A.Matthies for their kind support and for their permanent interest in the progress of this work and its results;
- Prof. W. von Oertzen, Dr. H.Fuchs and Dr. J.Krueger for the helpful introduction into the HI-data analysis preceding this work and for their interest to its development;
- Dr. K.-D.Schilling for his regular assistance in organization and for discussions during the entire work;
- V.S.Salamatin for his useful ideas concerning the mass asymmetry analysis and for the critical but fruitful discussions;
- Dr. C.-M.Herbach and V.G.Tishenko for their contribution to the data processing and for their sceptical comments;
- Dr. Yu.V.Pyatkov for his regular remarks concerning current results;
- the U400M-accelerator team under supervision of Dr. G.G.Gulbekian for working together during long and complicated experimental shifts;
- my family, namely to my father, Dr. V.V.Kamanin, for stimulating discussions and to my wife, Dr. I.Z.Kamanina, for her great moral support.

Bibliography

[1] H. Delagrange et al., Z. Phys. A323 (1986) 437.

[2] D. Hilscher and H. Rossner, Ann. Phys. Fr. 17 (1992) 471.
Issue HMI-92-P2 Hil-1, Berlin, Germany, 1992.

[3] V.E. Viola,Jr. et al., Physical Review C26 (1982) 178.

[4] D. Guerreau, Int. School on Nucl. Phys. "Nuclear Matter and Heavy Ion Collisions", Les Houches, France, 1989, Report GANIL P 89-07, Caen, France, 1989.

[5] R. Yanez, Report FZR-192, Rossendorf, Germany, 1997.

[6] W. Wagner et al., Nuclear Instruments and Methods A403 (1998) 65.

[7] H.-G. Ortlepp et al., Nuclear Physics A642 (1998) 407.

[8] D. Durand, Nuclear Physics A541 (1992) 266.

[9] V. Zagrebaev and Y. Penionzhkevich, Prog. Part. Nucl. Phys., Vol. 35 (1995) 575.

[10] A.Ya.Rusanov, M.G. Itkis and V.N. Okolovich, Physics of Atomic Nuclei Vol. 60 no.5 (1997) 773.

[11] M.G. Itkis and A.Ya.Rusanov, Fiz. Elem. Chast. At. Yad. Vol. 29 no.2 (1998) 389. (in Russian)

[12] V.E. Viola et al., Physical Review C31 (1985) 1550.

[13] A. Gavron et al., Physical Review C35 (1987) 579.

[14] J.O. Newton et al., Nuclear Physics A483 (1988) 126.

[15] D.J. Hinde et al., Physical Review C45 (1992) 1229.

[16] J.P. Lestone et al., Nuclear Physics A559 (1993) 277.

[17] I. Diôszegi et al., Physical Review C46 (1992) 627.

[18] P. Paul, M. Thoennessen, Ann. Rev. Nucl. Part. Sci. 44 (1994) 65.

[19] U. Brosa, S. Grossmann and A. Müller, Physics reports. 1971990167

[20] J.P. Lestone, Physical Review Letters 70 (1993) 2245.

[21] H. Ikezoe et al., Physical Review C42 (1990) 342.
H. Ikezoe et al., Physical Review C42 (1990) R1187.

[22] H. Ikezoe et al., Nuclear Physics A538 (1992) 299.

[23] A. Gavron, Physical Review C21 (1980) 230.

[24] D.J. Hofman et al., Physical Review C51 (1995) 2597.

[25] M. Gui et al., Physical Review C48 (1993) 1791.

[26] K. Siwek-Wilczynska et al., Physical Review C48 (1993) 228.

[27] R.J. Charity, Physical Review C51 (1995) 217.

[28] V.A. Rubchenya et al., Physical Review C58 (1998) 1587.

[29] G. van't Hof et al., Physical Review C54 (1996) R1515.

[30] V.V. Kamanin et al., Fiz. El. Chast. At. Yad. Vol. 20, no. 4 (1989) 741. (in Russian)

[31] K. Siwek-Wilczynska et al., Physical Review C51 (1995) 2054.

[32] H. Fuchs and K. Möhring, Rep. Prog. Phys. 57 (1994) 231

[33] D.R. Bowman et al., Physical Review C46 (1992) 1834.

[34] S.L. Chen et al., Physical Review C54 (1996) R2114.

[35] C.-M. Herbach, H.-G. Ortlepp and W. Wagner, Report FZR-198, Rossendorf, Germany, 1997.
C.-M. Herbach, H.-G. Ortlepp and W. Wagner, Proc. VI International School-Seminar on Heavy Ion Physics. Dubna, Russia, September 22-27, 1997.

[36] G.D. Adeev, et al., Fiz. Elem. Chast. At. Yad. Vol.19 (1988) 1229.

[37] H.-G. Ortlepp et al., in: "Heavy Ion Physics", Scientific Report 1995/96 (Ed. B.I. Pustylnik) JINR E7-97-206, Dubna, Russia, 1997, p.238

[38] E.C. Pollacco et al., Physical Letters B146 (1984) 29.

[39] W. Wagner and H.-G. Ortlepp, in: "Heavy Ion Physics", Scientific Report 1995/96 (Ed. B.I. Pustylnik) JINR E7-97-206, Dubna, Russia, 1997, p.243

[40] G.N. Flerov et al., Report JINR 9-84-55, Dubna, Russia, 1984.

[41] V.V. Bekhterev et al., in: "Heavy Ion Physics", Scientific Report 1995/96 (Ed. B.I. Pustylnik) JINR E7-97-206, Dubna, Russia, 1997, p.277

[42] M.M. Fowler et al., Nuclear Instruments and Methods A281 (1989) 517.

[43] J. Pouthas et al., Nuclear Instruments and Methods A357 (1995) 418.

[44] A. Gobbi et al., Nuclear Instruments and Methods A324 (1993) 156.

[45] S.V. Radnev et al., Contr. at the Internat. Conf. on Set-up FOBOS, Sofia, Bulgaria, 1990, JINR D7-90-539, Dubna, Russia, 1990, p.17.

[46] A.A. Alexandrov et al., Instruments and Experimental Techniques Vol.40, No.2 (1997) 170.

[47] G.D. Westfall et al., Nuclear Instruments and Methods A238 (1985) 347.

[48] W. Seidel et al., Nuclear Instruments and Methods A273 (1988) 536.

[49] C.R. Grun et al., Nuclear Instruments and Methods 196 (1982) 33.

[50] H.-G. Ortlepp and A. Romaquera, Nuclear Instruments and Methods A267 (1989) 500.

[51] A.Matthies et al., Contr. at the Symp. on Correlation Experiments on Heavy Ion Beams, Dresden 1988, JINR D7-88-299, Dubna, 1988, p.11.

[52] M. Gebhardt, Diploma Thesis, Johann Wolfgang Goethe - Universität, Frankfurt am Main, Germany, 1995;
M. Gebhardt et al., Report FZR-78, Rossendorf, Germany, 1995, p.81.

[53] G. Renz et al., Proc. of the FOBOS workshop'94, Cracow, Poland, 1994 (Ed. W. Wagner) FZR-65, Rossendorf, Germany, 1995, p.46;
G. Renz et al., Report FZR-78, Rossendorf, Germany, 1995, p.115.;
G. Renz et al., in: "Heavy Ion Physics", Scientific Report 1993/94 (Ed. B.I. Pustylnik) JINR E7-95-227, Dubna, Russia, 1995, p.222

[54] W.Terlau, PhD Thesis, Freie Universitaet Berlin, Germany, 1988.

[55] J. Tõke et al., UR-NSRL-394, University of Rochester, USA, 1993.

[56] O. Strekalovskii et al., Instruments and Experimental Techniques Vol.41, No.1 (1998) 41.
O. Strekalovskii et al., Pribory i Technika Eksperimenta, Vol. 1 (1998) 49(in Russian).

[57] O.V.Strekalovski, PhD Thesis, Joint Institut for Nuclear Research, Dubna, 1985.

[58] O.V. Strekalovsky et al., Proc. of the XVI Internat. Symp. on Nuclear Electronics and VI Internat. School on Automation and Computing in Nuclear Physics and Astrophysics, Varna, Bulgaria, 1994 (Ed. I.N. Churin) JINR D13-94-491, Dubna, Russia, 1995, p. 31
O.V. Strekalovsky et al., Proc. of the FOBOS Workshop'94, Cracow, Poland, 1994 (Ed. W. Wagner) FZR-65, Rossendorf, Germany, 1995, p.49.

[59] STRUCK - Product Summary, Hamburg, Germany, 1990.

[60] C.A.E.N. - General Catalogue, Viareggio, Italy, 1993.

[61] LeCroy - Research Instrumentation Catalog, Chestnut Ridge NY, USA, 1992.

[62] P. Ziem et al., Report FZR-92-11, Rossendorf, Germany, 1992, p. 19.

[63] M. Wilpert, privat communication, HMI/Berlin, 1995.

[64] C.-M. Herbach and C. Umlauf, in: "Heavy Ion Physics", Scientific Report 1991/92 (Ed. B.I. Pustylnik) JINR E7-93-57, Dubna, Russia, 1993, p.250

[65] C.-M. Herbach and D.V. Vakatov, Proc. of the FOBOS workshop'94, Cracow, Poland, 1994 (Ed. W. Wagner) FZR-65, Rossendorf, Germany, 1995, p. 56.

[66] G. Röschert, HMI-B436, Berlin, Germany, 1986;
G. Röschert, "HOOPSY under VMS - A Program System for Multi-Parameter-Experiments", Version 12, Hahn-Meitner-Institut, Berlin, Germany, 1992.

[67] K.-P. Eckert, S. Gipp, and S. Wasserroth, HMI-D/M 154, Berlin, Germany, 1984;
"OLYMP – A System for the Evaluation of multi- dimensional experimental Data and Spectra", Version 5.4, Hahn-Meitner-Institut, Berlin, Germany, 1992.

[68] H. Stelzer, "CAMDA – a CAMAC-PC Data Aquisition System", Messel, Germany, 1989.

[69] J.B. Birks, "The Theory and Practice of Scintillation Counting", Pergamon Press, Oxford, 1964.

[70] V.V. Avdeichikov et al., Nuclear Instruments and Methods A349 (1994) 216.

[71] S. Usuda, A. Mihara and H. Abe, Nuclear Instruments and Methods A321 (1992) 247.

[72] V.V.Avdeichikov, private communication, JINR, Dubna, 1998. (submitted to Nucl. Instr. and Meth. A)

[73] W. Wagner et al., Scientific Report 1991/92 "Heavy Ion Physics" (ed. B.I. Pustylnik) JINR E7-93-57, Dubna, Russia, 1993, p. 244.

[74] J. Alarja et al., Nuclear Instruments and Methods A242 (1986) 352.

[75] F. Benrachi et al., Nuclear Instruments and Methods A281 (1989) 137.

[76] W. Wagner et al., Report FZR-78, Rossendorf, Germany, 1995, p. 117.

[77] W. Wagner et al., JINR Rapid Comm. 4(61)-93, Dubna, Russia, 1993.

[78] A.S. Fomichev et al., Nuclear Instruments and Methods A344 (1994) 378.

[79] Mod. F683 C (CIAFB) 96 Channel charge integrating ADC, Technical information Manual, Viareggio, Italy, 1991.

[80] A.Beer, G. Critin, G. Schuler, Nuclear Instruments and Methods A234 (1985) 294.

[81] F. Bourgeois et al., High-density CAMAC and FASTBUS charge integrating ADC for use at the LEP OPAL. IEEE NS34 No.1, 1987.

[82] REDUV Manual, Institut de Physique Nucléaire, Orsay, France.

[83] CF8101 Octal fraction discriminator, User's Manual, GSI, Germani, 1990.

[84] Mod. 4418/T CAMAC 8-input ADC, User's Manual, Via Firenze, Italy, 1991.

[85] C.A.E.N. SY403 High Voltage System User's Manual, Viareggio, Italy, 1992.

[86] Mod. C117B H.S. CAENET CAMAC Controller. Technical information Manual, Viareggio, Italy, 1992.

[87] Proc. of the FOBOS workshop '94, Cracow, Poland, 1994 (ed. W. Wagner) Report FZR-65, Rossendorf, Germany, 1995; p. 40

[88] Bronstein, Semendjajew, Taschenbuch der Mathematik.

[89] Yu.A. Baurov et al., in: "Heavy Ion Physics", Scientific Report 1995/96 (Ed. B.I. Pustylnik) JINR E7-97-206, Dubna, Russia, 1997, p.354

[90] D. Guinet et al., Nuclear Instruments and Methods A278 (1989) 614.

[91] D.V. Kamanin et al., Nuclear Instruments and Methods A413 (1998) 127.// Report FZR-197, Rossendorf, Germany, 1997.

[92] A.S. Fomichev et al., Nuclear Instruments and Methods A350 (1994) 605.

[93] D. Horn et al., Nuclear Instruments and Methods A320 (1992) 273.

[94] N. Colonna et al., Nuclear Instruments and Methods A321 (1992) 529.

[95] Y. Larochelle et al., Nuclear Instruments and Methods A348 (1994) 167.

[96] K. Michaelian, A. Menchaca-Rocha, and E. Belmont-Moreno, Nuclear Instruments and Methods A356 (1995) 297.

[97] E. Costa, E. Massaro and L. Piro, Nuclear Instruments and Methods A243 (1986) 572.

[98] D.W. Stracener et al., Nuclear Instruments and Methods A294 (1990) 485.

[99] K. Michaelian, A. Menchaca-Rocha, and E. Belmont-Moreno, Nuclear Instruments and Methods A334 (1993) 457.

[100] H. Fuchs, D. Kamanin, and J. Krüger, Ann. Rep. 1994, HMI-B 526, Hahn-Meitner-Institut, Berlin, 1995, p. 137.

[101] A.J. Bird et al., Nuclear Instruments and Methods A353 (1994) 46.

[102] M. Moszynski et al., Nuclear Instruments and Methods A336 (1993) 587.

[103] W. Wagner and D.V. Kamanin, Report FZR-130, Rossendorf, Germany, 1996, p. 150.

[104] J. Henniger and B. Horlbeck, JINR E6-84-366, Dubna, Russia, 1984.

[105] T. Masuda et al., Nuclear Instruments and Methods A332 (1992) 135.

[106] W. Wagner and H.-G. Ortlepp, Report FZR-35, Rossendorf, Germany, p. 93.

[107] H.-G. Ortlepp et al. and FOBOS Collaboration, Scientific Report 1995/96 "Heavy Ion Physics", (ed. B.I. Pustylnik) JINR E7-97-206 JINR Dubna, Russia, p. 236.

[108] D.V. Kamanin et al., Proc. Third Int. Conf. on Dynamical Aspects of Nuclear Fission, Casta-Papiernicka, Slovak Rep., 1996. Ed. by. J.Kliman and B.I.Pustylnik, JINR Dubna, 1997. p.183.

[109] K.R. Schubert, Technische Universität Dresden, Germany, 1996 (private communication).

[110] J. Krüger, PhD Thesis, Technischen Universität Dresden, Germany, 1996.

[111] G. Klotz-Engmann et al., Nuclear Physics A499 (1989) 392.

[112] C.-M. Herbach et al., Report FZR-159, Rossendorf, Germany, 1996.

[113] C.-M. Herbach and H.-G.Ortlepp, Annual Report 1997, Institute of Nuclear and Hadronic Physics, FZR-215, Rossendorf, Germany, 1998, p.56.

[114] W. Bauer, Physical Review C40 (1989) 715.

[115] H.-G. Ortlepp et al., Proc. of the FOBOS workshop'94, Cracow, Poland, 1994 (Ed. W. Wagner) FZR-65, Rossendorf, Germany, 1995, p.29

[116] H.-G. Ortlepp et al., Annual Report 1995, Institute of Nuclear and Hadronic Physics, FZR-130, Rossendorf, Germany, 1996, p.93.

[117] Y. Lou et al., Nuclear Instruments and Methods A581 (1995) 373.

[118] P. Fröbrich, I.I. Gontchar and N.D. Mavlitov, Nuclear Physics A556 (1993) 281.

[119] I.I. Gontchar, Fiz. El. Chas. At. Yad. 26 (1995) 932.

[120] R.S. Kurmanov et al., Annual Report 1995, Institute of Nuclear and Hadronic Physics, FZR-130, Rossendorf, Germany, 1996, p.97.

[121] J. Lukasik et al., Physical Review C55 (1997) 1906.

[122] Y. Larochelle et al., Physical Review C55 (1997) 1869.

[123] A.Siwek et al., Preprint LPCC 97-16, Caen, France, 1997. (submitted to Physical Review C)

[124] R. Wada et al., Physical Review C55 (1997) 227.

[125] J. Pochodzalla et al., Physical Review Letters 75 (1995) 1040.

[126] Yu.P. Gangrsky, B. Dalhcuren and B.N. Markov, Nuclear fission recoils. ENERGOATOMIZDAT, Moscow, 1986. (in Russian)

[127] R. Wada et al., Physical Review C39 (1989) 497.

[128] G.G. Adamian et al., Physical Review C53 (1996) 871.

[129] G.G. Adamian et al., Zeitschrift für Physik A347 (1994) 203.

[130] A.A. Alexandrov et al., Annual Report 1997, Institute of Nuclear and Hadronic Physics, FZR-215, Rossendorf, Germany, 1998, p.57.

[131] P.Klein et al., Zeitschrift für Physik A357 (1997) 193.

[132] J. Peter et al., Nuclear Physics A593 (1995) 95.

[133] J.P. Lestone, Doctoral Thesis, Australian National University, 1990.

[134] R.S. Kurmanov, L.A. Litnevsky, Private communication, Omsk, Russia, 1995.

[135] G.I. Kosenko, D.V. Vanin, G.D. Adeev, Yadernaja Fizika, vol.61, n.3 (1998) p.416 (in Russian).

[136] A.S. Iljinov et al., Nuclear Physics A543 (1992) 517.

[137] D.V.Kamanin and V.S.Salamatin, 1999. The paper is in progress.

[138] Y. Schutz et al., Report GANIL P 97-15, Caen, France, 1997.

[139] H.K. Leegte et al., Physical Review C46 (1992) 991.

[140] W.W. Wilcke et al., Atomic data and nuclear data tables 25 (1980) 389-619.

Index

almost binary events, 82, 84, 85

backward hemisphere, 65
BF
  abbr. binary fragmentation, 10, 84, 86
  distribution, 86
BIC
  abbr. Bragg Ionization Chamber, 13

CDSM
  abbr. Combined Dynamical Statistical Model, 67, 103
CIS
  abbr. CsI(Tl) scintillator, 13, 22, 39
  detector, 24
  energy resolution, 26
  event, 64
  lid, 26
  single file, 35
correlation coefficient, 32

DCM
  abbr. Dubna Cascade Model, 105

energy losses, 47, 99
excitation energy, 53
  sharing parameter, 75, 78

FF
  abbr. fission fragment, 3, 13
fission-like process, 84, 91, 93, 95

Galilean-invariant coordinates, 68

IMF
  abbr. intermediate mass fragment, 7, 13

LCP
  abbr. light charged particle, 3, 13, 39
  data consistency, 64, 69
  multiplicities, 67, 70
  spectra, 51, 67, 68, 71
    correction, 36
    simulation, 106
  total mass, 64
  total velocity, 64
Lestone-parametrization, 102
LMT
  abbr. linear momentum transfer, 9, 30

parameter
  R_χ, 80
  $\bar{\zeta}$, 75
  χ, 55
  χ_{prim}, 58
  χ_{sec}, 73
  ζ, 78
particle branch
  ascending, 23
  descending, 23
PIM
  abbr. particle identification matrix, 23, 41
  examples, 17, 18, 23, 31, 40
  ideal, 42, 45–47, 100
  sumed, 40, 42
pre-equilibrium emission, 64, 65, 71, 82, 105
PSA
  abbr. pulse-shape analysis, 22, 27, 39
PSAC
  abbr. position-sensitive avalanche counter, 13
PTP
  abbr. punch-through point, 36, 39
  definition, 35
  energy, 41
  simulated, 45, 50

quenching, 43, 45

reaction time, 84

scission angle, 82, 83, 85, 88
    distribution, 85, 89

ternary event, 11, 56, 84, 89, 95
TKE
    abbr. total kinetic energy, 5
    distribution, 59, 61
    formula, 60

Versicherung

Hiermit versichere ich, daß ich die vorliegende Arbeit ohne unzulässige Hilfe Dritter und ohne Benutzung anderer als der angegebenen Hilfsmittel angefertigt habe; die aus fremden Quellen direkt oder indirekt übernommenen Gedanken sind als solche kenntlich gemacht. Die Arbeit wurde bisher weder im Inland noch im Ausland in gleicher oder ähnlicher Form einer anderen Prüfungsbehörde vorgelegt.

Dmitri Kamanin